Laminated Holocene lacustrine sediment records of ENSO and PDO-scale climate variability from the Pacific Basin

by

Samuel Z. Mark

B.S Geology, Bates College, 2016

Submitted to the Graduate Faculty of the

Dietrich School of Arts and Sciences in partial fulfillment

of the requirements for the degree of

Doctor of Philosophy

University of Pittsburgh

2023

UNIVERSITY OF PITTSBURGH

DIETRICH SCHOOL OF ARTS AND SCIENCES

This dissertation was presented

by

Samuel Z. Mark

It was defended on

June 1, 2023

and approved by

Josef Werne, Professor and Chair, Department of Geology & Environmental Science, University of Pittsburgh

Eitan Shelef, Professor, Professor, Geology & Environmental Science, University of Pittsburgh

Daniel Bain, Professor, Geology & Environmental Science, University of Pittsburgh

Byron Steinman, Professor, Earth & Environmental Science, University of Minnesota-Duluth

Dissertation Director: Mark Abbott, Professor, University of Pittsburgh

Laminated Holocene lacustrine sediment records of ENSO and PDO-scale climate variability from the Pacific Basin

Samuel Z. Mark, PhD

University of Pittsburgh, 2023

The Pacific Ocean is a dominant driver of global climate variability on interannual to multidecadal timescales. The El Niño Southern Oscillation (ENSO) and the Pacific Decadal Oscillation (PDO) are large-scale ocean-atmospheric patterns which influence hydroclimate anomalies and correspondingly influence the structure and condition of terrestrial ecosystems. Here, laminated lacustrine sediments from the Ecuadorian Andes and Pacific Northwest of North America are used to reconstruct the long-term variability of these relatively high-frequency (interannual-decadal) climatic phenomena.

Flood deposits from Laguna Pallcacocha, Cajas Parque Nacional, Ecuador, have previously been used to quantify the frequency of El Niño events over the Holocene (11,700 BP-present). Here, I employ sedimentary sequences from three lakes, each of which displays different sensitivities to El Niño-driven flood events in an effort to reconstruct changes in both the frequency and amplitude of ENSO. An XRF-based flood reconstruction from the well-studied Laguna Pallcacocha sedimentary record supports an emerging consensus among proxies indicating 10-20 year flood return intervals during the early Holocene (11,700-7,500 BP), >20 year El Niño return intervals during the middle Holocene (7,500-4,000 BP) and 2-10 year El Niño frequency from 4,000 to present. The Little Ice Age (LIA: 1450-1850 CE) experienced infrequent, high-intensity El Niño's compared to the preceding Medieval Climate Anomaly (MCA: 950-1250 CE) which experienced the opposite pattern.

Oxygen isotope reconstructions of precipitation-evaporation balance from Castor and Round Lake, Washington help reveal long-term links between the tropics and northern hemisphere mid-latitudes. At both sites, the MCA was marked by relatively stable and moist conditions, while the LIA was marked by intense oscillations between drought and pluvial cycles, leading to enhanced fire activity. Over the course of the Holocene, long-term changes in orbital configuration, interannual to multidecadal forcing associated with ENSO and PDO, and abrupt landscape disturbances such as volcanic tephra deposits have left profound impacts on terrestrial ecosystems. These findings demonstrate that climate phenomena which operate on timescales relevant to human society have exhibited wide ranges of variability over the Holocene.

Table of Contents

List of Tables

List of Figures

Preface

I owe too many thanks to too many people to do a thorough job of it here, but will try regardless. First to my advisor Mark Abbott for his guidance, support, and willingness to let me pursue different ideas. Choosing a lab and a graduate program is in some ways a crapshoot and I really lucked out. I look forward to continuing to bounce ideas back and forth in the future. My committee, consisting of Profs. Eitan Shelef, Josef Werne, Dan Bain, Don Rodbell and Byron Steinman, have provided mentorship, field assistance, inspiration, lab access, editing, support, and a litany of other necessities which have made the past six years valuable (and hopefully not just to me). Cathy Whitlock and her laboratory at Montana State University taught me not just the specifics of paleoecological methods and data processing but vastly expanded my appreciation of what kind of questions can be asked of lake sediments. To members of the Abbott Lab and other collaborators who both predate and postdate me –Arielle Woods, Sophie Lehmann, MG Bustamante, Nick Wondoloski, Tyler Rohan, Everett Lasher, Jamie Vornlocher, Hailey Sinon, Shannon Christensen, Michelle Kim, Melissa Griffore, Alejandro Fernandez – I hope I can provide even a fraction of what you have. I spent the height of the pandemic locked up with four people and two dogs who became lifelong friends and sources laughter and inspiration —Hillary, Mason, Allie and Mike, along with Griff and Rooster. Thank you Luke and Laura for incorrectly assuming I'm clever enough to participate in back and forths with you. Thank you Margaret for helping me think more differently than I have before. Finally, I owe the largest ongoing debt of gratitude to my parents Beth and David and brother Ben. I'm sure you'll each have different and valid criticisms of my casting it as a "debt" so I'll settle for expressing gratitude.

1.0 Introduction: The role of the Pacific in global climate: significance and questions

The El Niño Southern Oscillation (ENSO) and the Pacific Decadal Oscillation (PDO) are coupled ocean-atmospheric phenomena which influence weather and climate patterns worldwide (McPhaden et al 2020). ENSO, defined by sea-surface temperature and atmospheric pressure anomalies in the tropical Pacific Ocean, is defined by 2-8 year periods (Trenberth 1997), while the PDO operates over multi-decadal (15-60 year) timescales and is defined by sea surface temperature anomalies in the northern mid-latitudes (Newman et al. 2016). Both systems have been shown to exert pronounced influence on drought (Kumar et al. 1999, McCabe et al. 2004), wildfire activity (Fasullo et al. 2018, Heyerdahl et al. 2008), and agricultural systems (Antilla-Hughes et al. 2021, Schillerberg et al. 2020). Despite the significance of these climate modes to modern human society, a comprehensive understanding of their past variability and their response to external climate forcing mechanisms remains rudimentary. Temporally continuous paleoclimate reconstructions can help resolve these uncertainties; however, well-preserved archives of interannual- to decadal-scale climate phenomena spanning long timescales are relatively rare. Questions such as: does ENSO strengthen or weaken in a warmer world? Will changes in global temperature be buffered or exacerbated by changes in ENSO and the PDO? Do the wavelength and amplitude of these systems shift substantially under different background climate states? remain unanswered.

To this end, I present high-resolution lacustrine records of climate variability from three lakes in the Ecuadorian Andes and two lakes in eastern Washington state. Scanning x-ray fluorescence (XRF) is used to reveal flood deposits related to intense El Niño-driven rainstorms in the Ecuadorian Andes, allowing us to reconstruct changes in the frequency and intensity of these

events over the past 11,000 years. In northwestern North America, a region which generally experiences drier conditions during El Niño and PDO warm phase (PDO+) events, oxygen isotopes from authigenic calcium carbonate are used to reconstruct precipitation-evaporation balance. Charcoal and pollen accumulation records from the same sedimentary sequences are used to evaluate the influence of high-resolution climate phenomena on terrestrial ecology. A shared feature of these reconstructions (apart from their sensitivity to Pacific climate forcing) is interannual-decadal sampling resolution throughout the entirety of each sedimentary sequence. This approach is powerful in that it not only allows for the reconstruction of long-term changes in climate patterns (driven by millennial-scale changes in orbital configurations, for example) but also shifts in sub-centennial phenomena which have profound impacts on human civilization.

1.1 ENSO and Pacific Multidecadal Variability

The El Niño Southern Oscillation is the most significant source of interannual climate variability worldwide (Lu et al. 2018). The term derives from linking periodic oceanic warming in the eastern equatorial Pacific (colloquially known as "El Niño", or the Christ-child, to Peruvian fisherman because these anomalies typically peak near Christmas, Trenberth 1997) to tropical atmospheric pressure and rainfall anomalies, termed the Southern Oscillation (Walker 1924). Bjerknes (1969) was the first to connect the oceanic and atmospheric components of the system, though the term "El Niño Southern Oscillation" was not in use until later (Rasmusson and Carpenter 1983). During ordinary (neutral) ENSO conditions, easterly equatorial winds draw surface waters from coastal South America towards Indonesia, creating upwelling of cold, deep water and shoaling of the thermocline in the eastern equatorial Pacific (Bjerknes 1969). Warm

waters in the Indo-Pacific region generate convective rainstorms and low atmospheric pressures, creating persistently moist conditions. After this convection and rainout occurs, the resultant airmass then flows back down the pressure gradient from west to east, where it subsides over coastal equatorial South America, creating high pressure systems and dry climates, thus forming a semi-closed loop known as the Walker Circulation (Bjerknes 1969).

El Niño events constitute a weakening or reversal of these prevailing conditions. While the precise mechanisms which initiate an El Niño remain contested (Anderson et al. 2013), and while no two El Niño events are identical (Ashok et al. 2007), their occurrence generally follows a recognizable pattern. During a canonical El Niño event (during which warming is centered in the eastern, rather than central tropical Pacific, Ren and Jin 2013), a weakening of Pacific Walker Circulation, caused by slackening of equatorial easterly winds occurs. Next, the surface of the eastern tropical Pacific warms, and the thermocline deepens. This causes anomalous convection and rainfall in coastal equatorial South America (see chapters 2 and 3) and atypical subsidence and drought in the Indo-Pacific warm pool (Goddard and Gershunov 2020). The impact of this subsidence extends far beyond the tropical Pacific, where Walker Circulation takes place; Indian monsoon failures (Kumar et al. 2006), malaria outbreaks in Africa (Mabaso et al. 2007) and South America (Mantilla et al. 2009), and even incidents of civil conflict (Hsiang et al. 2011) have all been associated with the occurrence of El Niño events.

An additional consequence of El Niño events is the presence of lower frequency modes of climate variability in the subtropical Pacific (Newman et al. 2016). Mantua et al. (1997) found a multidecadal quasi-oscillatory phenomena in the northern mid-latitudes of the Pacific which had a pronounced impact on salmon productivity. Termed the Pacific Decadal Oscillation (PDO), this pattern bears a strong spatial resemblance to that of ENSO, with PDO-positive phases marked by

warmer surface waters in the eastern tropical Pacific and along the western coast of North America. This configuration of temperature anomalies also strengthens the persistent Aleutian Low pressure system and deflects mid-latitude storm tracks to the south, making conditions over northwestern North America generally more arid (McAfee and Wise 2016, see chapters 4 and 5). Correspondingly, these phenomena have profound impacts ecosystem productivity (Berkelhammer 2017). The role that the PDO plays in driving fire activity (Hessl et al. 2004, Heyerdahl et al. 2008) in northwestern North America has been a topic of increasing interest (Halofsky et al. 2020) as fuel moisture, ignition opportunities, and spread are all influenced by PDO-driven climate dynamics.

The PDO is generally explained as a function of both tropical and extra-tropical forcing mechanisms. A commonly applied model represents the PDO as an integrator of ENSO-driven temperature anomalies (Liu and Alexander 2007). These short-lived pulses of warming, it is suggested, are "smoothed" by thermal inertia which creates multidecadal-scale variability rather than simply reflecting the 2-8 year timescales commonly associated with ENSO (Newman et al. 2016). However, recent work has called into question whether multidecadal climate phenomena such as the PDO represent true oscillatory phenomena intrinsic to the climate system (Mann et al. 2020) or whether they are in fact transitory artifacts which have, over the past several centuries, been driven by the combined impact of quasi-periodic volcanic aerosol spikes and anthropogenic emissions (Mann et al. 2021). Clearly, well-dated high-resolution paleoclimate reconstructions sensitive to these phenomena are necessary to better understand the behavior of ENSO and the PDO under different background climate states, and to better understand how they interact with one another.

1.2 Insight from high-resolution paleoclimate records from the Pacific

While evidence of ENSO-scale climate variability extends back at least as far as the Cretaceous (Davies et al. 2012), ENSO variability over even the recent past (~1200 years) remains largely unresolved (Emile-Geay 2013, Henke et al. 2017). Because of the large spatial scale of the phenomena, the geologically brief wavelength at which ENSO events evolve and decay, and the diversity between different individual events, paleoclimate proxies which faithfully capture ENSO and individual ENSO events are extraordinarily rare and valuable. Those which have been particularly useful over the Holocene include fossil corals, which detect ENSO-driven sea surface temperature and salinity changes in the carbonate chemistry of their skeletons (Cole et al. 1993, Cobb et al. 2003, Cobb et al. 2013, Dee et al. 2020); tree-rings, whose width changes according to temperature and precipitation patterns influenced by ENSO via remote atmospheric teleconnections (D'Arrigo et al. 2005, Li et al. 2011, Fowler et al. 2012); marine foraminifera, which are sensitive to shifts in thermocline depth temperature (Koutavas and Joanides 2012, Rustic et al. 2015); and lake sediments, which can offer long, continuous reconstructions and are sensitive to a multitude of environmental variables but generally lack interannual sampling resolutions (Rodbell et al. 1999, Moy et al. 2002, Thompson et al. 2017).

Though each of these proxy types is sensitive to different aspects of the climate system and contains its own strengths and weaknesses, Holocene-scale ENSO reconstructions tend to indicate a severe reduction in ENSO frequency, amplitude, or both during the middle Holocene (Emile-Geay et al. 2016, Du et al. 2021, Grothe et al. 2020). While pattern is at least partially due to changes in Earth's orbital configuration (Carre et al. 2021), others have noted that variability arising from internal dynamics is a substantial control on centennial-scale variability seen in many

ENSO records (Cobb et al. 2013). Additional continuous, high-resolution, well-dated records are necessary to better understand how and why ENSO has developed over the Holocene.

The paleoclimate literature concerning the Pacific Decadal Oscillation is much less robust (Stone and Fritz 2006). A similar array of geological materials can be used to reconstruct PDO and PDO-scale phenomena. Some tree-ring (D'Arrigo et al. 2001, MacDonald and Case 2005), coral (Gedalof et al. 2002), and lake sediment (Kirby et al. 2010, Nelson et al. 2011) records have been developed, but there remains a paucity of continuous proxy reconstructions of decadal-multidecadal scale climate phenomena in regions affected by the PDO. Existing research suggests there were predominantly muted/PDO-negative conditions between 8.2-4.2 kyr BP, roughly coincident with the proposed minimum in ENSO variability (Barron and Anderson 2011). After 4.2 kyr BP, an increase in the number of El Niño events (Du et al. 2021, Rodbell et al. 1999, Conroy et al. 2008) may have generated more PDO-positive conditions in northwestern North America via atmospheric teleconnections. However, a lack of high-resolution continuous archives of decadal hydroclimate has thus far hindered our understanding of whether these shifts were related to insolation-scale mean-state changes (i.e changing background conditions) or were related to quasi-oscillatory phenomena like the PDO.

The PDO has previously been shown to influence regional-scale ecosystem composition and productivity (Berkelhammer 2017). Its most societally relevant ecosystem impact, however, may be its role in driving fire activity in semi-arid western North America (Hessl et al. 2004, Schoennagel et al. 2005). Prolonged wet periods can facilitate the growth of fine fuels on the landscape, as well as suppress fire activity, which subsequently desiccate and burn during arid conditions associated with the opposite PDO phase (Cooper et al. 2021). Additionally, persistent atmospheric anomalies associated with the PDO can facilitate or depress the ignition and spread

of fire (Kitzberger et al. 2007, Trouet et al. 2006). Our limited understanding of pre-instrumental PDO variability thus hampers our understanding of past controls on fire regimes. This, in turn, hinders future projections of fire in a changing climate. Multi-proxy sediment records sensitive to fire, hydroclimate, and terrestrial ecosystem composition are thus necessary to better understand the complex, nonstationary relationships between fire and climate.

1.3 Outline of dissertation

In the ensuing dissertation, I intend to improve our understanding of how and why ENSO and the PDO have evolved over the Holocene, and how these changes have driven fire dynamics in semi-arid northwestern North America. Chapter 2 focuses on a flood history reconstruction from sediments in Laguna Pallcacocha, Ecuador. This sedimentary sequence has been widely studied in the past, as it is likely the only published work which provides a continuous record of individual El Niño events spanning the entire Holocene (Rodbell et al. 1999, Moy et al. 2002). Recent work, however, (Schneider et al. 2018) has called the original interpretation of this record into question. By adding additional chronological control points and evidence from surface sediments collected over the past 20 years, we affirm the sensitivity of this widely cited record to El Niño-driven flooding. By incorporating XRF data where previous studies used sediment color, we find a greater number of El Niño events in the early Holocene (11,700-7,500 yr BP) than previously documented. The resulting Holocene-scale flood chronology is consistent with a developing consensus of proxy records from around the Pacific, indicating decadal-scale El Niño frequency during the early Holocene, rare, multi-decadal El Niño events during the middle Holocene (7,500-4,000 BP) and sub-decadal El Niño return intervals during the late Holocene

(4,000-present). This pattern aligns with proposed orbital forcing controls on ENSO dynamics, but changes in orbital configuration alone cannot explain centennial-scale variability in the flood history. Thus, dynamics internal to the ENSO system or other mechanisms, such as teleconnections to other basins, must be invoked.

Chapter 3 incorporates sedimentary records from two lakes within 5 km of Laguna Pallcacocha, each of which contains a different chronology of flooding events. The differences in stratigraphy are attributed to the unique geomorphic setting of each watershed. Differences in basic topographic parameters and landcover make a flood deposit in each sedimentary sequence a valid proxy for a hydrological maxima exceeding a different, watershed-specific, threshold. Laguna Pallcacocha records flooding events with relatively short return intervals, making its sediments valuable for reconstructing El Niño frequency. Nearby Lagunas Martin and Fondococha, conversely, are sensitive only to more extreme events, making them records of El Niño intensity. By grouping ENSO proxies from different archival types according to a frequency/intensity framework, lingering discrepancies can be largely resolved (Henke et al. 2017). Coral (Cobb et al. 2013) and foraminiferal (Rustic et al. 2015) reconstructions, which relate to the amplitude of the ENSO signal, more closely resemble the sedimentary records from Lagunas Martin and Fondococha. Conversely, ENSO frequency reconstructions from tree-rings and annually laminated lake sediments more closely resemble the sedimentary record from Laguna Pallcacocha. The Medieval Climate Anomaly (MCA, 950-1250 CE) was marked by relatively high-frequency, low-intensity El Niño events while the subsequent Little Ice Age (LIA, 1450-1850 CE) was marked by the opposite conditions. The middle Holocene, when most ENSO proxies suggest relatively infrequent El Niño's, experienced occasionally very powerful El Niño events.

Chapter 4 is focused on high-resolution records of precipitation-evaporation balance from oxygen isotopes and fire activity from charcoal accumulation records spanning the past 1300 years at Castor and Round Lakes, WA. Quantitative comparison of the Castor Lake oxygen isotope record over the period covered by instrumental data and tree-ring records shows that the isotopic mass-balance of lake water is largely driven by winter precipitation, consistent with proxy-system modelling results (Steinman et al. 2010). Additionally, detrending of lake sediment data produces higher correlation with nearby tree-ring chronologies (Dannenberg and Wise 2016), indicating low-frequency climate variability may be lost during the composition of tree-ring chronologies. Contrary to many fire history reconstructions in western North America, we find greater biomass burning occurred during the LIA than the MCA. Significant correlations exist between charcoal accumulation and the amplitude of multi-decadal hydroclimate variability. Previously hypothesized mechanisms which suggest that production and connectivity of fuels to wet PDO-negative (cool) phases which subsequently desiccate and burn during PDO-positive (warm) phases may thus have been important controls on fire during the last millennium. Additionally, the forced removal of Native inhabitants and imposition of Euro-American land use patterns during the mid-19th century drastically altered fire and fire-climate relationships.

Chapter 5 expands the Round Lake oxygen isotope dataset to cover the Holocene. Oxygen isotopes indicate a dry early Holocene, a moist middle Holocene, and a relatively moist and variable late Holocene, consistent with other oxygen isotope reconstructions. A persistently PDO-/La Niña like mean state in the tropical Pacific, consistent with previous work (Barron et al. 2010) may explain increased winter precipitation. Lake level indicators and pollen data, however, suggest drier conditions, driven by elevated summer insolation and a persistent subtropical Pacific blocking high pressure system (Bartlein et al. 1998). Multidecadal variability is consistent

between other sites with high-resolution oxygen isotope records, and indicate that the past 1000 years has experienced anomalously high amplitude swings in hydroclimate over multidecadal timescales. Correlations between arboreal pollen and oxygen isotopes are improved by incorporating 60-100 years of preceding oxygen isotope data, demonstrating the long-term sensitivity of terrestrial ecosystems to precipitation variability. Finally, chapter 6 summarizes the findings described above and outlines remaining areas of uncertainty and potential future work on these topics.

2.0 XRF Analysis of Laguna Pallcacocha Sediments Yields New Insights into Holocene El Niño Development

The laminated sedimentary sequence of Ecuador's Laguna Pallcacocha is one of the most widely cited proxy records of Holocene El Niño Southern Oscillation (ENSO) variability. Previous efforts to reconstruct flood-driven laminae from Laguna Pallcacocha relied solely on sediment color, a useful but non-specific metric of flood events. We improved the chronology with ^{210}Pb and additional ^{14}C dates over the past millennium, which allows for comparison of the sedimentary record with historically documented El Niño events. Additionally, we use elemental composition derived from X-ray Fluorescence (XRF) to reconstruct flood history at Pallcacocha. A principal component analysis (PCA) of the XRF dataset identifies minerogenic flood-driven clastic laminae. The first principal component (PC1) of the XRF data and red color intensity are positively correlated over the past 7.5 kyr, but the color record fails to capture high frequency variability that is preserved in the XRF dataset during the early Holocene (approximately 7.5-11 kyr BP). The new XRF dataset indicates moderate El Niño activity during the early Holocene, suppressed El Niño activity in the middle Holocene, and enhanced El Niño activity during the late Holocene. This pattern is relatively common among other ENSO records, and has been attributed to long-term changes in tropical insolation. Some intervals-most notably between 3-2 kyr BP and during the last millennium-deviate from expected trends if insolation was the sole forcing mechanism. Previously proposed mechanisms linking ENSO to latitudinal displacement of the ITCZ and ocean-atmospheric variabilities in other ocean basins appear to play an additional role in modulating Holocene ENSO development, as demonstrated by statistically significant correlations between the revised Laguna Pallcacocha flood history and proxy records from the Atlantic.

2.1 Introduction

Despite the significance of the El Niño Southern Oscillation (ENSO) to global climate and human society, its behavior over the course of the Holocene remains widely debated. Existing proxy records from lake sediments (Rodbell et al. 1999, Moy et al. 2002, Thompson et al. 2017, Zhang et al. 2014), foraminifera (Koutavas and Joanides 2012), bivalve shells (Carré et al. 2014) and speleothems (Chen et al. 2016, Griffiths et al. 2020), as well as evidence from modelling experiments (e.g. Chen et al. 2019, Zheng et al. 2008) indicate reduced El Niño activity during the middle Holocene (7.5-4 kyr BP). However, other high-resolution proxy records from coral skeletons (Cobb et al. 2013, Emile-Geay et al. 2016) and molluscan assemblages (Emile-Geay et al. 2016) highlight the pronounced variability of past ENSO changes. Further demonstrating the complexity of pre-instrumental ENSO variability, continuous, high resolution proxy records from tree-ring and speleothem records have yet to yield a conclusive picture of ENSO variability during the Little Ice Age (LIA, 1450-1850 AD) and Medieval Climate Anomaly (MCA, 900-1300 AD) (Henke et al. 2017). For instance, while some records indicate increased El Niño activity, or persistent El Niño-like conditions during the Medieval Climate Anomaly (MCA) (Tan et al. 2019), other records indicate the opposite pattern (Denniston et al. 2015). Reconciling these divergent conclusions is a crucial and necessary step for better understanding long-term forcing of ENSO variability.

Several studies have implicated insolation as a major driver of El Niño frequency. Modelling studies and observational data suggest an inverse relationship between seasonal temperature contrast and ENSO activity, as enhanced seasonality strengthens Pacific Walker Circulation, and suppresses the development of El Niño events (An and Choi 2014, Zheng et al. 2008). While some proxy records have supported this mechanism (McGregor et al. 2013), a Pacific-wide compilation

of sub-annually resolved $\delta^{18}O_{aragonite}$ records dispute such a mechanism (Emile-Geay 2016a). Other studies have indicated that higher equatorial September (White et al. 2018, Dang et al. 2020) and June (Dang et al. 2020) insolation enhances the zonal tropical Pacific thermal gradient and suppresses the development of El Niño events via shoaling of the eastern Pacific thermocline. However, high-resolution proxy records from the core ENSO region (equatorial tropical Pacific) demonstrate the importance of centennial-scale shifts in ENSO variability which cannot be explained solely by changes in insolation (Cobb et al. 2013). Abrupt, stepwise southward shifts in the intertropical convergence zone (ITCZ) (Haug et al. 2001), explosive volcanism (Stevenson et al. 2016) and teleconnections to the Atlantic basin (Pausata et al. 2017, Levine et al. 2017) have all been proposed as additional drivers of ENSO variability.

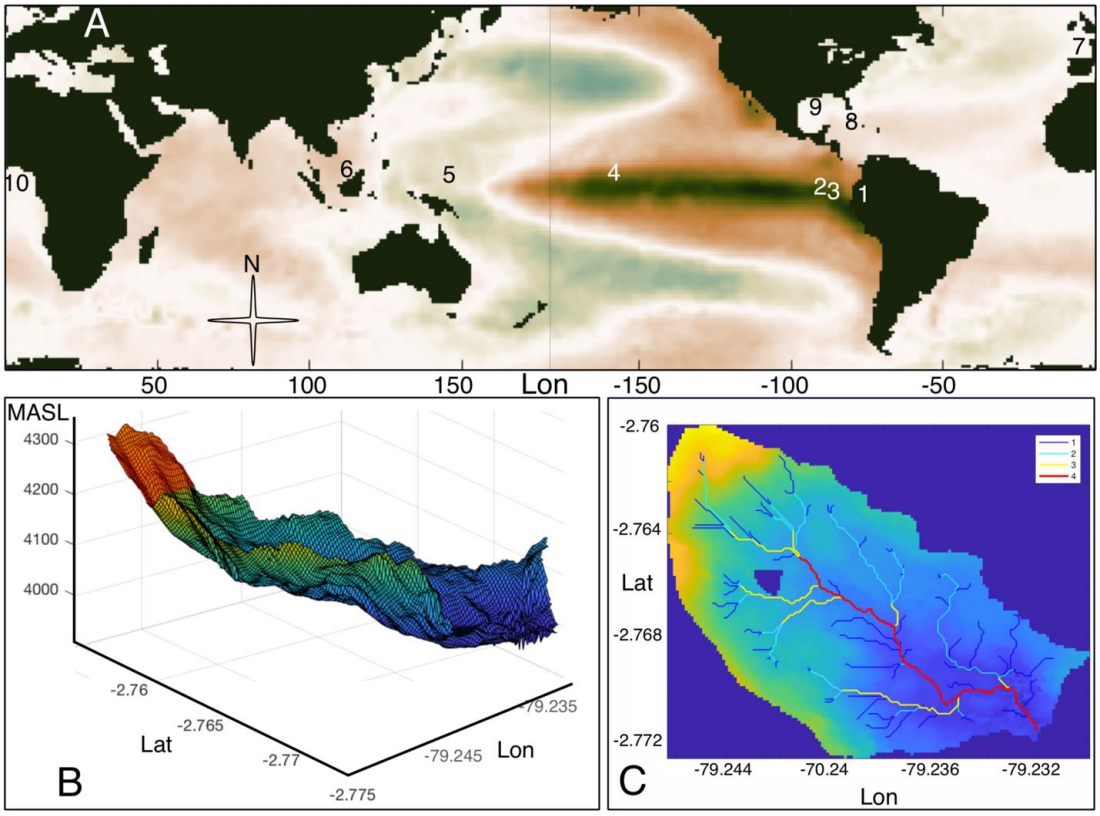

Figure 1. Setting of Laguna Pallcacocha and other ENSO proxy reconstructions. (A) First EOF of sea surface temperatures (SST), 60N to 60S. Location of ENSO-sensitive proxies discussed in text are designated as follows: (1) Laguna Pallcacocha (this study), (2) El Junco, Galapagos (Zhang et al. 2014), (3) Marine Core V21-30 (Koutavas and Joanides, 2012), (4) Northern Line Islands coral chronology (Grothe et al. 2020), (5) Indo-Pacific Warm Pool marine core compilation (Dang et al. 2020), and (6) Bukit Assam Cave, Borneo (Chen et al. 2016). Proxies sensitive to Atlantic phenomena are designated as (7) Kaite Cave, Spain (Dominguez-Villar et al. 2017), (8) Florida Straits marine core (Schmidt et al. 2012), (9) Gulf of Mexico marine core (Poore et al. 2003), and (10) Gulf of Guinea core GEO-B4509 (Collins et al. 2017). Plotting conducted using the Climate Data Toolbox for MATLAB (Greene et al. 2019) (B) 3D rendering of the Laguna Pallcacocha watershed. The transparent red outline at headwall shows the zone of loose, clastic sediment production. (C) Horton stream order map of the Laguna Pallcacocha watershed, showing the network of channels which connect the zone of clastic sediment production to the lake. Color of channel indicates Horton stream order.

Several studies have sought to re-evaluate the clastic alluviation signal preserved in Laguna Pallcacocha's sedimentary record using different approaches. Schneider et. al (2018) found no significant relationship between flood driven alluviation events and instrumental El Niño records. This study failed to find clastic laminae corresponding to the very strong 1982/83 and 1997/98 CE El Niño events in surface cores. However, the cores were collected after significant landscape disturbance in the watershed and repeated coring of the small deep basin of the lake. Additionally,

using a network of meteorological stations located up to 50km east of the Andean divide, Schneider et al. (2018) found no significant relationship between 24 and 36 hour precipitation maxima and El Niño conditions. The only station proximal (<5km) to Pallcacocha, however, covers only 4 years (2012-2016 CE). More recent work, however, has concluded that alluviation at Laguna Pallcacocha is, in fact, closely tied to El Niño events when sea surface temperature (SST) warming is centered in the eastern Pacific and coastal South America (EP and COA events, respectively). During EP and COA events, westerly winds and cloudburst rainfall occur at Laguna Pallcacocha, but not at a nearby weather station several kilometers east of and more than 500m lower than the lake (Hagemans et al. 2021). This is consistent with a meso-scale modelling experiment which suggests that EP and COA ENSO events drive intense hourly precipitation maxima, while having relatively little impact on overall precipitation totals (Kiefer and Karamperidou, 2019). These convective cloudbursts are responsible for generating alluviation and clastic sedimentation in the Laguna Pallcacocha sedimentary record.

Additional work is needed on the Laguna Pallcacocha record to directly link watershed-scale erosion to climate, evaluate how the record may record newly recognized configurations of ENSO, and compare the clastic stratigraphy to the growing body of paleo-ENSO proxy records. The original work was done prior to advances in age modelling and suffers from limited chronological control over the past millennium. Additionally, the visible color stratigraphy may in part reflect a variety of environmental and ecological processes unrelated to rapid depositional events. High-resolution XRF-derived elemental content offers the advantage of directly linking sedimentary structures with erosion and deposition in the watershed. Few, if any, Holocene ENSO reconstructions have both the temporal resolution to record individual El Niño events and provide continuous coverage over the Holocene. Most modelling experiments only cover discrete,

centennial-scale windows of climate variability, hindering an exploration of ENSO evolution and its relationship to external factors (Emile-Geay et al. 2016a). As such, improving the temporal constraints and refining the interpretation of the Laguna Pallcacocha record is vital to the future of paleo-ENSO research.

Here, we address critical questions regarding the Pallcacocha record. We use surface cores recovered in 1993, 1998, 2014, 2017, and 2018 CE to examine the relationship between El Niño events, environmental change, and clastic sedimentation in the basin. By using ^{137}Cs and ^{210}Pb assays, we improved the chronology over the recent past, and can directly compare depositional events in the stratigraphy to instrumental and documentary records of warming in the eastern tropical Pacific. Third, and most significantly, we present a high-resolution record of XRF-derived elemental composition to directly link clastic debris flow events to sedimentation during the Holocene. The resultant flood chronology, interpreted as showing long-term changes in coastal and eastern Pacific El Niño events, sheds new light on the development of ENSO over the Holocene and can be used to investigate potential forcing mechanisms.

2.2 Methods

2.2.1 Core Collection

Surface cores were collected using a 5.9cm diameter polycarbonate tube and piston in 1999, 2017, and 2018 and transported intact to the laboratory using sodium polyacrylate to stabilize the surface (Fig. 2). A freeze core was collected in 2017 to ensure in-situ preservation of

sediment (Fig. 2). Full Holocene sections were recovered with a Livingstone corer in 1993 and 1999, however sediment-water interfaces were disturbed during these coring operations. All cores described here were collected from the deepest (~8 meter) basin identified by Rodbell et. al (1999).

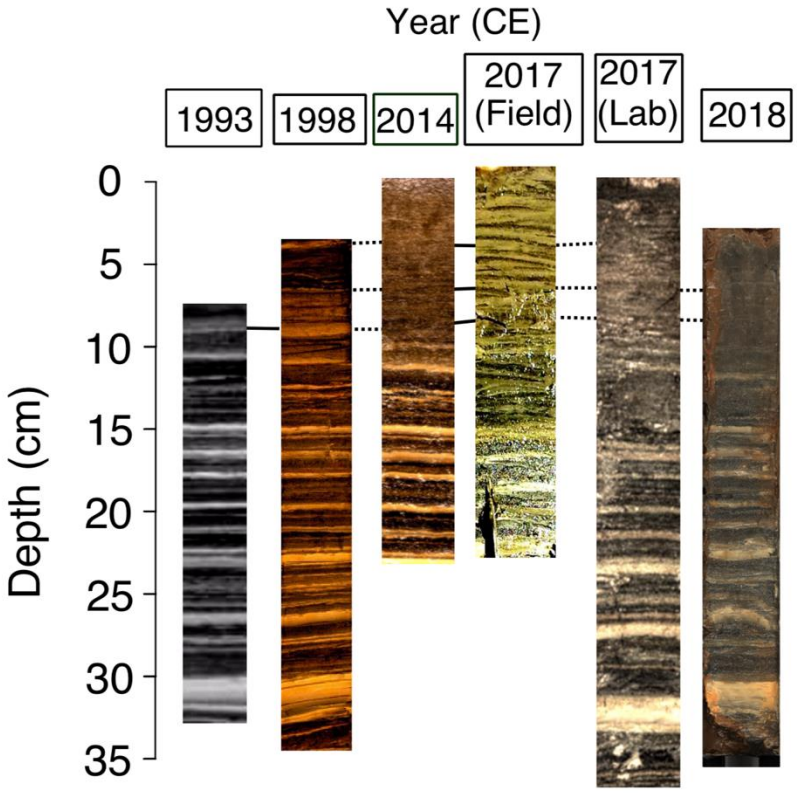

Figure 2. Pallcacocha surface cores taken between 1993 and 2018. Cores show common visual features beneath roughly 15cm, but not necessarily at the core tops. Solid black lines indicate stratigraphic features which are reproduced and correlated based on visual identification, while dashed black lines indicate features which are not.

2.2.2 Chronology

We constrained the ages of surface sediments using an unpublished ^{210}Pb chronology from the 1999 surface core and a ^{210}Pb chronology from a surface core collected in 2017, modelled

using both a Constant Rate of Supply (CRS) and Constant Flux Constant Sedimentation (CFCS) model after eliminating clastic layers following the assumption that they were essentially instantaneous events (Arnaud et. al 2002) (Fig. 3). In addition, 5 radiocarbon dates were measured and combined with the original 14 radiocarbon dates from Rodbell et. al (1999). Two of them were measured at the Penn State Radiocarbon Laboratory on a National Electrostatics Corporation 500kV 1.5SDH-1 Compact Accelerator Mass Spectrometer and three were measured at the W.M Keck Carbon Cycle Accelerator Mass Spectrometer at the University of California Irvine on a similar system. All samples were prepared with a standard acid-base-acid method (Santos et al. 2013). A well-dated tephrochronology from the region provides additional chronological tie-points (Rodbell et. al 2002) and allows for depth adjustments to account for the amount the cores have shrunk over the past 20 years. A complete age-depth model, with age uncertainty, was developed using the Bchron software package (Parnell et. al 2021) and the IntCal20 calibration curve (Hogg et al. 2020). The initial age model developed by Rodbell et al. (1999) and further advanced by Moy et al. (2002) uses a Constant Carbon Accumulation (CCA) model to account for rapid depositional events in the core. While the relatively short-lived depositional events surely alter instantaneous sedimentation rate, the sequence in its entirety displays a relatively constant sedimentation rate (Fig. 3), making age modelling techniques that account for rapid alluvial events unnecessary over the timescale of the full record.

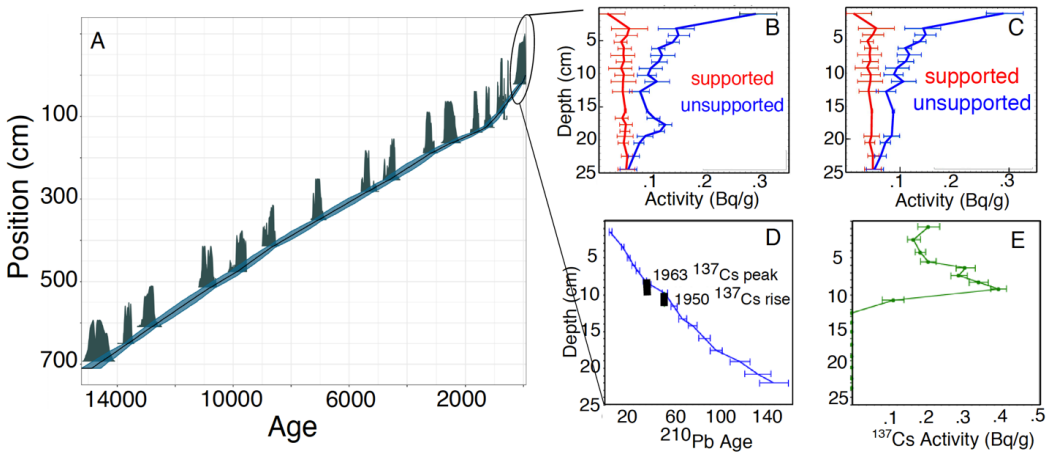

Figure 3. Chronological control for Laguna Pallcacocha (A) Full Pallcacocha BChron age model, with the inclusion of 20 new 210Pb and 5 new 14C dates over the last millennium. (B) The 210Pb profile from 1998 Laguna Pallcacocha surface core. Red line shows supported ^{210}Pb curve and blue line shows unsupported ^{210}Pb curve. (C) The same as (B) but with rapid depositional events excluded (per Arnaud et al. 2002). (D) ^{210}Pb and ^{137}Cs derived age model for 1998 Pallcacocha surface core and (E) ^{137}Cs profile from the 1998 Pallcacocha surface core.

2.2.3 X-Ray Fluorescence and Sedimentology

In 2017 the Livingstone cores collected in 1999 were scanned with an ITRAX XRF Core scanner at the Large Lakes Observatory at the University of Minnesota Duluth, which provides elemental counts for most elements less than atomic number 93. The cores were scanned at 0.1 cm resolution with a 15 second dwell time. Total organic content (TOC) was measured by loss on ignition and converted to TOC via a transfer function (Rodbell et al. 1999).

2.3 Results

2.3.1 Laguna Pallcacocha XRF record

Al, Si, K, and Rb are all positively correlated with one another for the entirety of the record (Fig. 4). Higher counts are associated with the light-colored clastic laminae and the inorganic (glacial) silt at the base of the sequence. The ratio of incoherent to coherent scatter (inc/coh) is associated with organic matter in the core and is significantly anti-correlated with Al, Si, Rb, and Ti. Unlike other lithophilic elements commonly derived from the catchment (Davies et al. 2015), Ti is not substantially higher during the deglacial period. We performed a principal component analysis on the variables mentioned above. The first principal component (PC1) of the XRF data (Figure 4 B and C) is closely related to Al, Si, K, and Rb, consistent with the results of Schneider et al. 2018, and is interpreted as a proxy for alluvial deposits. The PC1 is the only significant component in the dataset, comprising 60% of the total variance. We interpret the PC1, and the elements positively correlated with it, as representing erosional input from clastic sediments in the catchment. PC1 is consistently higher prior to approximately 11.5 kyr BP, when sediments are characteristic of inorganic glacial till. The spacing of the high-frequency peaks, which we interpret as rapid alluviation events, represents the frequency of flooding over the course of the Holocene. In order to better visualize the frequency of flood events, peaks in the XRF PC1 were binned in 100 year intervals per the methodology of Moy et al. (2002) (Fig. 12). Additionally, the return interval of flood events (i.e. the years between flood layers) were also calculated to emphasize higher-frequency variability (Fig. 13). Floods during the early Holocene tended to occur between roughly 8-12 times per century for an approximately 10-year return interval. During the middle Holocene, flood frequency decreased to approximately between 5-8 events per century

(approximately 20 year return intervals). After approximately 4 kyr BP, flood frequency begins to increase, entering the modern ENSO frequency band (sub-decadal return interval, approximately 12-16 events per century) at about 2 kyr BP.

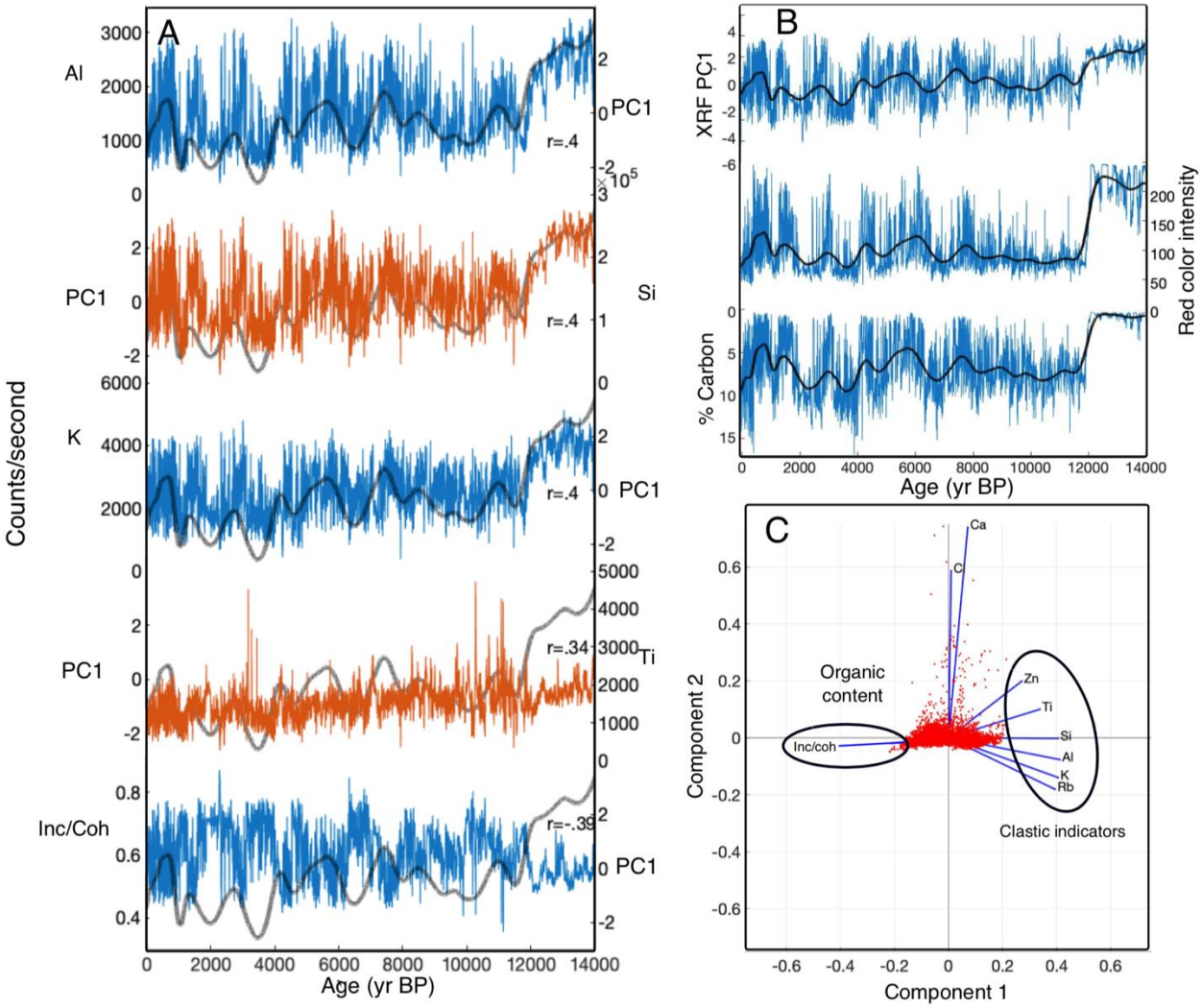

Figure 4. Laguna Pallcacocha XRF results. (A) XRF-derived element counts from Laguna Pallcacocha, 100 point smoothing filter of the XRF PC1 is shown as transparent gray line. R values indicate correlation of each element with the PC1. (B) XRF PC1, organic carbon content, and red color intensity from Laguna Pallcacocha with 100-point smoothing filters (black lines). (C) Biplot of major elements from XRF Principal Component Analysis.

When both proxies are placed on the same (new) depth scale, the PC1 closely matches the variability in red color intensity values throughout the surface core (Fig. 5) and during the late to

middle Holocene, but the two time series become dissimilar at greater depths (Figs. 6 and 7). Most notably, while the PC1 captures significant sub-decadal scale variability during the early Holocene, these variations in the red intensity data are either absent or the amplitude is significantly reduced (Fig. 6 and 7). The correlation between the PC1 and red color intensity for the period 0-7 kyr BP is 0.58 ($p<.05$). However, during the period 7-11 kyr BP, the correlation coefficient is reduced to 0.33 ($p<<.05$). The cores have shrunk in the two decades between the initial collection and recent XRF analyses, and even millimeter-scale discrepancies in the depth scale can create destructive interference between the two time series, likely reducing correlations between the color record and XRF record. A cross-wavelet analysis between the red color intensity record and the XRF PC1 reveals the importance of using elemental data as opposed to sediment color (Fig. 6). From the beginning of the Holocene to roughly 10 kyr BP both time series show few significant spectral properties. Between 10 and 7 kyr BP, the XRF PC1 shows significant periodicities in the 8-32 year waveband, at lower frequencies than the modern ENSO waveband, while the red color intensity data shows no such periodicity. Both time series share a common significance at a 32-year waveband between 7 and 5 kyr BP. The updated age model indicates maximum flood event frequency in both the XRF and red color intensity record occurs between 900-1200 CE, during the MCA. The subsequent LIA (1450-1850 CE) shows fewer flooding events than the MCA, but still more frequent El Niño events than most of the Holocene.

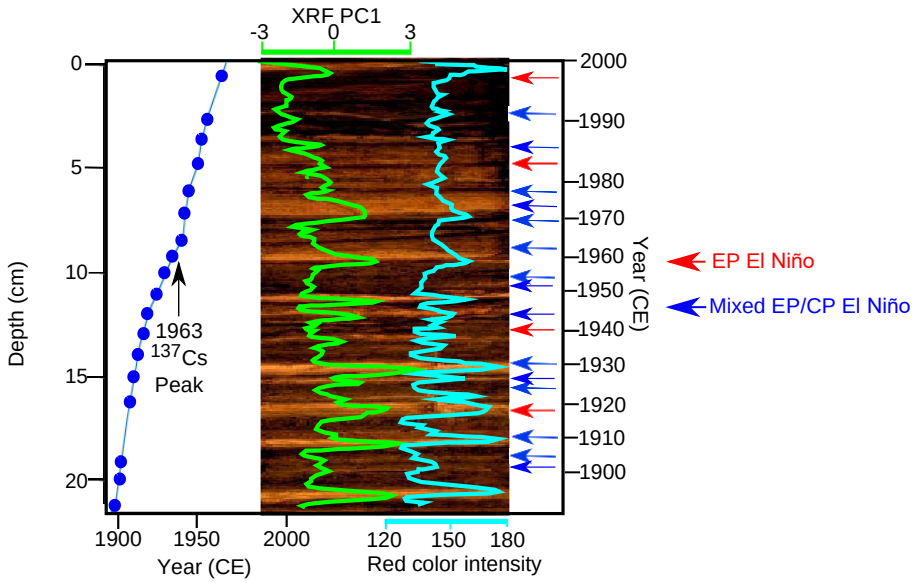

Figure 5. 1999 surface core image with new 210Pb and 137Cs age model. Blue dots indicate depths at which assays were conducted. Grayscale (blue line) and XRF PC1 (green line) show close agreement with one another. Light colored clastic laminae, captured by both metrics, show close correlation with Eastern Pacific El Niño events, marked by red arrows and mixed EP/CP events by blue arrows, according to the classification scheme of Andreoli et al. (2017), which extends to CE 1902.

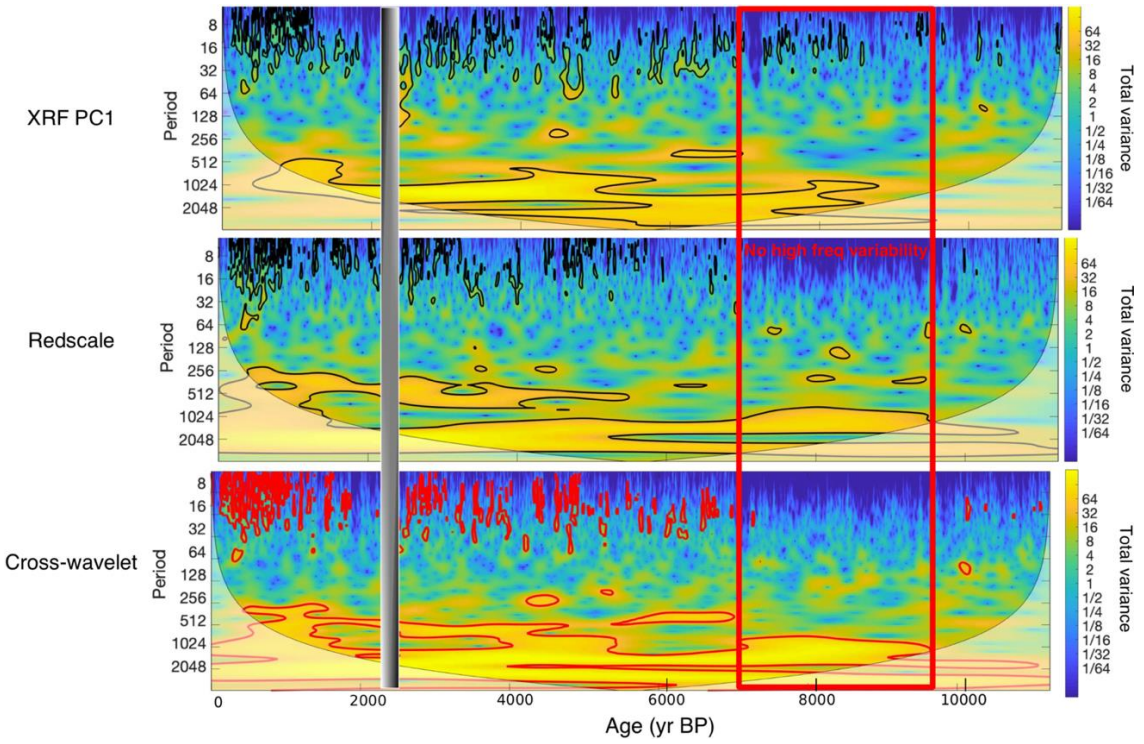

Figure 6. Wavelet analyses for (A) XRF PC1, (B) Red color intensity, and (C) the cross wavelet of (A) and (B). Gray vertical box at roughly 2.2 kyr BP represents a deformational structure related to a tephra deposit. Raw time series's were first treated with the "Gaussianize" transform developed by Emile-Geay and Tingley (2016b) to account for non-linearities in the proxy data. Morlet wavelet and cross-wavelets were caried out using the code for Matlab developed by Grinsted et al. 2004.

Previous work has indicated that organic carbon in the sedimentary sequence is dominantly terrestrial in origin (Fig. 8, Rodbell et al. 1999). Both the proportion and the rate of organic carbon deposition is higher during the early Holocene (Fig. 9). Perhaps most importantly, negative excursions in organic carbon concentration, indicating rapid alluviation events, are substantially more organic carbon-rich during the early Holocene than during the middle Holocene (Fig. 9). Because organic carbon in the sediment is primarily terrestrial, the increased proportion of carbon in the early Holocene is consistent with enhanced erosion of organic material diluting inorganic clastic sediment during rapid alluvial events. This dilution would prevent alluvial deposits from being identified in the red color intensity and grayscale datasets, and prevent a high-frequency signal from registering during the early Holocene.

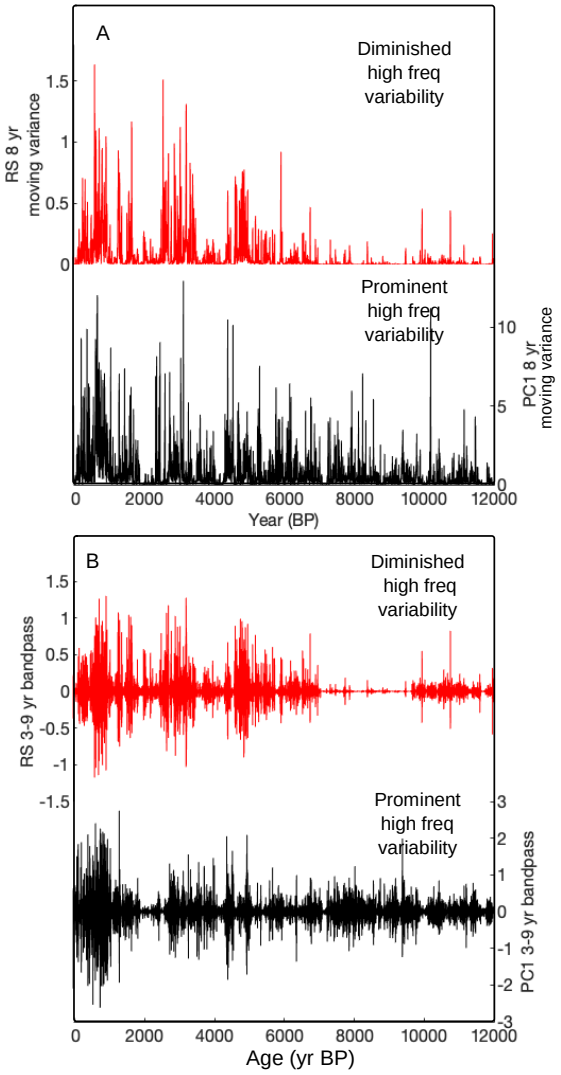

Figure 7. (A) ENSO-scale moving variance of red color intensity and XRF PC1 records and (B) 3-9 year bandpass filter of red color intensity and PC1 from 0-12 kyr BP. Gray boxes indicate early Holocene period where high-frequency variability is muted in the color record but apparent in XRF PC1.

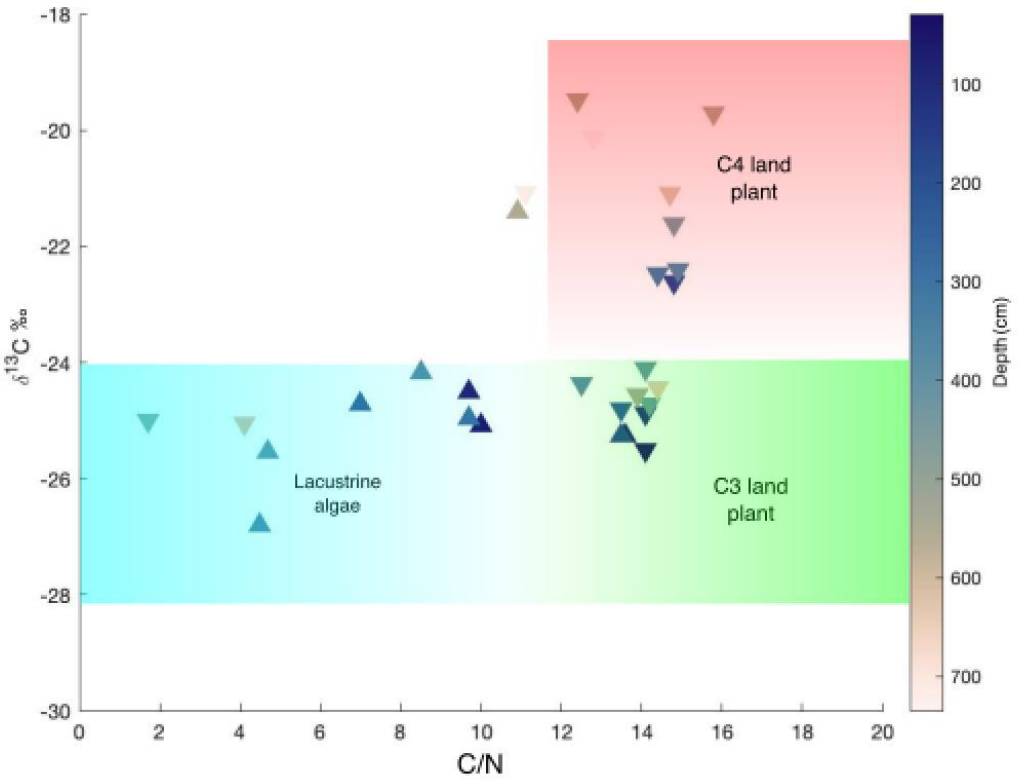

Figure 8. Organic carbon and TOC/TN ratios indicate primarily terrestrial delivery of organic carbon into the catchment, particularly during the early Holocene.

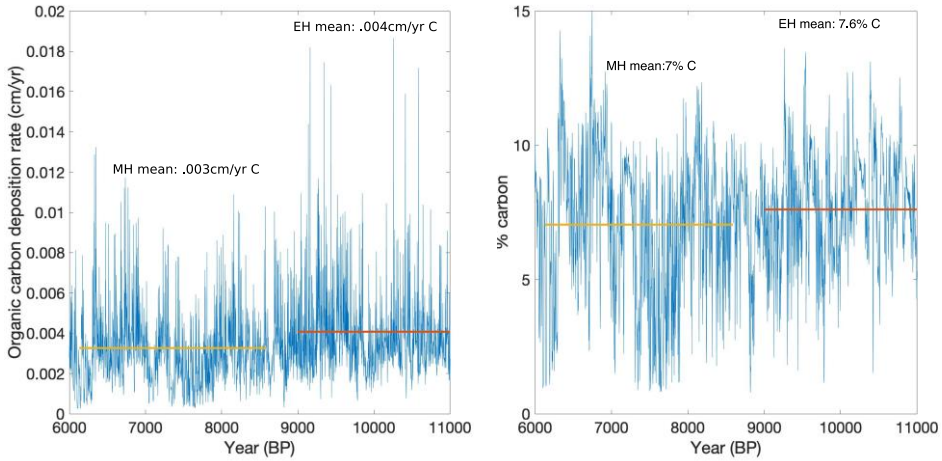

Figure 9. Laguna Pallcacocha organic content between 11-6 kyr BP. (A) The rate of deposition of organic carbon during the early and middle Holocene. Red line indicates 11000-9000 BP mean and yellow line indicates 6000-8000 BP mean. (B) Percent organic carbon during the early and middle Holocene. Red line indicates 11000-9000 BP mean and yellow line indicates 6000-8000 BP mean. (C) Local minima in organic carbon, indicative of clastic depositional layers, during the early and middle Holocene.

2.3.2 Recent Sedimentation at Laguna Pallcacocha and Surroundings

Recent landscape disturbance and repeated coring within the small lake basin preclude the correlation of the uppermost Pallcacocha stratigraphy to instrumental climate records after 1999. While surface cores taken over the past 25 years are consistently reproducible below 15cm, clastic layers above this boundary are not common to all cores (Fig. 2). A core taken in 1999, shortly after the very strong 1997/1998 EP El Niño shows a clear clastic layer at the top (Figs. 2 and 5). However, the surface core presented in Schneider et al. taken in 2014 does not show this flood laminae, as well as several preceding layers (Fig. 2). Three potentially overlapping mechanisms can explain these differences. (1) Kees Noreen (Utrecht University, written communication 2020) documents a tenfold increase in the presence of the eutrophic indicator diatom species *discostella stelligera* (Bush et. al 2017) beginning in 1994. This shift occurs concurrently with the 1994 paving of Highway E-582, the only land route connecting the major cities of Guayaquil and Cuenca, which runs through Cajas National Park and within 2 km of Laguna Pallcacocha. This has drastically enhanced vehicle traffic through the park, particularly over the past decade (Bandowe et al. 2018). Productivity has long been shown to influence sedimentary color (Hayes and Anthony, 1958), and the high flux of aquatic organic matter to the lakebed would likely dilute the clastic signal and may "mask" visually identifiable clastic layers. This road construction, as well as the observed proliferation of foot and mule paths connecting communities north of the Pallcacocha catchment to the highway, have produced documented impacts on local ecosystems (Astudillo et. al 2014). However, potential eutrophication and productivity proxies (Si/Ti and Mn/Fe ratios) do not indicate that changing trophic conditions have drastically altered the top of the sedimentary record. Oxidation reactions which mask visually identifiable layers after core collection may play a significant role in changing the color of core tops. A field photograph of the 2017 freeze core

shows visible stratigraphy which is absent in subsequent laboratory photographs (Fig. 2), consistent with this suggestion. (2) It is possible that the repeated coring of the Pallcacocha basin (more than a dozen cores have been extracted from a depocenter of roughly 1000 m^2) may have created an uneven and artificially mixed surface sediment layer. The 2014 cores collected by Schneider et al. may have been taken from an area of the deep basin which has been disrupted over the past 20 years of research through repeated coring and anchoring efforts. Indeed, cores collected in 1993 and 1998 show several clear clastic layers which cannot be reproduced in all subsequent cores (Fig. 2). (3) Lastly, Hagemans et al. (2021) show recent (post 1998) debris flow events resulted in a channel avulsion which redirected the primary pathway for coarse sediment to be deposited away from the previous lake depocenter. This recent reworking of channel networks may confound the detection of modern depositional events. The size of the alluvial fan, and lack of geomorphic evidence for additional prominent channels in the watershed (Fig. 1C) indicate that alternative pathways of sedimentation have been minimal over the course of the Holocene. In sum, the combination of recent catchment alterations, sediment disturbance and changes in trophic status require that we limit quantitative correlations to historical and instrumental records of ENSO prior to 1999.

The addition of ^{210}Pb assays and ^{14}C dates to the surface sediment core collected in 1999 substantially decreases age uncertainty over the past millennium, allowing for comparison with instrumental and historical evidence of El Niño events since 1550 CE (Fig. 10). Between 1550 and 1900 CE, the period covered by several documentary reconstructions of El Niño events (Quinn et al. 1987, Garcia-Herrera et al. 2008), the Laguna Pallcacocha record documents 45 distinct flood laminae, one more than the number of El Niño events documented by Garcia-Herrera et al. (2008), when multi-year events are counted as a single El Niño (Fig. 10). This is justified because multi-

year events are likely indistinguishable from one flood deposit given the sub-millimeter scale of non-clastic sedimentation that would occur between floods. The documentary evidence provided by Garcia-Herrera et al. (2008) is the most reliable source to compare to recent sedimentation at Pallcacocha because of their shared sensitivity to coastal and eastern Pacific ENSO events. The Garcia-Herrera et al. (2008) chronology incorporates primary source evidence from the Spanish colonial administration in the city of Trujillo in northern Peru which is arid during non-El Niño years and receives precipitation in years with COA and EP El Niño events. The shared sensitivity to COA and EP events is reflected in the strong visual match between documented El Niño's and peaks in the XRF PC1 (Fig. 5, Fig. 10). While age uncertainty precludes the attribution of individual flood laminae to a specific year, the cumulative number of El Niño's recorded by Pallcacocha and the Garcia-Herrera et al. (2008) chronology between 1550 and 1990 CE is very similar (Fig. 10). The period when the two cumulative event distributions diverge occur between the thickest clastic deposits over this period. Because these deposits occur approximately instantaneously, they distort the age model on interannual timescales (Moy et al. 2002). While the subtraction of clastic layers is justified over the ^{210}Pb chronology due to the high number of dates, further manual adjustment of the age model on interannual timescales is not justified. Despite these challenges, the remarkable consistency between documentary evidence and clastic sedimentation supports the notion of EP and COA El Niño events driving clastic sedimentation at Laguna Pallcacocha.

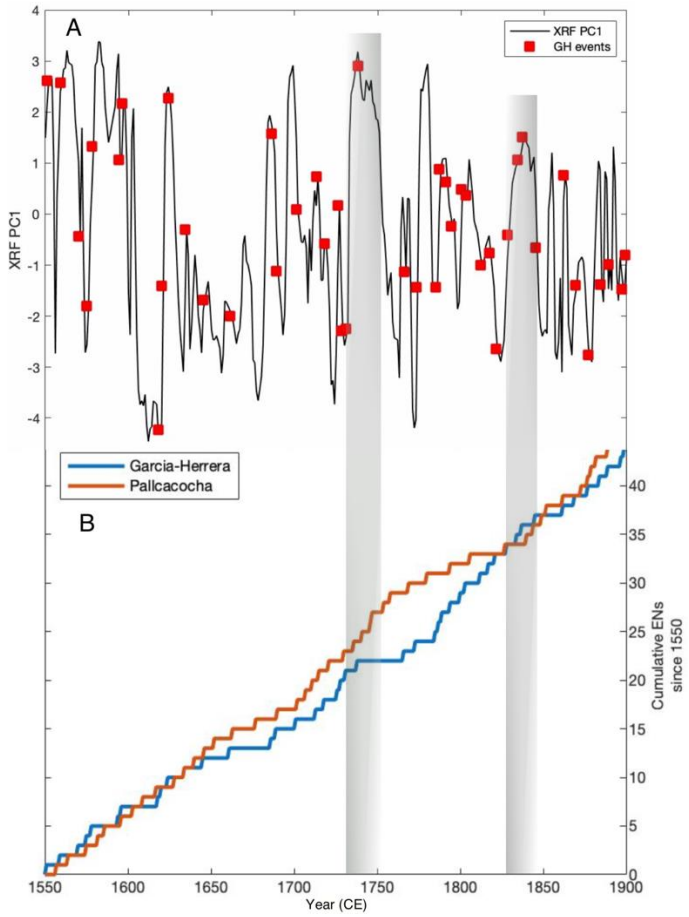

Figure 10. Comparison of Laguna Pallcacocha flood deposits with documentary evidence for El Niño events. (A) XRF PC1 (black line) and documentary evidence of El Niño events from primary documentary evidence detailed in Garcia-Herrera (2008) (red squarers). Peaks in XRF PC1 indicate clastic layers. While age uncertainty precludes absolute identification of the years in which clastic layers were deposited, the number of El Niño's (when counting events in concurrent years as a single event-see text) is almost identical (44 in the documentary evidence, 45 in the sedimentary record). (B) The cumulative number of El Niño events documented by Laguna Pallcacocha (red line) and the Garcia-Herrera El Niño chronology (blue line) between 1550 and 1900, the period covered by both records. Transparent gray boxes show thick layers of rapidly deposited clastic alluviation which occur coevally with divergence between the Laguna Pallcacocha and Garcia-Herrera event chronologies.

2.4 Discussion

2.4.1 The Relationship between Geochemical Data, Sediment Color, and Landscape Change

Rapid alluviation events in the Laguna Pallcacocha sedimentary record are well represented by the first principal component (PC1) of the XRF data. Peaks in the PC1 represent abrupt deposition of clastic material resulting from El Niño-driven convective storm bursts consistent with the interpretations of Rodbell et al. (1999), Moy et al. (2002), and Hagemans et al. (2021) (Fig. 5). Measurements of Al, Si, K, and Rb in counts per second (cps) are all closely correlated with the XRF PC1 and are commonly used to identify clastic flood deposits in lacustrine settings (e.g. Berntsson et. al 2014). Additionally, each of these elements is significantly anti-correlated with Inc/Coh scatter, a commonly used proxy for organic content, as Carbon is too light to be detected by traditional scanning XRF techniques. Examination of the surface cores show that the visibly identifiable, fining upward sequences attributed to deposition by hyperpycnal flows by Rodbell et. al (1999) also appear as peaks in the PC1 (Fig. 5). Individual element counts each contain specific drawbacks, making the use of techniques like PCA preferable. While silica is an important component of the underlying ignimbrite bedrock, as evidenced by its elevated levels in glacial sediments, it can also reflect diatom frustule production (Peinerud et al. 2000). Titanium is an often-reliable indicator of terrestrial input (e.g., Haug et al. 2001), but it is also associated with larger grain size minerals of high specific gravity (Brown 2015). This may explain why it is less abundant than the other detrital elements during the late glacial period, when sedimentation was primarily fine-grained glacial flour (Fig. 11). Catchment glaciers had completely melted by 12 kyr BP (Rodbell et al. 2008) making flood-driven alluviation the major delivery mechanism for clastic

material through the Holocene. The use of PCA overcomes the limitations described above, and the linear combination of variables represented by the PC1 is a more reliable indicator of flood frequency from Laguna Pallcacocha than any single element.

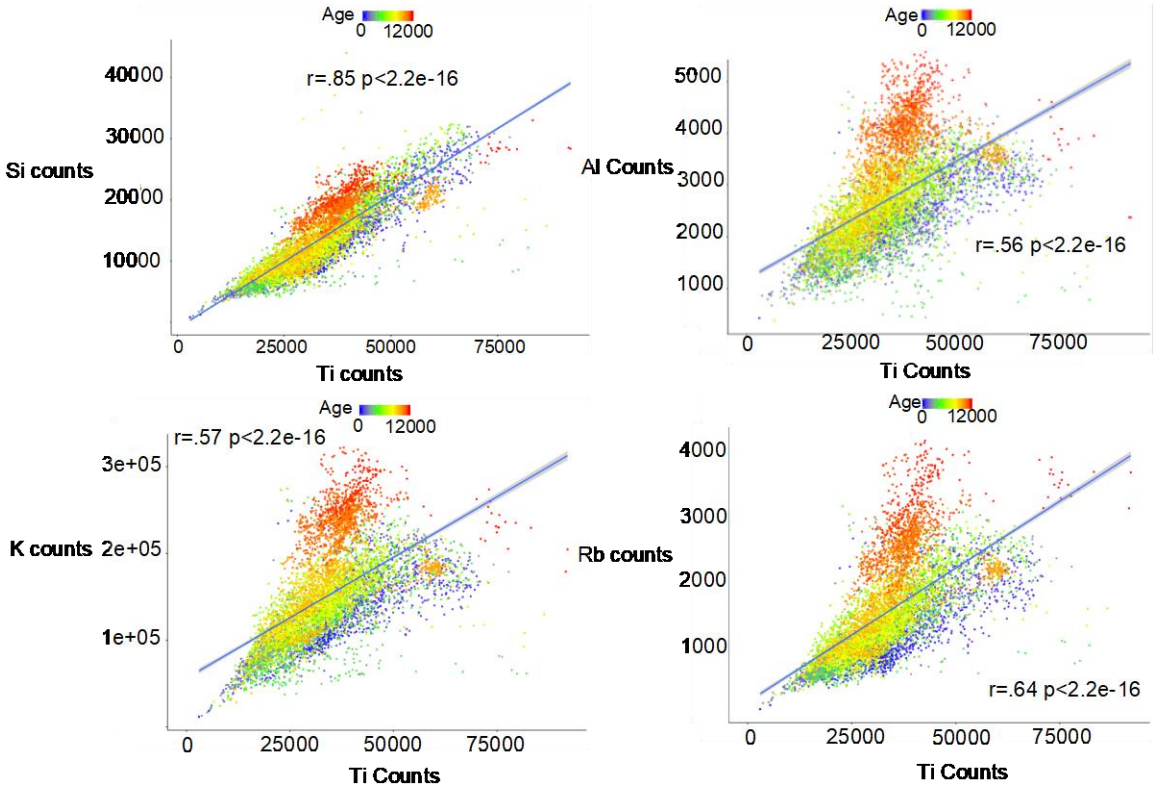

Figure 11. Relationship between Ti and other major elements. Strong positive correlations between Ti and other major clastic elements. Notably, the glacial portion of the record (roughly 11,700 to 15,000 yr BP) is depleted with respect to Ti. Ti is often associated with coarser grained mineral assemblages which may have been largely absent in glacial flour.

Why, then, is color reliable indicator of clastic deposition during the middle and late Holocene, but not during the early Holocene? Unlike elemental composition, which is a direct function of mineralogy, color is influenced by a variety of environmental and limnological processes. Laminae discernable by color differences may have been formed less frequently during the deglacial period and early Holocene because of limited landscape stability. At present, high-altitude páramo ecosystems dominate the highlands of Cajas National Park, increasing soil carbon stocks and soil stability, even in steep watersheds (Minaya et al. 2016). Pollen records from the

region indicate that these ecosystems have changed markedly over the course of the Holocene (Hansen et. al 2003). The transition to a páramo ecosystem resembling the modern environment occurred at 7,500 yr BP, coincident with the alignment between the XRF and color records. The early Holocene in Cajas National Park was marked by the presence of a dry season and increased biomass burning based on analyses of pollen and charcoal (Hansen et al. 2003). This pattern is reproduced at Laguna Llavillucu, a lower elevation site (3115m a.s.l.) several kilometers east of Pallcacocha (Nascimento et al. 2020). The transition from a deglacial landscape to one dominated by páramo vegetation increased the stability of the watershed and hence the amount of erosion. Prior to the establishment of páramo vegetation at Laguna Pallcacocha, flood deposits contained higher proportions of terrestrial organic matter than during the middle and late Holocene when deep rooted tussock grasses protected soil from erosion (Fig. 8). Carbon isotopes and elevated TOC/TN ratios of organic matter indicate a predominantly terrestrial source. Generally elevated carbon isotope values during the early Holocene indicates a greater proportion of C4 to C3 land plants, a common phenomenon in postglacial Andean páramo ecosystems (Boom et al. 2001) (Fig. 8). Additionally, the transport of loose clastic material from the headwall where it is produced into the lake requires a network of channels and a prograding delta fan that developed over time. Mechanical abrasion continues to carve existing channels (Whipple et. al 2000), creating stream networks of sufficient competence and capacity to transport enough clastic material to register as visual laminae. Temporary sediment storage sites exist further upslope, forming much of the existing delta fan (Hagemans et. al, 2021). While abrupt clastic sedimentation is still apparent in scanning XRF data, early Holocene flood deposits are less readily identifiable by red color intensity due to terrestrial ecosystem changes and landscape development.

2.4.2 Holocene History of El Niño Preserved in Laguna Pallcacocha Sediments

Changing orbital configurations have long been invoked to explain the apparent suppression of El Niño events in the early and (particularly) middle Holocene (Chen et al. 2019), a pattern broadly supported by the new XRF data from Pallcacocha. White et al. (2018) call attention to the role of enhanced equatorial June insolation in decreasing the depth of the eastern Pacific thermocline in the early and middle Holocene, dampening the upwelling feedback and hindering the formation of El Niño events. A compilation of marine sedimentary records from the Indo-Pacific Warm Pool (IPWP) highlights two significant orbital factors which limited El Niño activity by shoaling the thermocline and intensifying Walker Circulation prior to 4 kyr BP (Dang et al. 2020). The early Holocene thermocline warming is thought to be driven by June equatorial insolation maxima while the middle Holocene was driven by equatorial Oct-Dec insolation maxima (Dang et al. 2020), which inhibited the formation of El Niño events during their growth phase (Chen et al. 2016). Insolation driven seasonal contrast also peaks during the early Holocene, and has been suggested to hinder El Niño development by exaggerating the zonal tropical Pacific temperature gradient, thereby accelerating Walker Circulation (McGregor et al. 2014). The new Laguna Pallcacocha XRF record, and others from the tropical Pacific (Fig. 12), indicate reductions in El Niño activity that are consistent with each mechanism described, suggesting that multiple orbital factors have been crucial to the development of the ENSO over the Holocene.

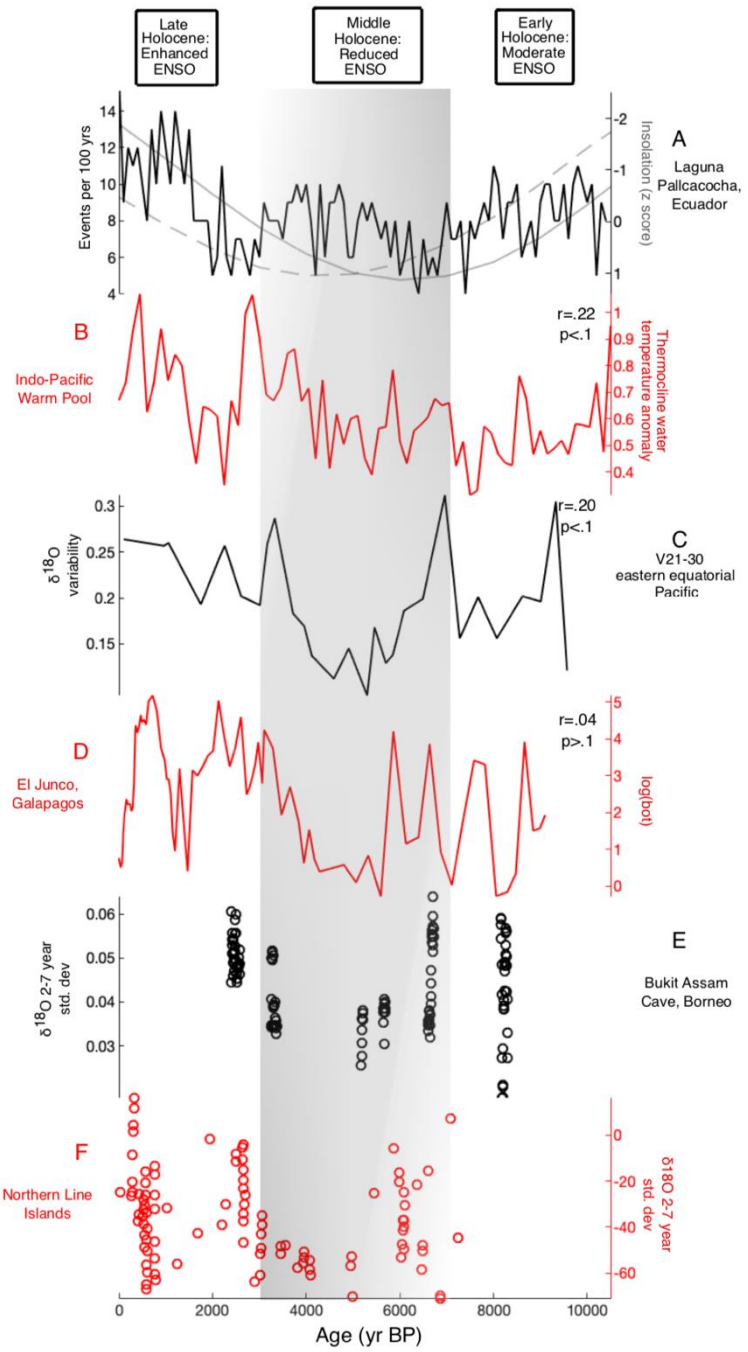

Figure 12. Compilation of tropical Pacific ENSO records from 10,500 BP to present. Records indicate moderate ENSO activity in the early Holocene, reduced ENSO activity in the middle Holocene and enhanced ENSO during the late Holocene. Transparent gray box indicates middle Holocene period when continuous (A-D) and discontinuous (E and F) proxies indicate reduced ENSO variability. (A) El Niño events per 100 years from Laguna Pallcacocha (this study). Dashed gray line indicates equatorial Oct-Dec and solid gray line indicates equatorial seasonal insolation contrast (Mar-May vs. Oct-Dec). (B). Indo-Pacific Warm Pool thermocline water temperature anomaly (Dang et al. 2020) (C) $\delta^{18}O$ variability, IODP drill site V21-30

(Koutavas and Joanides, 2011) (D) Concentration of *b. braunii*, El Junco Lake, Galapagos (Zhang et al. 2014) (E) 2-7 year bandpass filter $\delta^{18}O$, Bukit Assam Cave, Borneo speleothem (Chen et al. 2016) (F) (2-7 year bandpass filter $\delta^{18}O$ concentrations from Northern Line Islands corals (Grothe et al. 2020). For continuous proxy records (B-D), r and p values between A and each panel are shown in the top right.

2.4.3 The Role of Volcanism, the ITCZ and Other Ocean Basins in ENSO Variability

While Holocene-scale trends in the Pallcacocha sedimentary record may relate to insolation forcing, robust centennial-decadal scale variability noted by other studies (Cobb et al. 2013, Emile-Geay e al. 2016a) precludes the attribution of ENSO shifts to insolation alone. Several periods in particular show trends that cannot be clearly explained by orbital forcing. The Laguna Pallcacocha record, along with others (Fig. 12), document a decrease in El Niño frequency between 3 and 2 kyr BP, a period which would have experienced enhanced El Niño activity if insolation alone were responsible for forcing long-term changes in the ENSO. The last millennium, a period covered by a multitude of highly-resolved, well-calibrated ENSO proxies remains uncertain and contested (Henke et al. 2017), with changing orbital configurations insufficient to explain the variability apparent in the proxy records. The Laguna Pallcacocha record indicates a higher frequency of El Niño events during the MCA than during the LIA, a pattern repeated by some other proxy records (Hereid et al. 2013). The influence of volcanic aerosol injection, as occurred after the Samalas eruption of the 1250's AD, has been widely investigated and debated (Dee et al. 2020, Stevenson et al. 2016). Recent work has shown that explosive volcanism may induce pronounced multi-decadal Pacific variability, which may in turn modulate the frequency of El Niño events (Mann et al. 2021, Sun et al. 2022).

Changes in the meridional extent of the ITCZ and its relationship to the ENSO, have also been the subject of considerable debate over the Holocene (Asmerom et al. 2020, Haug et al. 2001). The ENSO and the ITCZ are known to be closely related on interannual timescales. Northward displacement of the ITCZ, driven by northern hemisphere warming relative to the Southern Hemisphere, drives strong trade winds at the equator, enhancing upwelling and suppressing the development of El Niño events (Koutavas and Lynch-Steiglitz 2004). Conversely, over the course of the instrumental record, El Niño events are associated with southward ITCZ displacements of up to 5 degrees (Schneider et al. 2014). Insolation is thought to drive latitudinal displacement of the ITCZ on a precessional timescale, with the ITCZ moving further south over the course of the Holocene in response to decreasing boreal summer insolation (Haug et al. 2001). This southward shift has also been invoked to explain a gradual strengthening of the South American Seasonal Monsoon (SASM) over the Holocene (Bird et al. 2011, Kanner et al. 2013). On shorter timescales, several proxies sensitive to Atlantic-derived SASM precipitation activity indicate abrupt drying after about 2 kyr BP (Schittek et al. 2015, Kanner et al. 2013) roughly coincident with an abrupt increase in El Niño events at Laguna Pallcacocha.

Many tropical proxy records from both hemispheres indicate a more northerly ITCZ location during the MCA, consistent with the proposed mechanism of northern hemisphere heating (cooling) driving latitudinal displacement of the ITCZ to the north (south) (Higley et al. 2018). However, there exists continued debate regarding whether this pattern is indicative of simple ITCZ displacement or ITCZ expansion and contraction (Lechleitner et al. 2017). Asmerom et al. (2020) use a highly resolved speleothem record from central Mexico to show that regions at the margins of the ITCZ belt in both hemispheres experience simultaneous drying and wetting during the MCA and LIA, respectively. A wavelet analysis of the speleothem record indicates that the annual

migration of the ITCZ to its modern extent occurs at 1400 CE (550 yr BP) (Asmerom et al. 2020). Four runoff-driven lacustrine reconstructions of the ENSO from the eastern and western tropical Pacific record an abrupt transition from more active to less active ENSO conditions at approximately this time (Rodysill et al. 2018). Crucially, the Lake Lading, Indonesia, sedimentary record records La Niña, rather than El Niño, driven runoff and also indicates greater erosion during the MCA (Rodysill et al. 2018). The Laguna Pallcacocha and Lake Lading records dispute the characterization of the MCA and LIA as defined by persistently El Niño/La Niña like conditions. Instead, it appears the tropical Pacific during the MCA may have been defined by an ENSO system which oscillated on a shorter wavelength than during the LIA. However, discontinuous and lower-resolution proxy records from the last millennium show greater ENSO amplitude during the LIA than during the MCA (Rustic et al. 2015). A comparative absence of external forcing during the MCA may have led to stable conditions in ocean-atmospheric modes such as the ENSO (Bradley et al. 2016). This is reflected by the relatively frequent and consistent clastic depositional events at Laguna Pallcacocha. The tropical Pacific during the LIA may have been defined by stronger decadal and weaker interannual variability during the LIA (Wise et al. 2014, D'Arrigo et al. 2001) which is reflected by relatively less frequent and consistent clastic layers in Laguna Pallcacocha.

A growing body of model (Levine et al. 2017) and proxy (Dominguez-Villar et al. 2017) studies have explored the relationship between the tropical Pacific and Atlantic Multidecadal Oscillation (AMO). Despite the complexities that are apparent in deciphering Pacific-Atlantic interactions, even during the modern era, the revised Pallcacocha record shows compelling similarities with proxy records from the Atlantic region (Fig. 13). Previous paleoclimate studies have found robust, significant correlations between Pallcacocha and proxies from the Atlantic (Dominguez-Villar et al. 2017), linking a speleothem $\delta^{18}O$ record from Kaite Cave, Spain to the

AMO, which in turn influences trade wind strength via the atmospheric bridge (Fig. 13A) (Levine et al. 2017). The temperature of the tropical North Atlantic, also influenced by the AMO has been shown to alter the location of the descending branch of Pacific Walker Circulation. Warming of the Florida Straits (Schmidt et al. 2012) is associated with decreased El Niño related flooding at Laguna Pallcacocha, consistent with a warmer tropical North Atlantic driving increased subsidence in the central and eastern tropical Pacific (Fig. 13B) (McGregor et al. 2014). The apparent reduction in El Niño frequency between 3 and 2 kyr BP occurs coevally with abrupt changes in the Kaite Cave and Florida Strait $\delta^{18}O$ records. While ENSO variability clearly responds to numerous forcing mechanisms, the congruencies linking the tropical Pacific and Atlantic variability warrant further investigation.

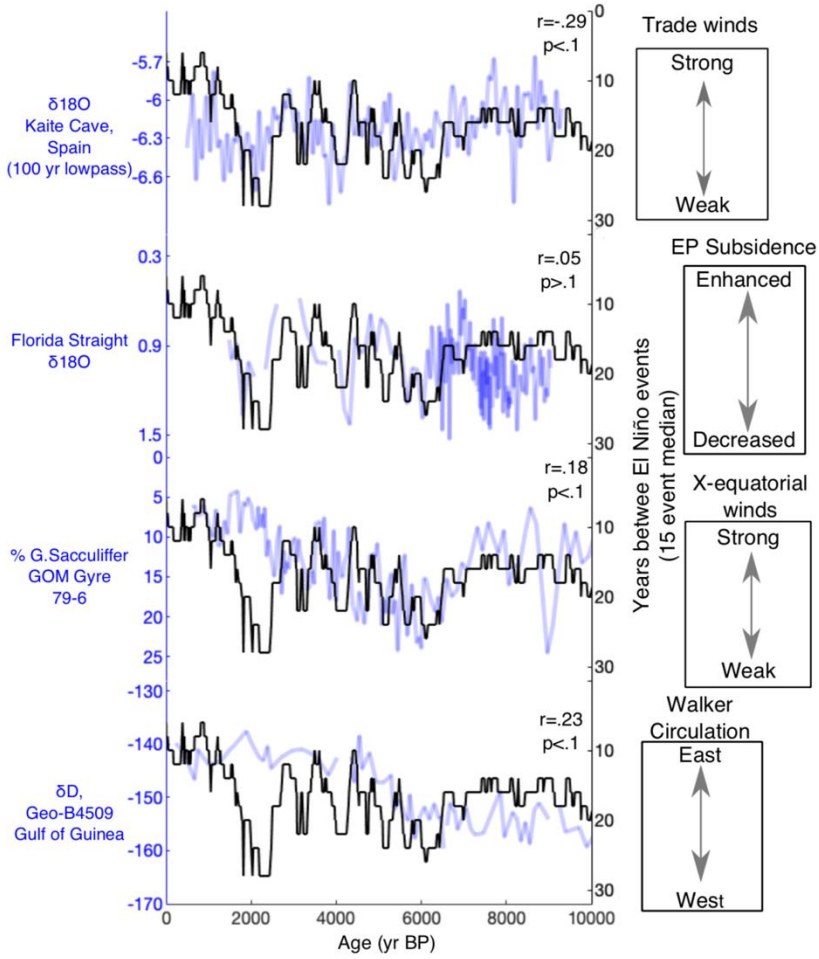

Figure 13. Return interval of El Niño events (15 event rolling median, in black) at Laguna Pallcacocha and various proxy records from the Atlantic basin. Boxes on right indicate proposed interpretation of published proxy, while boxes on left offer potential explanations for how they influence the tropical Pacific. (A) Kaite Cave, Spain speleothem $\delta^{18}O$ record (Dominguez-Villar et al. 2017). Degrees of freedom adjusted to account for lowpass filtering of original record when calculating p value. Potential relationship to ENSO described by Levine et al. 2017 (B) Florida Strait foraminiferal $\delta^{18}O$ record. Relationship to ENSO described by McGregor et al. (2014) (C) % *G. sacculiffer* from Gyre 97-6 PC 20 (Poore et al. 2003). Potential relationship to ENSO described by Hu and Fedorov 2018. (D) West African Monsoon reconstruction using hydrogen isotopes from Gulf of Guinea (Collins et al. 2017). Potential relationship to ENSO described by Pausata et al. (2017).

Proximal records interpreted as being sensitive to centennial scale shifts in the ITCZ (Poore et al. 2003) are consistent with changes in the frequency of flooding at Laguna Pallcacocha (Fig. 13C). Northward shifts of the tropical North Atlantic ITCZ have been shown in modelling studies to increase the strength of cross equatorial winds and induce a La Niña-like mean state in the tropical Pacific (Hu and Fedorov, 2018). Additionally, the strength of the West African Monsoon

and the aridification of the Sahara have been shown to be crucial components in increased El Niño frequency during the late Holocene by shifting Pacific Walker Circulation westward causing La Niña like conditions (Pausata et al. 2017). Increasing El Niño event frequency over the middle and late Holocene occur contemporaneously with a weakening of the West African Monsoon, supporting this mechanism (Fig. 13D) (Collins et al. 2017, Griffiths et al. 2020). The long-term congruencies of records from different ocean basins and the abundance of proposed mechanistic relationships between the Atlantic Ocean and the ENSO suggest the persistence of complex, possibly time-lagged, linkages between Pacific and Atlantic oceanic-atmospheric variability. The development of further well-dated, high-resolution proxy records of ocean-atmospheric variability in the Atlantic will be crucial to improving an understanding of the complex linkages that influence ENSO on multi-decadal timescales. Disentangling Atlantic influence on the tropical Pacific from internally generated variability and externally forced changes will be crucial to anticipating long-term modulation of the ENSO system under different climate regimes.

2.4.4 Spatial Heterogeneity of ENSO events

Increasing attention has been paid to the spatial heterogeneity of ENSO events, or ENSO "flavors" (Ashok et al. 2007). The vast spatial scale associated with the ENSO makes a comprehensive understanding of the entire system from a single proxy archive unreasonable. For example, a recent modelling study has indicated that during El Niño events with warming centered in the central Pacific, Laguna Pallcacocha receives relatively moderate and year-round rainfall. When warming is centered in the eastern tropical Pacific, however, convective activity and precipitation is enhanced (Kiefer and Karamperidou, 2019). This suggests the Laguna Pallcacocha record should be relatively insensitive to central Pacific (CP) El Niño events. Surface sediments

from Laguna Pallcacocha appear to show flood deposits coincident with both eastern Pacific El Niño events and "mixed" El Niño when both EP and CP flavors occur in the same event (Andreoli et al. 2017). This is not surprising given that intense rainfall at Laguna Pallcacocha requires SST warming and convection in the eastern tropical Pacific. Statistically significant relationships exist between the Laguna Pallcacocha flood history and records from both the central and western Pacific (Dang et al. 2020) and eastern Pacific (Koutavas and Joanides 2012) (Fig. 12), indicates there is some degree of coherence between the many flavors of the ENSO over multi-millennial timescales. A newly developed network of coral records (Freund et al. 2019) shows that the ratio of CP to EP events has increased in recent decades, while EP events have become more intense. The development of a continuous Holocene chronology of EP El Niño events will be crucial to testing hypotheses regarding the relationship between different flavors of the ENSO under different background climate conditions.

2.5 Conclusions

The Laguna Pallcacocha sedimentary record has long been cited as a continuous, high-resolution proxy record of El Niño events during the Holocene. Additional age constraints over the past millennium confirmed the link between rapid clastic sedimentation and historically documented El Niño's. Scanning XRF analysis identified flood-driven clastic laminae, which are not captured by previous studies which relied on sediment color analyses, between 11 and 7.5 kyr BP. Clastic laminae deposited during the early Holocene are marked by higher proportions of organic carbon, and were deposited prior to the establishment of the modern páramo which may

have prevented erosion of the unstable upper soil horizon. The revised, erosion-based record of alluvial events at Laguna Pallcacocha more closely matches an emerging consensus of the ENSO over the course of the Holocene: moderate El Niño frequency before 7.5 kyr BP, suppressed El Niño frequency between 7.5 kyr and 4 kyr BP, and more active El Niño conditions after 4 kyr. This pattern is broadly consistent with proposed insolation controls on the ENSO-specifically June and September insolation maxima, which have the effect of warming the western Pacific and accelerating Walker Circulation. However, reduced El Niño frequency between 3 and 2 kyr BP and persistent centennial-scale variability throughout must be explained by other mechanisms. El Niño event frequency peaks during the MCA and relatively fewer events during the subsequent LIA. Proxy records from both sides of the Pacific also suggest more frequent La Niña events during the MCA, suggesting the MCA featured higher frequently oscillations of the ENSO system, rather than persistently El Niño/La Niña like conditions. Consistencies between the Laguna Pallcacocha record and proxy records from the tropical to sub-tropical Atlantic, lacking significant interannual relationships with the ENSO, suggest that previously proposed mechanisms linking the Atlantic and Pacific Oceans have operated over the course of the Holocene, and may explain some of the centennial-scale variability seen in tropical Pacific proxy records. The continuous, high-resolution Laguna Pallcacocha record offers a unique dataset that can be used to test hypotheses regarding ocean-atmosphere dynamics over the Holocene.

3.0 Holocene-scale El Niño frequency and intensity signals preserved in 3 Andean lakes

Long term variations in the El Niño Southern Oscillation (ENSO), along with their drivers, remain poorly understood. The laminated stratigraphy of Laguna Pallcacocha, Ecuador, exhibits inorganic flood deposits driven by intense convective rainstorms which generally occur during eastern Pacific warming associated with El Niño events. Proximal basins, however, show vastly different stratigraphic patterns, despite near identical climatic conditions. We investigate the watershed-scale geomorphology of different basins using a simple erosion model, as well as orthoimagery of land cover, to better understand the factors which influence erosion and deposition in each stratigraphic sequence. By better understanding the geomorphic characteristics responsible for clastic sedimentation and deposition in each watershed, records of flooding events, and correspondingly El Niño events, of different magnitudes can be generated. The flood chronologies of three lakes, (Laguna Pallcacocha, Laguna Martin, Laguna Fondococha) show close correspondence with proxy records from around the tropical Pacific, particularly once accounting for their dominant sensitivity to either ENSO amplitude (the intensity of individual ENSO events) or wavelength (the frequency of oscillations). The Little Ice Age (LIA), we find, shows a generally longer ENSO wavelength but higher amplitude than the preceding Medieval Climate Anomaly (MCA). While amplitude and frequency are largely coupled throughout the Holocene, many proxy records document multiple particularly intense El Niño events during the middle Holocene, occurring during period which has often been interpreted as consistently quiescent in the tropical Pacific. Combining these more refined interpretations demonstrates that many proxy records previously thought to have been contradictory are, in fact, complimentary.

3.1 Introduction

Reconciling divergent proxy evidence of past El Niño Southern Oscillation (ENSO) variability remains a crucial task in understanding how high-frequency climate phenomena evolve over long timescales. Due to the short wavelength of ENSO, its vast spatial scale, and the heterogeneity (or "flavor") of individual ENSO events, geologic archives of paleo-ENSO are rare and often difficult to intercompare. The diverse array of geologic materials which have been used to reconstruct ENSO (Lu et al. 2018) all have different temporal resolutions, uncertainties, and sensitivities to the climate system. Isotopic composition of coral skeletons (Cole et al. 1993, Cobb et al. 2003, Cobb et al. 2013, Grothe et al. 2020) and molluscan assemblages (Carre et al. 2014, McGregor and Gagan 2004) provide sub-annual temporal resolution and, due to their proximity to the core ENSO region, often exhibit high correlations to instrumental records of ENSO. However, chronologies from these sources tend to be discontinuous and coverage is very limited over time periods such as the early Holocene (Tudhope et al. 2001). Foraminiferal assemblages from marine sediment cores are also valuable ENSO archives, continuously spanning long timescales (Rustic et al. 2015, Rustic et al. 2020) but temporal resolution is generally low due to slow marine sedimentation rates. In the terrestrial realm, networks of tree-rings provide exceptional temporal resolution and climatic sensitivity (Li et al. 2013, D'Arrigo et al. 2005) but are obviously located outside the core (oceanic) ENSO region and are thus sensitive to remote (and possibly inconsistent) teleconnections to ENSO itself (Zhu et al. 2022). These archives also rarely extend past the last millennium. Lake sediment reconstructions of ENSO (Conroy et al. 2008, Zhang et al. 2014, Thompson et al. 2017) can offer continuous coverage over long periods, but tend to lack the annual and sub-annual resolution of other ENSO proxy records, and are also drawn from the terrestrial realm.

The unique strengths and weaknesses of each archive type has given rise to statistical techniques designed to highlight the sensitivity of a given proxy to ENSO. For example, bandpass filters (Cobb et al. 2003, Hereid et al. 2013) and sliding windows of moving variance (Jiang et al. 2021) are generally applied to coral aragonite geochemistry time series' to compare the amplitude of ENSO-scale (2-8 year) variability between corals which lived during different times. Due to low marine sedimentation rates, foraminifera-based ENSO reconstructions utilize the intra-sample variance of many individual foraminifera within distinct sediment intervals to reconstruct the amplitude of sea surface temperatures (SST) change over relatively short time periods (Rustic et al. 2015). Each of these proxies are primarily related to ENSO *amplitude* rather than *frequency*. Other proxy types, such as lacustrine biomarker reconstructions (Zhang et al. 2014), sedimentary runoff records (Conroy et al. 2008, Rodysill et al. 2019) and pollen spectra (Barron et al. 2003, Ledru et al. 2013), integrate decadal-scale variability, diminishing individual high-amplitude peaks. These proxies generally constitute valuable archives of changing background conditions, but can rarely resolve individual ENSO events. Varved (Du et al. 2021) or laminated (Mark et al. 2022) sediments can offer a unique perspective in paleo-ENSO reconstructions, in that they provide relatively long-term continuous temporal coverage and are (theoretically) sensitive to changes in the *frequency* of individual El Niño events which span multi-millennial timescales.

The laminated lacustrine sequence of Laguna Pallcacocha, Ecuador represents one of the most widely cited records of Holocene-scale El Niño frequency (Rodbell et al. 1999; Moy et al. 2002; Hagemans et al. 2021; Mark et al. 2022). During El Niño events where warming is centered in the eastern tropical Pacific (EP or COA events), anomalous SST's lead to intense convective activity and extreme rainfall at the study site (Kiefer and Karamperidou, 2019, Hagemans et al. 2021), washing inorganic terrigenous sediment into the lake, where it is deposited and preserved

as millimeter-scale laminae. The Laguna Pallcacocha flood history indicates moderate El Niño frequency during the early Holocene, reduced El Niño frequency during the middle Holocene, and elevated El Niño frequency during the late Holocene, peaking at approximately 1000 BP (Mark et al. 2022). While this Holocene-scale pattern is consistent with other paleoclimate records (Carre et al. 2014, Chen et al. 2016, Zhang et al. 2014, Dang et al. 2020) and owes in part to insolation forcing (Carre et al. 2021), most proxies document centennial-scale variability of the ENSO system which cannot be easily explained by orbital configurations alone (Cobb et al. 2013, Emile-Geay et al. 2016).

Further complicating interpretations of El Niño frequency from the Laguna Pallcacocha flood record, the temporal patterns of flooding events are not repeated in the proximal Laguna Fondococha basin (Schneider et al. 2018). The presence of a flood deposit in a lake basin is the result of a variety of complex and overlapping upstream processes; from the production of loose, allochthonous sediment in the watershed (Schiefer 2006) to the transport of sediments from surrounding hillslopes through fluvial networks (Hooke 2003) to in-lake sediment focusing dynamics which preserves discrete, identifiable flood deposits (Hilton 1985). Given the proximity of the three lakes studied here (Lagunas Pallcacocha, Martin, and Fondococha, Fig. 1), climatic conditions were likely very similar. Hence, differences in the frequency with which flooding events are recorded are driven by unique watershed-scale geomorphology and land cover characteristics. Sediment transport and deposition is a complex function of these upstream and upslope processes; as such, a flood deposit in each lake is indicative of a hydrological maxima of a watershed-specific threshold (Schilleref et al. 2014). While the geomorphic controls on the deposition and preservation of flood events are well documented, few studies have attempted to leverage proximal sedimentary records with different sensitivities to flooding events to resolve

flooding events of different intensities (Schilleref et al. 2016). Here, the frequency of flood deposits in three distinct sedimentary sequences are analyzed through time to better understand the changes in the frequency of El Niño events of different magnitudes throughout the Holocene.

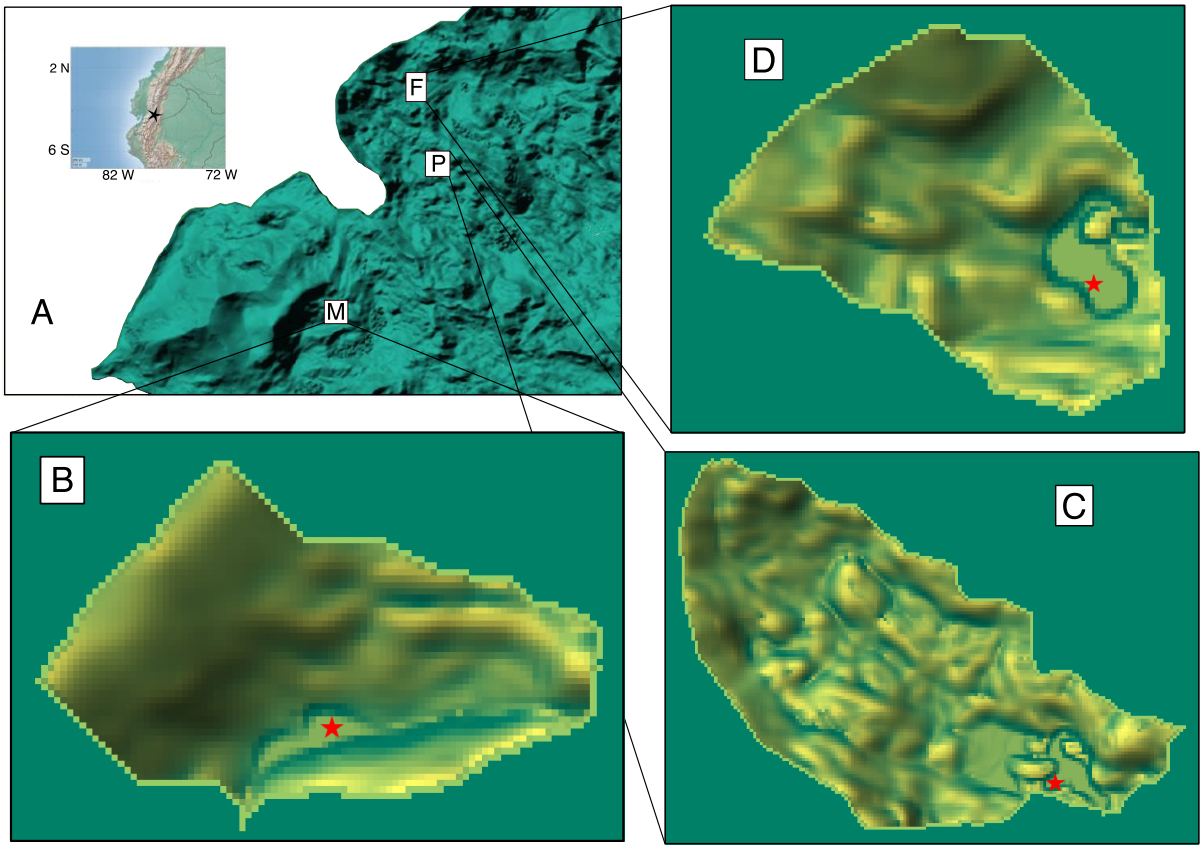

Figure 14. Setting of the three lakes discussed in the text. (A) Study area of Cajas National Park within in Ecuador (inset). Three lakes discussed in this manuscript are denoted by letter in the white boxes (M=Laguna Martin, Panel B, F=Laguna P=Laguna Pallcacocha, Panel C, Laguna Fondococha, Panel D). Red stars indicate approximate location of coring location.

3.2 Methods

3.2.1 Study Area

All three watersheds sit entirely within the boundaries of Cajas National Park, Ecuador. Each lake is above 3800 m.a.s.l and all are within 3 km of one another. The vegetation at each site is dominated by deep-rooted tussock grasses characteristic of high-altitude paramo ecosystems (Hagemans et al. 2019). The underlying bedrock is volcanic ignimbrite of the Tarqui formation (Buytaert et al. 2005). Several volcanic eruptions are documented in many cores from the region, with most deriving from Northern Andes Volcanic Zone, which sits approximately 200 km to the north of the study site (Rodbell et al. 2002, Arcusa et al. 2020). Two earthquakes in the park have been documented since the early 20th century (Hagemans et al. 2023).

3.2.2 Core Collection

Cores used in this investigation were collected from inflatable rubber rafts using Livingstone piston corers in 1993 1999 2017 and 2018. Flocculant surface sediments were collected with an in-tact sediment water interface. At Laguna Pallcacocha and Laguna Martin freeze cores were collected and transported intact back to the University of Pittsburgh.

3.2.3 Orthoimagery and Digital Elevation Models

High resolution orthoimagery obtained from ArcGIS Online (www.arcgis.com) was used to delineate exposed clastic colluvium from vegetation (Neely et al. 2019). Geomorphic analyses

were conducted using the TanDEM-X 11-meter digital elevation models (DEMs) of the region. Some topographic analyses (see section 3.2.4) were calculated on the exposed clastic colluvium rather than the entire watershed. The DEMs were therefore clipped according to the boundaries of the mapped colluvial exposure (delineated by drawing polygons over visible colluvial exposure in ArcGIS) from each watershed to generate clastic specific DEMs for each watershed (Pallcacocha, Martin, and Fondococha). DEMs were processed and analyzed using the TopoToolbox package for MATLAB (Schwangart and Scherler 2014). Slope area plots are utilized to approximate the minimum upstream contributing area needed for channel delineation (Fig. 15). Minimum contributing area was set at 1000 m^2, the approximate concave-convex transition, then adjusted by confirming the presence of visible channels in orthoimages (Fig. 15).

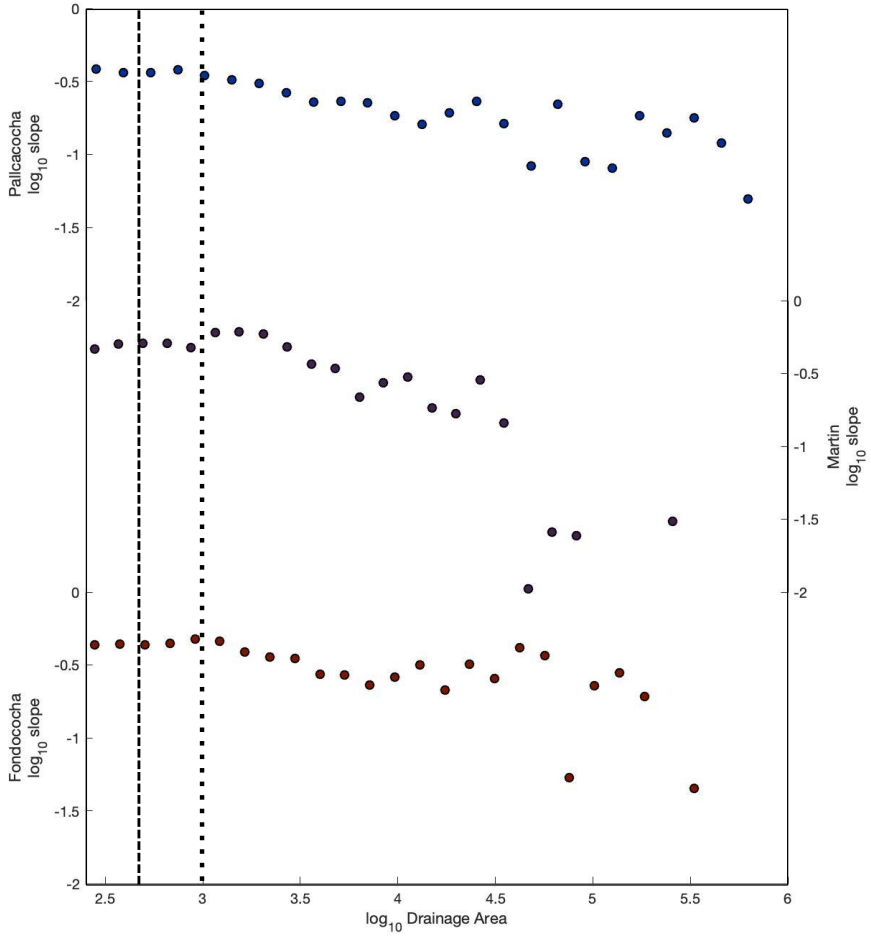

Figure 15. Slope area plots for Lagunas Pallcacocha, Martin, and Fondococha. Datapoints for each site are mean values for 25 evenly spaced bins for each site. Dotted black line represents the minimum threshold (1000 m^2) threshold for channel delineation. Dashed line represents the final minimum area threshold after evaluating resultant channel networks against aerial imagery.

3.2.4 Factor of Safety Calculations

To determine which DEM cells are prone to slope failure, factor of safety (FS) values were calculated for portions of the watershed covered by exposed bedrock (i.e the provenance of the material which constitutes clastic flood deposits in the sediment). FS, or the ratio of stabilizing to driving forces, is computed as:

$$(1)\quad FS=C+\cos(\theta)^{*}\,\theta\,[(1-\min(R/T^{*}a/\sin(\theta),1)r]\,\tan(\phi)/\sin(\theta)$$

(per Chen and Shao 1988). The parameters used in the model were determined from observation and literature values and are defined in Table 1. Values estimated from the literature are taken from sites nearby in the Ecuadorian Andes (i.e Fleischbein et al. 2006, Hagemans et al. 2021 for T and R, respectively), or due to estimations based on general soil types (Hao et al. 2008, Carter and Bentley, 1991). Values for cohesion, effective recharge, and transmissivity were altered according to evaluate the sensitivity of each parameter on the results. While the cohesion value for coarse inorganic colluvium is assumed to be 0.0 N/m^2 (Buchanan and Savigny, 1990), we employ an estimate of 0.1 N/m^2 due to the presence of trace organic soils interspersed with colluvial deposits. However, values of 0.0 N/m^2 are employed as lower bound estimates in our sensitivity tests (Table 1).

Table 1. Parameter, value, and source for each term used in factor of safety (FS) calculations for each watershed. Ranges for C, R, and T are the lower and upper bounds for sensitivity tests. Values in bold represent best estimates used for control runs.

Parameter	Value	Source
Cohesion (C)	0.0-0.3 **(.1)** N/m^2	Buchanan and Savigny, 1990
Effective recharge (R)	0.5-1.0 **(0.7)** cm/hr	Hagemans et al. 2021
Transmissivity (T)	0.1-0.3 **(0.1)** cm/hr	Fleischbein et al. 2006
Soil density (r)	1.33 g/cm^2	Hao et al. 2008
Contributing area (a)	Variable-by cell	DEM-derived
Land surface slope (θ)	Variable-by cell	DEM-derived
Friction angle (ϕ)	35 degrees	Carter and Bentley, 1991

Cohesion (C): Cohesion defines the degree to which a given substrate adheres to itself, given in units of force per unit area (N/m^2). While this term is often divided into soil cohesion and root cohesion, the areas selected for analysis are devoid of vegetation, removing the root cohesion term. Sandy, gravelly soils such as those that comprise the exposed loose ignimbrite headwalls of the basin, are expected to have no soil cohesion either (Buchanan and Savigny 1990), making C 0.

Effective recharge (R): This value represents the approximate rainfall rate for a storm of a given intensity in units of length per time (cm/hr). The Oct 1, 2016 rainstorm which produced a debris flow event at Laguna Pallcacocha, recorded by the nearby Laguna Toreador weather station (Hagemans et al. 2021) is used as the median R value.

Transmissivity (T): Defined here as the rate, in cm/h, at which water passes through the sediment. The transmissivity of the mineral-rich andosol were estimated from Fleishbein et al. 2006, who measured transmissivity values in a similar environment in the Ecuadorian Andes.

Soil density term (r): The loose mineral material covering the area of the watershed analyzed here is weathered from Quaternary silicious ignimbrite and rhyolite bedrock which have both low density and high porosity. Values for density were estimated from Moon (1993).

Upslope area (a) and Slope (θ): These values were derived for each DEM cell from the DEM and calculated using the TopoToolbox package for MATLAB (Schwanghart and Scherler 2014).

Friction angle (ϕ): Friction angle, or the angle at which shear failure occurs, was estimated from literature values for ignimbrite derived soil from Carter and Bentley (1991).

Because FS effectively divides forces which stabilize slopes by those which drive slope failure, values lower than 1 are considered unstable and prone to mass wasting. Values between 1 and 2 are generally at risk of mass wasting, while values above 2 are largely stable.

3.2.5 Stream Power Law Calculations

The stream power law (Whipple 2001) was used to evaluate the capacity of channel networks within each watershed to transport sediment from colluvial source to the lake surface. The stream power law is given as:

$$(2)\quad E = KA^{m}S^{n}$$

Table 2 displays the range of parameters used to calculate E as well as their sources.

Table 2. Parameters, values, and source for the calculation of stream power law (Eq. 2).

Parameter	Value	Source
Erodibility coefficient (K)	2.03^-04-3.36^-07	Whipple 2001
Positive exponent (m)	.45	Whipple 2001
Slope exponent (n)	1	Whipple 2001
Contributing area (m^2)	Varies by grid cell	DEM derived
Slope (S)	Varies by grid cell	DEM derived

Erodibility coefficient (K): This is a dimensionless value which encompasses climatological, lithological, and pedological factors which influence channel erosion and incision. Ranges vary based on values given by Whipple 2001.

Dimensionless constants (m and n): Positive constants which define channel concavity index (m/n).

Upslope area (a) and Slope (θ): These values were derived for each DEM cell from the DEM and calculated using the TopoToolbox package for MATLAB (Schwanghart and Scherler 2014).

3.2.6 Core imagery and X-ray fluorescence

Cores from Laguna Pallcacocha, Martin and Fondococha were imaged and scanned using a Geotek Multi-Sensor core scanner. Micro-XRF scans were conducted at the Large Lakes Observatory at the University of Minnesota Duluth, with an ITRAX XRF core scanner. Scans were conducted at 0.1 cm resolution with a 15 second dwell time.

3.2.7 Statistical analyses

Spectral analysis of annually resolved records were carried out using the multi-taper method in the R package *astrochron* (Meyers et al. 2014). Individual flood layers were determined for each lake according to the methodologies of Mark et al. (2022) which were adapted from Moy et al. (2002).

3.3 Results

3.3.1 Watershed characteristics and channel networks

The watersheds of Lagunas Pallcacocha, Martin, and Fondococha are all defined by relatively high relief (368, 310, and 294 m, respectively) and relatively small areas (1.39, 0.37, and 0.56 km^2 respectively). The Laguna Pallcacocha watershed has the longest channel and greatest drainage area of the three watersheds considered here (Fig. 14, Fig. 16). The intense rainstorm event on October 1, 2016 may have triggered an avulsion in the main channel, possibly redirecting sediment transport from the southern sub-basin of the lake (from which the cores described by Rodbell et al. 1999, Moy et al. 2002, Schneider et al. 2018, and Mark et al. 2022 derive) into the northern sub-basin (Hagemans et al. 2021). At Laguna Martin, clastic delivery into the lake is dominated by a single short channel (Fig. 16), a ~2m deep arroyo which terminates at the northwestern side of the lake (Fig. 17). The primary channel flowing into the Laguna Fondococha watershed is separated from the loose colluvial clastic material by a greater distance

and elevation than at either of the other two sites (Fig. 16), and two separate inflows running off the headwall divide sediment delivery into the lake (Fig. 21, Fig. 18).

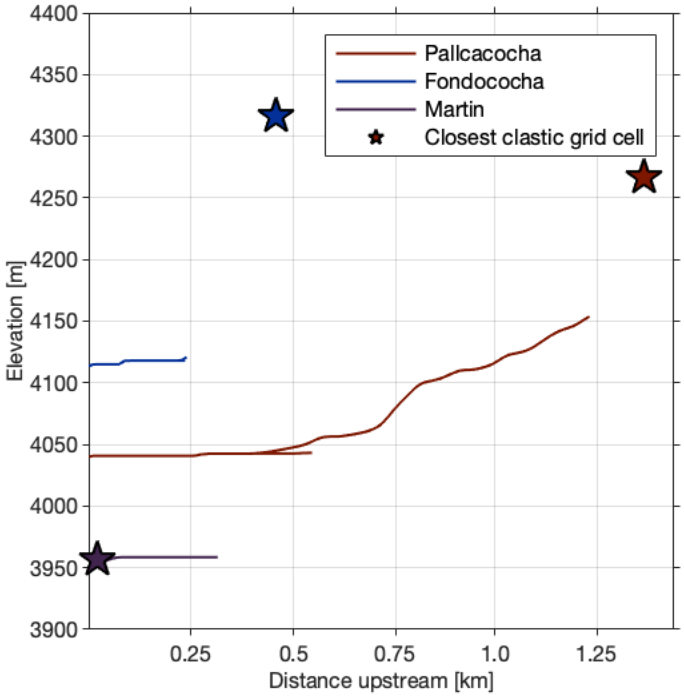

Figure 16. Stream profiles and location of the nearest clastic grid cell for Lagunas Pallcacocha, Fondococha, and Martin.

Figure 17. Large arroyo with buried paleosols in Laguna Martin watershed. Note red pocket knife in circle for scale.

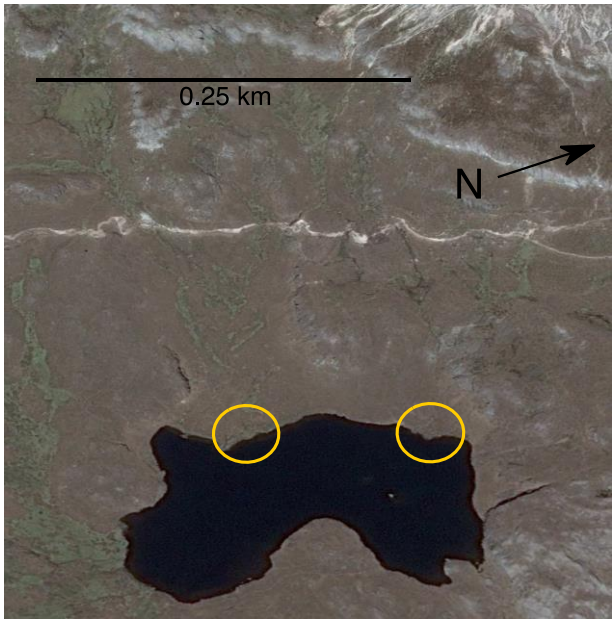

Figure 18. Aerial photograph of Laguna Fondococha watershed. Yellow circles indicate the two inflows where clastic sediment delivery is split.

3.3.2 Factor of safety

Pallcacocha has the lowest mean FS values for DEM cells covered by exposed clastic material (Fig. 19) and Fondococha has the highest. Pallcacocha also has the highest overall amount of exposed clastic grid cells of any of the three watersheds. This indicates loose clastic material commonly experiences slope failure and mobilization at Laguna Pallcacocha, while at Laguna Fondococha, such sediment mobilization is relatively rare. Realistic changes in the cohesion parameter produce the largest effects on overall slope stability, compared to transmissivity and effective recharge (Fig. 19, Fig. 20). This indicates that while the parameters used in calculating FS are generalized estimates, the underlying pattern between sites (that loose sediment production via slope failure is most common at Pallcacocha and least common at Fondococha) is robust.

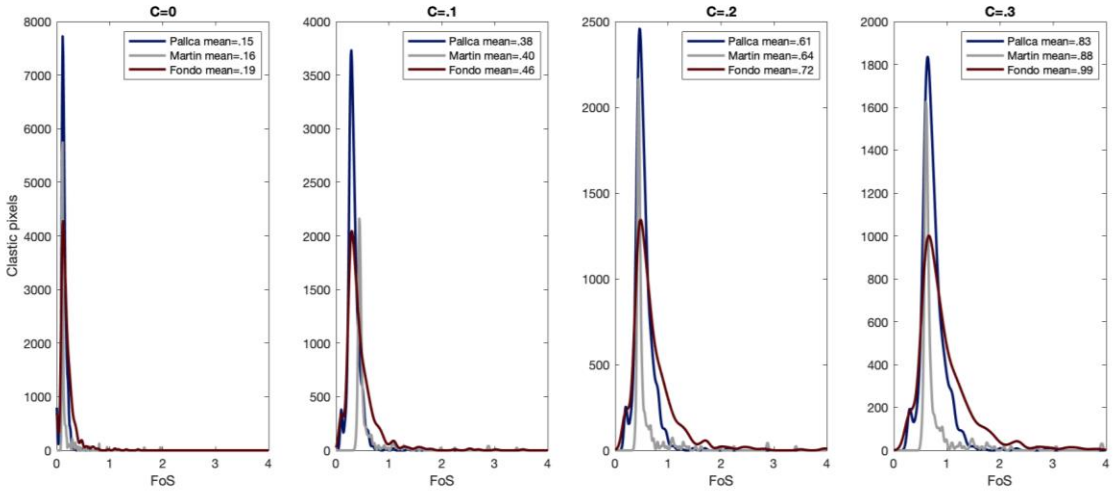

Figure 19. Factor of safety calculations for portions of Laguna Pallcacocha, Laguna Martin, and Laguna Fondococha which are covered by exposed colluvium. Cohesion (C) values were altered, ranging between 0.0 and 0.3 to test sensitivity of results to changes in parameter estimations.

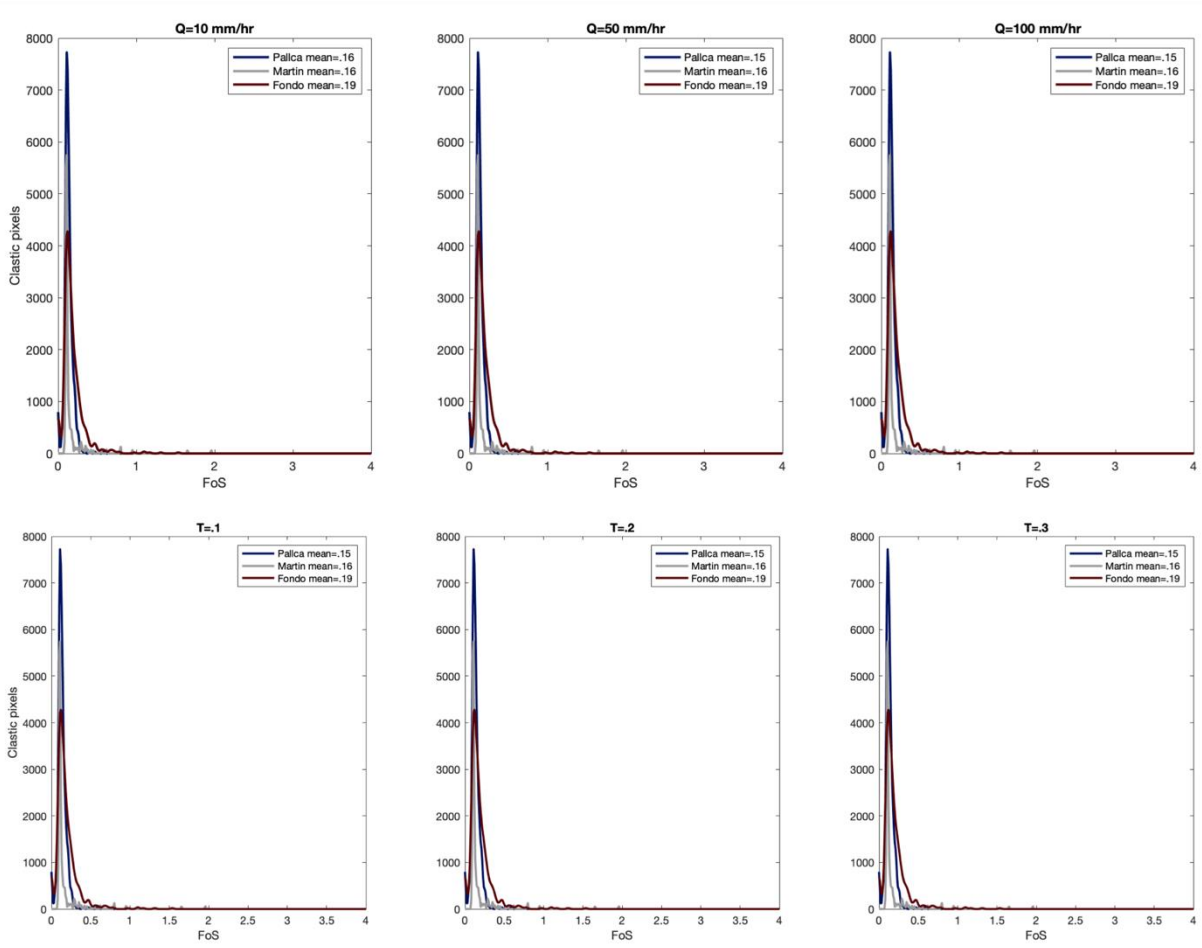

Figure 20. Sensitivity tests for FS calculations. Q values were altered by a factor of 10 (top row) and altering T values by a factor of 3 (bottom row).

3.3.3 Stream power

Channel networks which deliver clastic sediment into the lake basin are apparent in all three watersheds. The highest overall transport capacity for all three lakes occurs upstream of the prograding delta in Laguna Pallcacocha (Fig.21a, red circle). At Laguna Martin, the arroyo which serves as the primary sediment delivery pathway is marked by comparatively elevated values (Fig. 21b, green circle). At Laguna Fondococha, sediment delivery is split between two dominant stream networks (Fig. 21c, yellow circles).

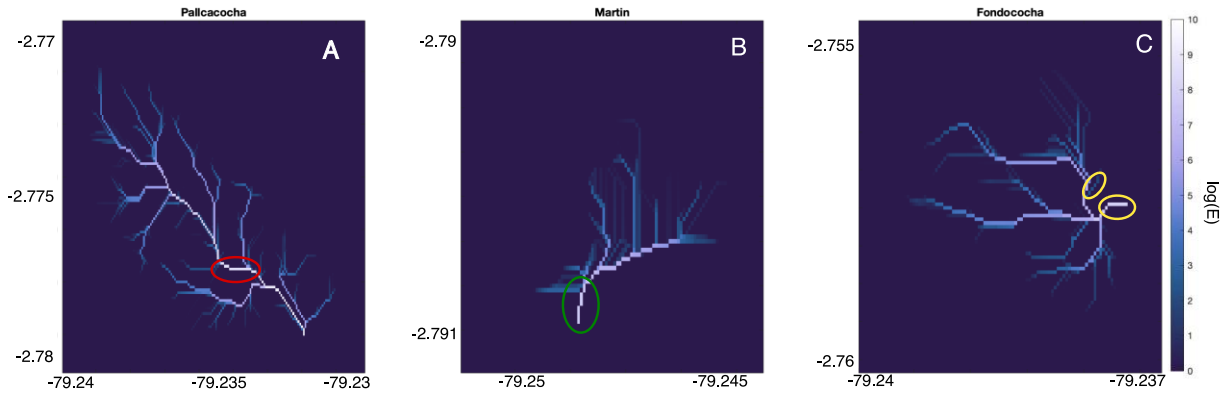

Figure 21. Stream power (E) estimated based on equation 2 for channel networks of Pallcacocha, Martin, and Fondococha. Red circle in (A) represents maximum area of stream power. Green circle in (B) denotes steep arroyo through which sediment is delivered. Yellow circles in (C) represent two distinct inlets which split sediment delivery.

3.3.4 Sedimentological and XRF results

3.3.4.1 Laguna Pallcacocha

While each of the three lakes considered here contain mineral-rich flood deposits generated from hyperpycnal flows, Laguna Pallcacocha contains the greatest number of laminae. It also exhibits the highest sedimentation rate of the three sequences, approximately 50cm/kyr. A transition from glacial clays to Holocene sedimentation is marked in XRF data, magnetic susceptibility, and color at 550cm depth (Fig. 22). The full Holocene sequence has previously been described in detail by Rodbell et al. 1999, Moy et al. 2002, and Mark et al. 2022. Sediments alternate between fine (0.1cm to 2.0cm) light-colored terrigenous laminae interspersed with dark organic-rich layers. Principal component analysis (PCA) indicates that the first principal component (PC1) is highly correlated with Ti, Sr, K, Zn, Al, and Rb, all elements commonly associated with terrigenous sedimentation (Schneider et al. 2018, Mark et al. 2022). Incoherent/coherent scatter (Inc/Coh), a common organic content indicator, is significantly

anticorrelated with PC1 (Fig. 22). PC1 is explains about 80% of the variance in the dataset, and is thus the only principal component investigated here (Fig. 25). The XRF PC1 time series is dominated by extremely high frequency oscillations throughout (Fig. 8).

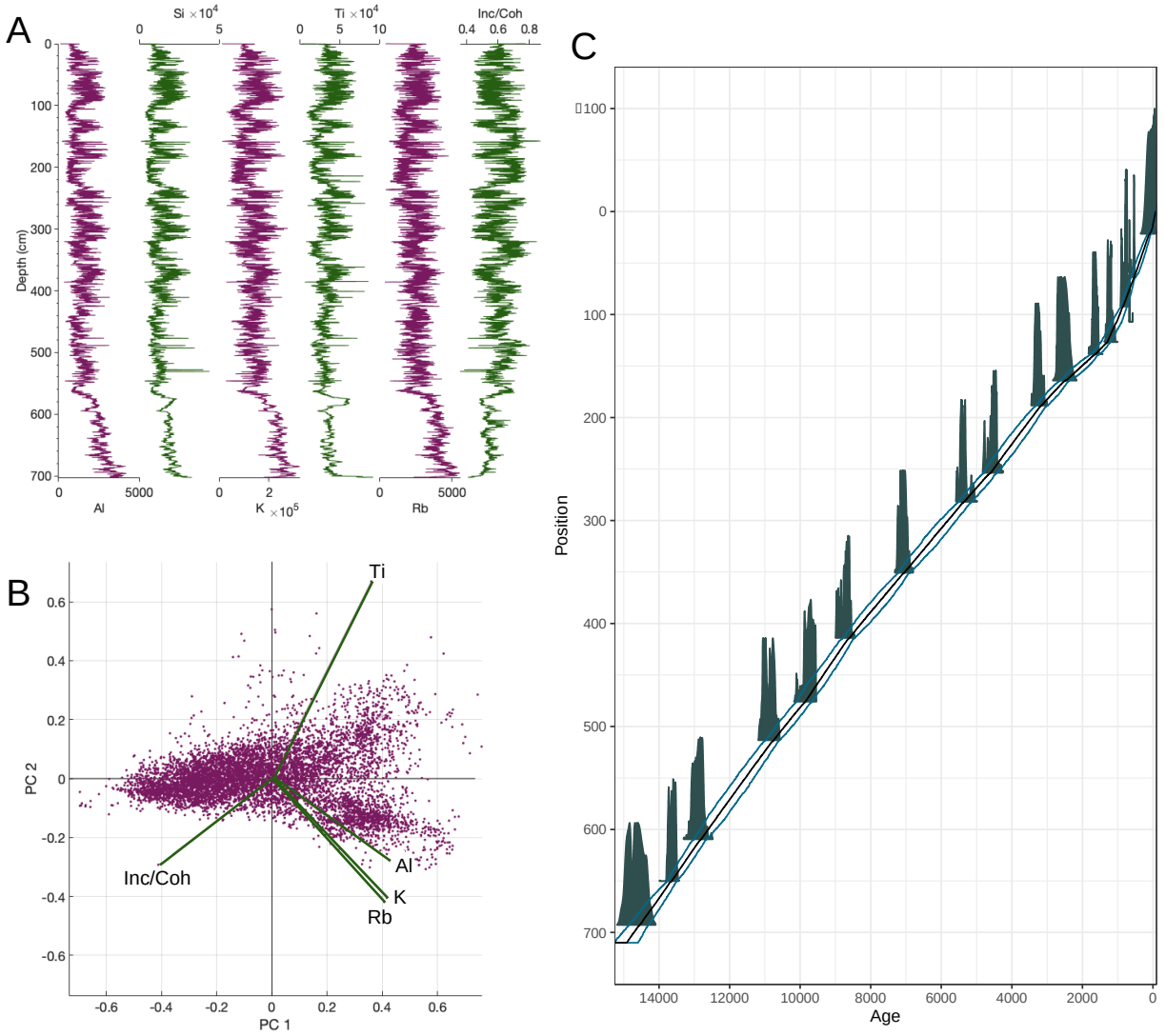

Figure 22. Summary of Laguna Pallcacocha sedimentary record. A) XRF-based elemental composition of full Holocene sequence (B) First 2 principal components of the Laguna Pallcacocha sedimentary record. (C) BChron age model of Laguna Pallcacocha sedimentary record. Probability distributions represent individual chronological control points and blue shading represents the 95% confidence interval.

3.3.4.2 Laguna Martin

The sedimentary record from Laguna Martin spans the years -68-6700 BP (Fig. 23), with a basal unit comprised of extremely course gravel preventing further recovery. The sedimentation rate for Laguna Martin is approximately 38 cm/kyr over the past 4 kyr and approximately 50 cm/kyr from 4 kyr to the base of the core (Fig. 23C). Clastic layers in the Laguna Martin sequence are consistent with the rapidly deposited fining-upwards laminae described in detail by Rodbell et al. (1999) and Schneider et al. (2018), but are generally thicker (0.5-2.0cm) than those found in the Laguna Pallcacocha sedimentary record. PCA reveals the first principal component of the Laguna Martin XRF dataset is very similar to that of Laguna Pallcacocha (Fig. 22B, Fig. 23B). PC1 explains almost 90% of the overall variance, and is thus the only principal component discussed (Fig. 25). The full XRF PC1 time series shows short-lived pulses of clastic sediment delivery marked by brief spikes in PC1 (Fig. 26). More frequent peaks are apparent at the beginning of the record and over the past 500 years (Fig. 26).

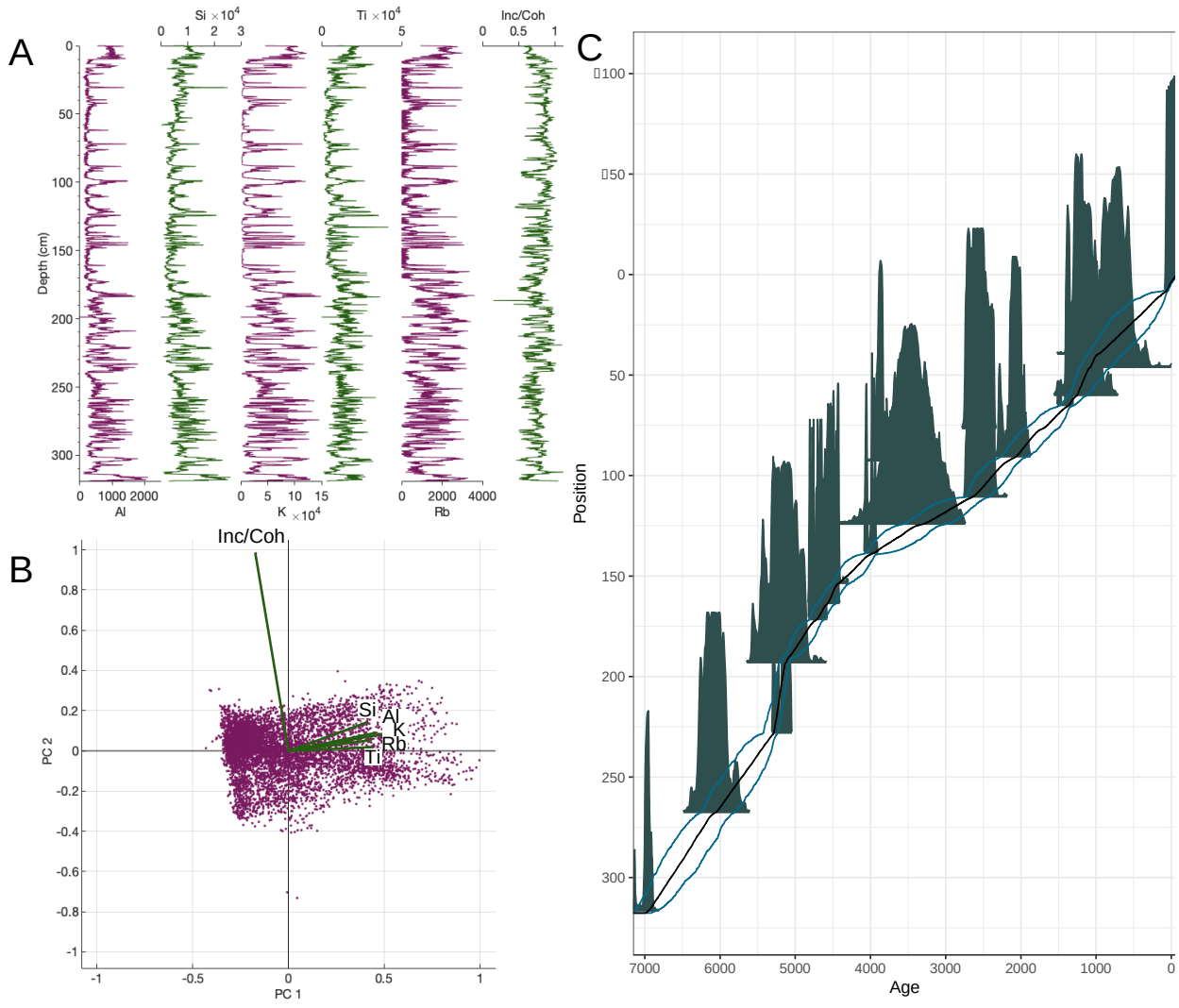

Figure 23. Summary of Laguna Martin sedimentary record. (A) XRF-based elemental composition of the full ~7000 year sequence (B) First 2 principal components of the Laguna Martin sedimentary record. (C) BChron age model of Laguna Martin sedimentary record. Probability distributions represent individual chronological control points and blue shading represents the 95% confidence interval.

3.3.4.3 Laguna Fondococa

The Laguna Fondococha sedimentary sequence covers the period -68-13000 yr BP (Fig. 24). A transition from glacial clays to more organic rich and laminated Holocene sediments is apparent at 514 cm. XRF PC1 in the Laguna Fondococha record is similar but opposite in sign to XRF PC1 in Martin and Pallcacocha (i.e negative PC1 excursions in Fondococha PC1 are rich in

Ti, Sr, K, Zn, Al, and Rb while positive excursions are defined by high Inc/Coh scatter, Fig. 24B). Like Pallcacocha and Martin, the first principal component explains about 80% of the overall variance and is discussed exclusively (Fig. 25). The difference in sign might reflect the comparatively low mineral input in the Laguna Fondococha sequence. Laminations in Laguna Fondococha are less frequent and less visually apparent. Some discrete negative excursions in XRF PC1 are visibly identifiable, but are markedly less prominent than in Pallcacocha or Martin (Fig. 26).

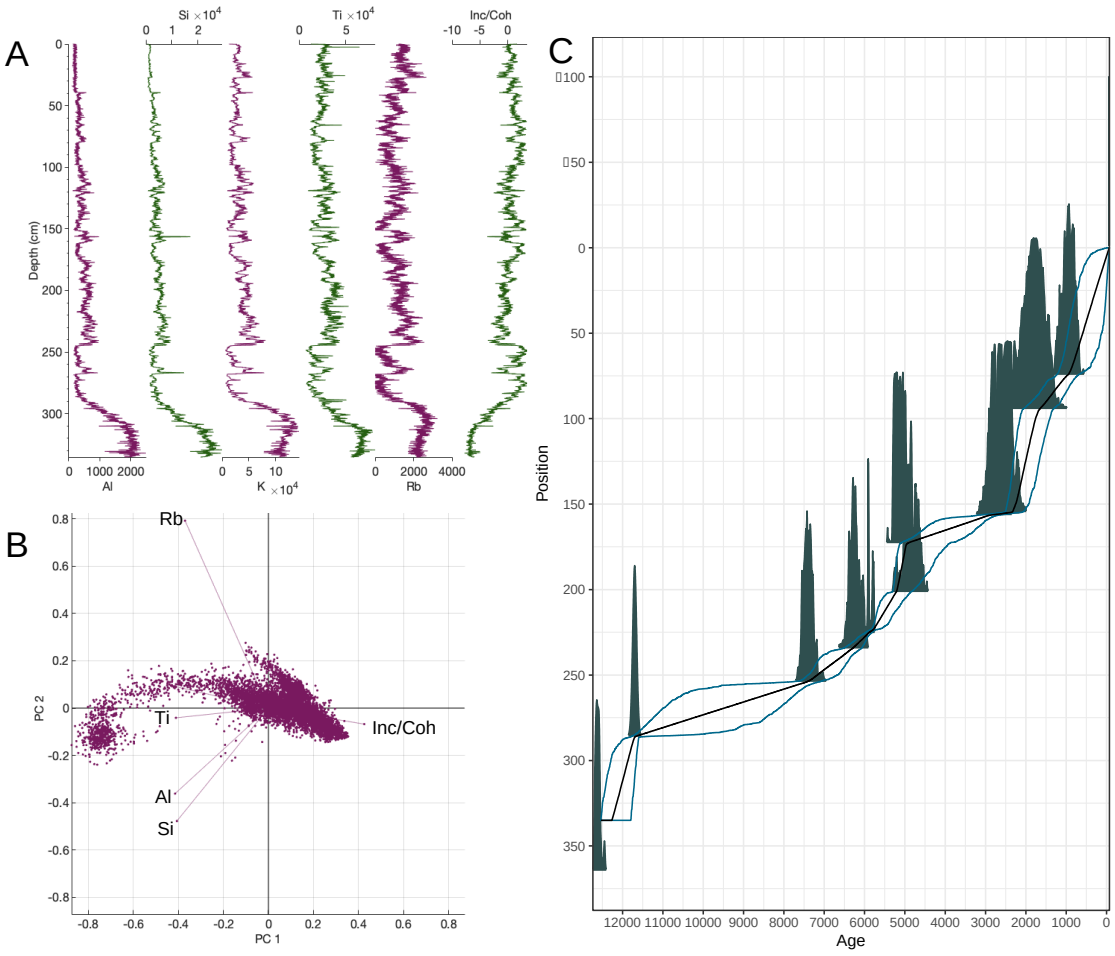

Figure 24. Summary of Laguna Fondococha sedimentary record. (A) XRF-based elemental composition of full Holocene sequence (B) First 2 principal components of the Laguna Fondococha sedimentary record. (C) BChron age model of Laguna Fondococha sedimentary record. Probability distributions represent individual chronological control points and blue shading represents the 95% confidence interval.

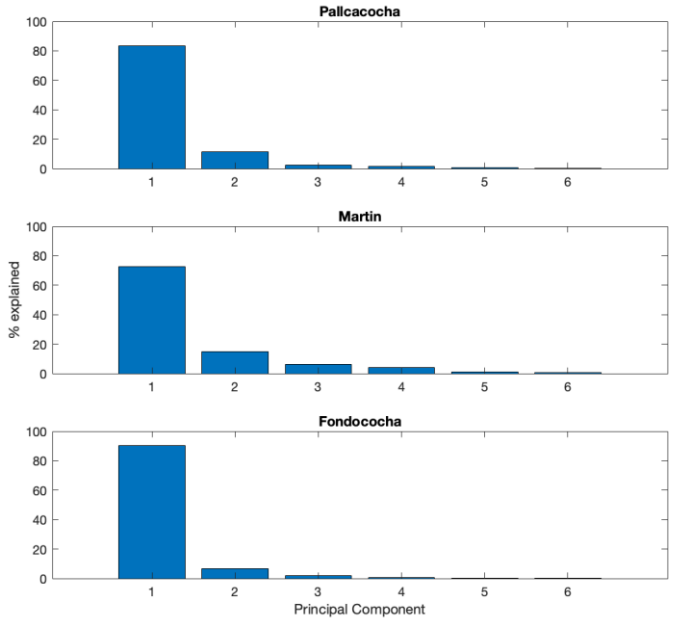

Figure 25. Percent of overall variance in XRF dataset explained by each principal component for each of three lakes.

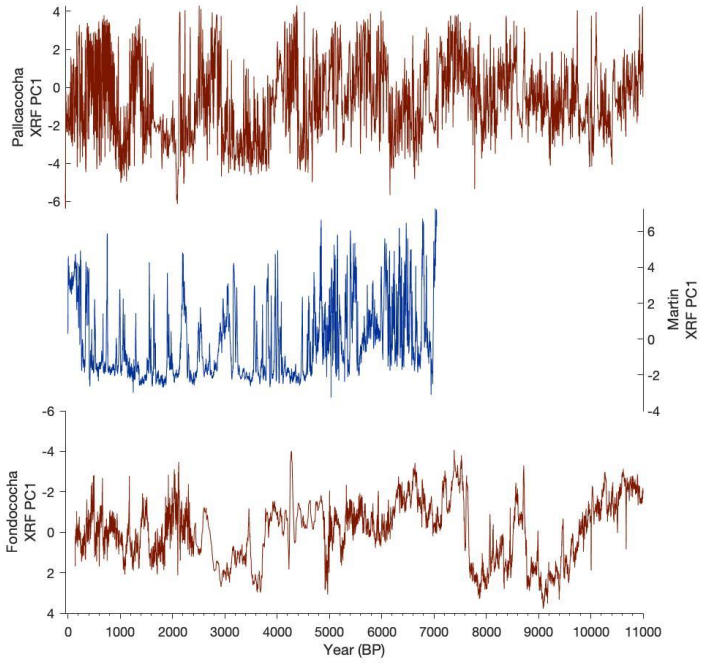

Figure 26. First principal component (PC1) for XRF data from Lagunas Pallcacocha (top panel) Martin (middle panel) and Fondococha (bottom panel).

3.4 Discussion

3.4.1 Interpretation of differing clastic stratigraphies in proximal lakes

The unique geomorphic setting of each watershed dictates its sensitivity to high-intensity precipitation events. Clastic alluviation is a function of both the production of loose clastic sediment (estimated from FS calculations, as an means of evaluating the likelihood of slope failure) and the transport of sediment (estimated from stream profiles and stream power law analyses). The Laguna Pallcacocha watershed has the lowest overall mean FS value, as well as the greatest overall amount of exposed clastic material (Fig. 20), which contributes to abundant clastic sediment production. The channel which delivers clastic sediment into the lake is the longest of the three considered here, and has the most powerful stream network (Fig. 16, Fig. 21). This combination of factors makes the Laguna Pallcacocha record relatively sensitive to flooding, as abundant loose material can be transported down a relatively high drainage-area channel.

At Laguna Martin, a comparatively low proportion of the watershed is covered by clastic DEM cells. However, these clastic DEM cells are both comparatively close to the lake (Fig. 16) and are generally very unstable (Fig. 20), with a deep arroyo transporting terrestrial sediment into the lake. Mean FS values suggest that the watershed is less prone to slope failure than Laguna Pallcaocha, but more prone than the Laguna Fondococha watershed (Fig. 20). Given the steep slope of the channel, and the proximity to the lake, it is unlikely that sediment delivery to the lake is limited by transport during high-intensity precipitation maxima. This is further supported by the large clast size of some alluvial deposits, indicating that high energy flows which can entrain large particles are mobilized during intense floods. Additionally, the lake area is small in relation

to Pallcacocha and Fondococha, and thus a comparatively small amount of clastic sediment must be transported a comparatively short distance for a clastic deposit to form.

At Laguna Fondococha, both clastic sediment production and transport are likely limiting factors for the generation of a flood deposit. Laguna Fondococha has the greatest proportion of stable FS values (Fig. 20). The channel which transports sediment into the lake is relatively distal from the clastic source compared to Laguna Martin (Fig. 16) and has a channel network of modest power compared to Laguna Pallcacocha (Fig. 4). Perhaps most importantly, two separate channels connect the clastic headwall to the lake, splitting sediment delivery between two discrete inputs (Fig. 21, Fig. 18). This hinders the formation of clastic deposits (Schillereff 2014). Only particularly intense hydrological maxima, then, produce alluvial deposits in Laguna Fondococha.

Laguna Pallcacocha, sitting within a watershed whose topographic characteristics are conducive to the production and transport of clastic material, preserves a record of El Niño frequency. This is supported by the similarity between the number of flood deposits in Laguna Pallcacocha and the simulated frequency of eastern Pacific/Coastal (EP/COA) ENSO events (Fig. 27, Karamperidou and DeNizio 2022). EP/COA events where warming is pronounced in the eastern tropical Pacific drive upwelling and intense convective storms at Laguna Pallcacocha (Kiefer and Karamperidou 2019, Hagemans et al. 2021), and are thus the most appropriate ENSO signal to compare to the Laguna Pallcacocha flood stratigraphy. The number of flood deposits per 100 years in the early Holocene (9 kyr BP) simulation is substantially lower than the number of simulated EP/COA events (Fig. 27). This can be explained by a simulated weakening of the influence of EP/COA events on precipitation in western South America, which could have failed to have produced hydrological maxima sufficient to be recorded, even in Laguna Pallcacocha (Karamperidou and DeNizio 2022).

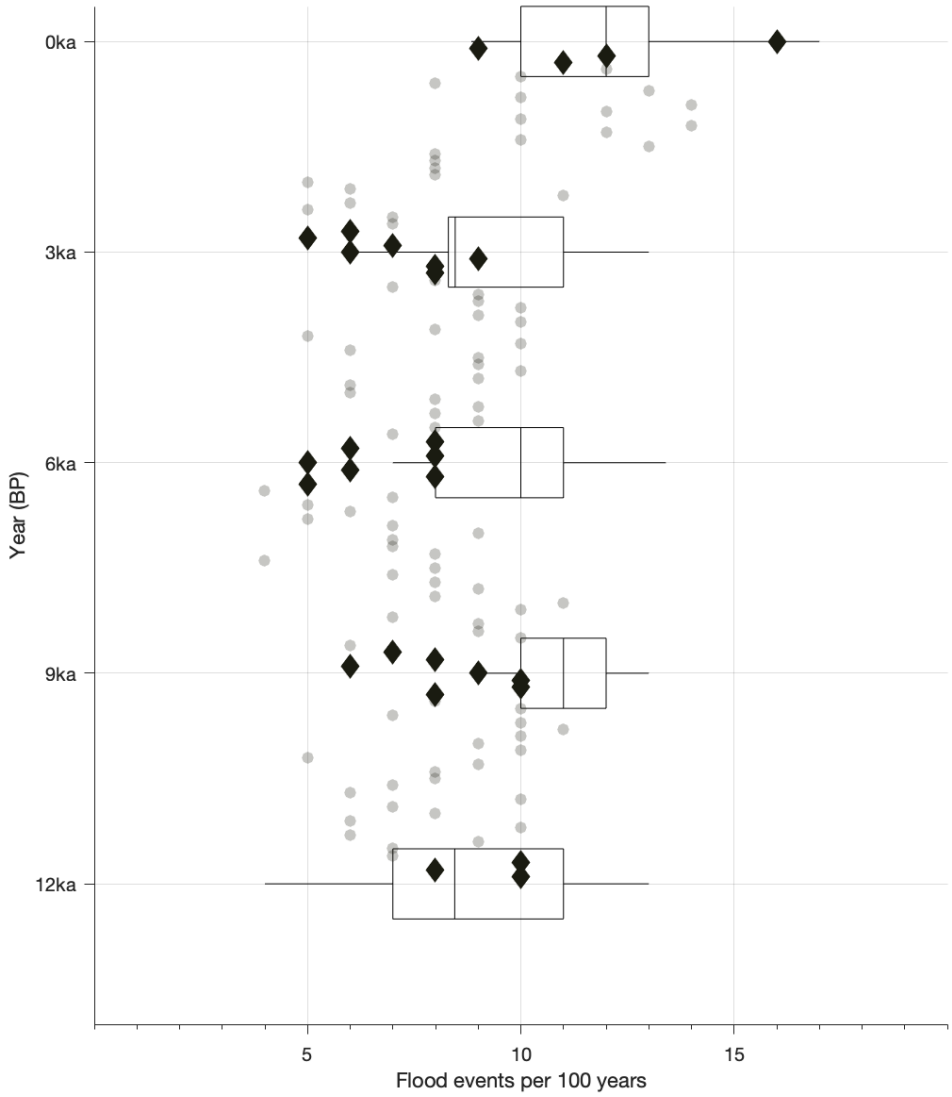

Figure 27. Number of flood deposits per 100 years recorded by Laguna Pallcacocha XRF PC1 (gray dots and black diamonds) and simulated number of EP/COA El Niño events per century (box plots, Karamperidou and DeNezio 2022). Black diamonds indicate values for centuries' which overlap with the temporal period of the model run while gray dots indicate centuries which fall between them. Boxplots indicate interquartile range (IQR) of each simulation calculated on random 100-year samples. Black lines show median and whiskers show 1.5 times the IQR.

The geomorphic characteristics of the Martin and Fondococha watersheds may prevent moderate flood events from producing measurable deposits in the sedimentary record. Hence,

only extremely powerful flood events are discerned in these sequences making them archives of El Niño intensity (as opposed to frequency). More specifically, a flood deposit in these lakes can be interpreted as a particularly extreme EP/COA El Niño events. This interpretive framework can be used to better understand shifts in both the wavelength and amplitude of the ENSO signal over the Holocene.

A possible complicating factor for interpreting the stratigraphy of the three lake (particularly Lagunas Martin and Fondococha, where clastic deposit are relatively infrequent) are the occurrence of earthquakes, which can create shallow landslides and overcome sediment supply limitations even in the absence of intense rainfall events. This seems unlikely as a primary driver of sedimentation for several reasons. For one, neither of the two earthquakes documented during the 20th century (1938 and 1948) are obviously associated with sedimentation in Laguna Martin or Fondococha (NOAA, 2020). Second, the Laguna Pallcacocha stratigraphy records a single obvious deformational structure over the Holocene, occurring at approximately 2500 BP, and such a feature is not obvious in either the Laguna Martin or Fondococha records. This suggests that while some degree of seismic activity is common in the region, it may not be sufficient to mobilize abundant clastic sediment and alter the stratigraphy of the cores. Finally, while earthquakes would increase the amount of loose clastic sediment available to be mobilized, this would not change the transport limitations inherent in the Laguna Martin and Fondococha watersheds. While there may be some minor contribution of seismic activity to the clastic stratigraphy of lakes in Cajas National Park, most of the alluvial signal in Laguna Martin and Fondococha should be attributed to repeated intense flooding events.

3.4.2 El Niño frequency and intensity during the last millennium

ENSO variability over the last millennium remains an open question, despite several synthesis efforts which have sought to utilize the comparatively high number of relevant proxy reconstructions from the relatively recent past (Henke et al. 2017, Emile-Geay et al. 2013). While some individual records indicate enhanced El Niño activity during the Medieval Climate Anomaly (MCA: 950-1250 CE) compared to the Little Ice Age (LIA: 1450-1850 CE, Masson-Delmotte et al. 2013) (Hereid et al. 2013), more frequent El Niño events (Thompson et al. 2017, Mark et al. 2022) or overall more "El Niño-like" conditions (Mann et al. 2009, Yan et al. 2011), many others indicate the opposite (Rustic et al. 2015, Cobb et al. 2003, Li et al. 2011). Spectral analyses of a 1200-year tree-ring based ENSO reconstruction (Li et al. 2011) and the annually laminated Santa Barbara Basin record (Du et al. 2021), and the return interval of flood events preserved in Laguna Pallcacocha, all of which are sensitive to El Niño event frequency, show generally shorter wavelengths during the MCA compared to the LIA (Fig. 28). At Laguna Fondococha and Laguna Martin, however, more frequent events occur during the LIA (Fig. 29). Individual foraminiferal analysis, which resolves only the most intense events, documents a shift towards more very-strong El Niño's occurring at approximately the middle of the millennium (Rustic et al. 2015, Fig. 29). This is consistent with well-dated coral reconstructions, also suggest greater ENSO amplitude during the LIA (Cobb et al. 2003). Crucially, a lacustrine runoff record from the western tropical Pacific also indicates more frequent La Niña (rather than El Niño) driven flooding during the MCA (Rodysill et al. 2019). This suggests that the MCA was defined by higher-frequency oscillations of the ENSO system rather than necessarily more El Niño or more La Niña like mean states. The LIA, conversely, was marked by an attenuation of ENSO periodicity, but was prone to extraordinarily strong events.

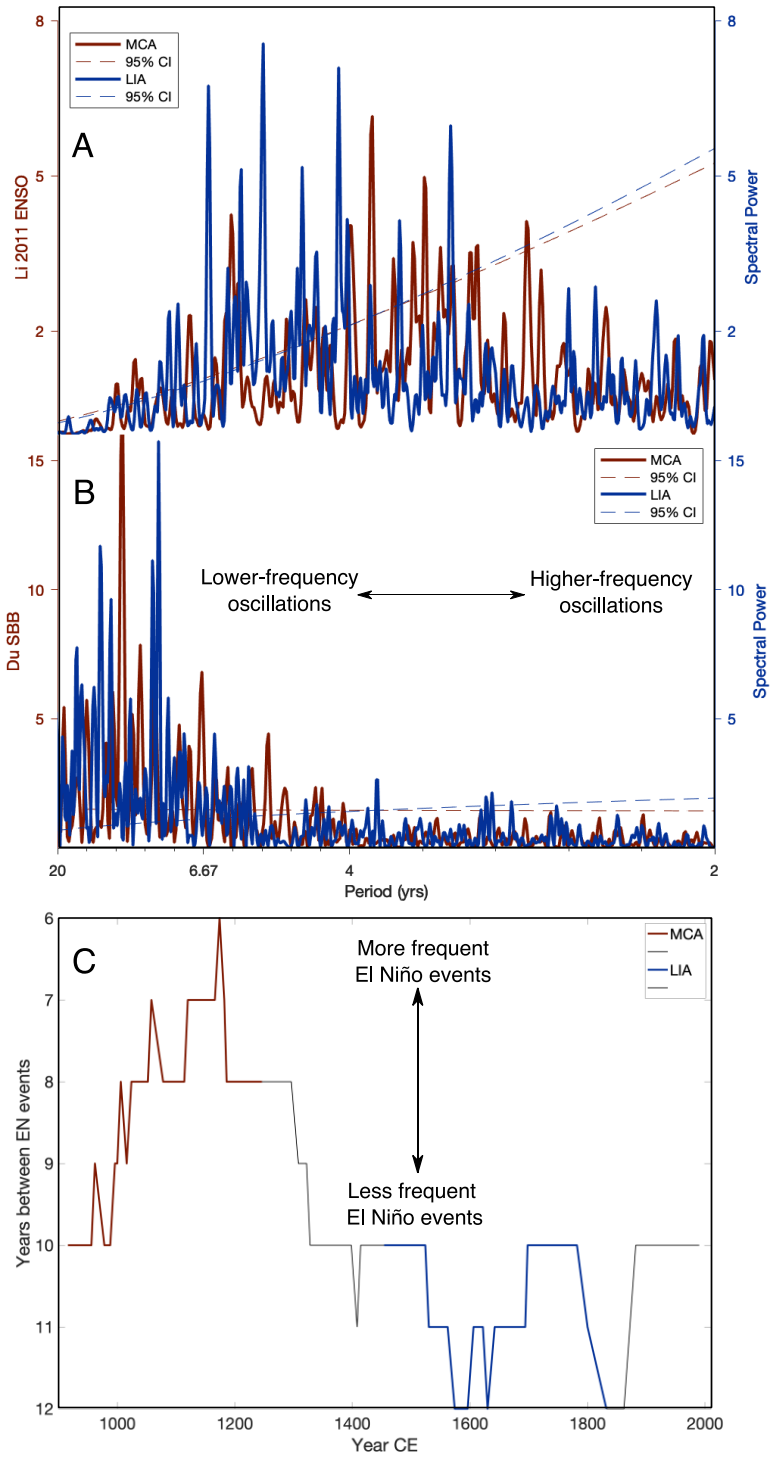

Figure 28. Finely resolved proxies for ENSO frequency over the last millennium. (A) Multi-taper method (MTM) periodogram of tree-ring based ENSO reconstruction (Li et. al 2011) and (B) MTM periodogram of the Santa Barbara Basin varve record (Du et al. 2021) during the MCA (red) and LIA (blue). (C) Years between flood events recorded by Laguna Pallcacocha (5 event moving median, Mark et al. 2022) with MCA highlighted in red and LIA highlighted in blue.

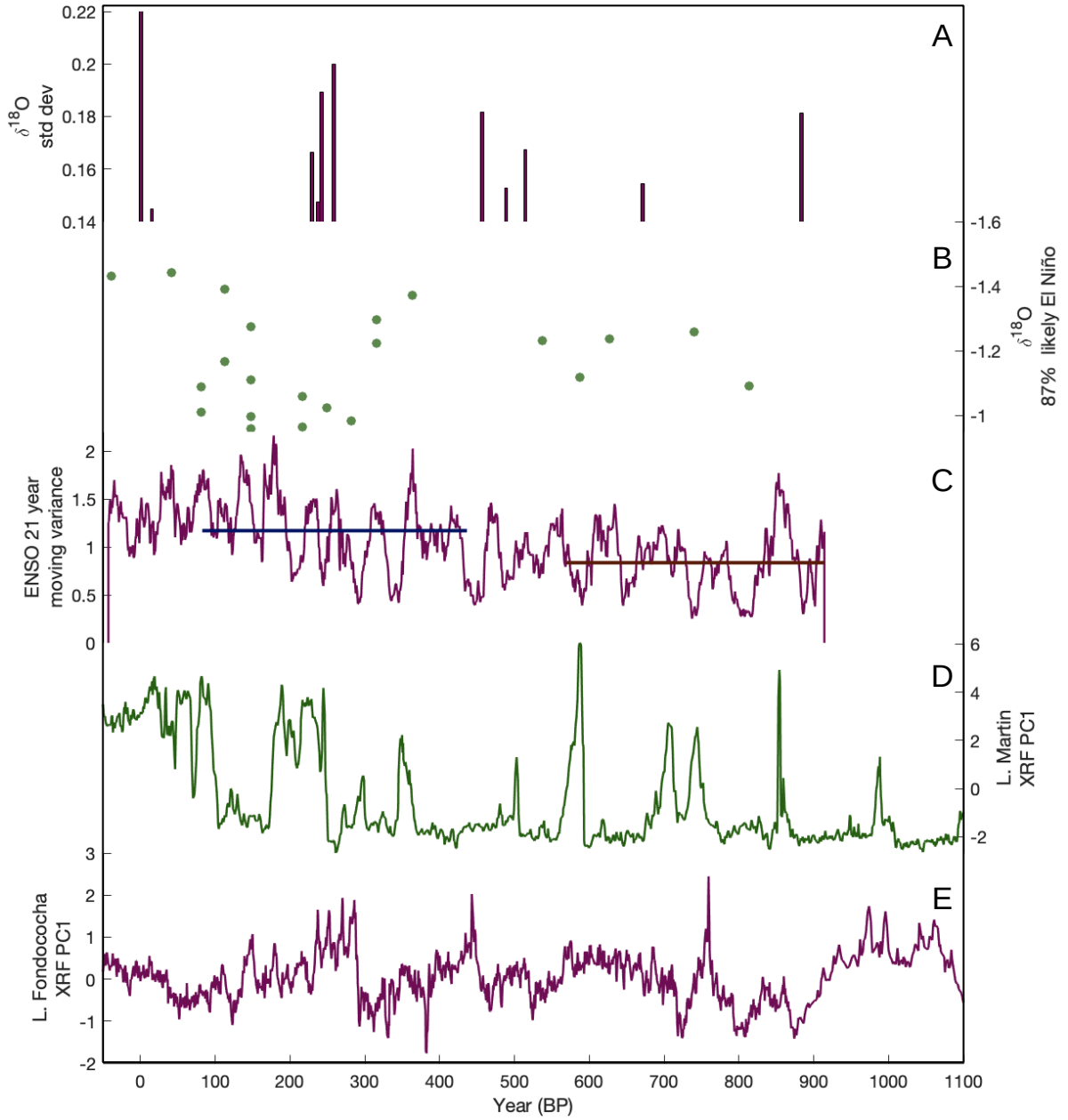

Figure 29. ENSO proxies over the last millennium which are sensitive to the amplitude of ENSO/El Niño events. (A) 2-7 year standard deviation of bandpassed oxygen isotope data from Palmyra atoll corals (Cobb et al. 2003). (B) Mean-removed $\delta^{18}O$ values of *G. Ruber* from the eastern tropical Pacific. Datapoints represent individuals which have an 87% chance of representing El Niño conditions (Rustic et al. 2015). (C) 21-year moving variances of ENSO-sensitive western North America tree-ring records (Red and blue horizontal lines represent mean values for MCA and LIA, respectively) (Li et al. 2011). (D) Peaks in XRF PC1 records from Laguna Martin and (E) Fondococha (this study) are interpreted as indicating particularly strong El Niño events. Blue box represents the LIA and red box represents the MCA.

3.4.3 El Niño Frequency and Intensity during the Holocene

The Laguna Pallcacocha flood record indicates infrequent El Niño's between 7-5 kyr BP (Fig. 30). This is consistent with thermocline temperature reconstructions from the Indo-Pacific Warm Pool which suggest stronger Walker Circulation during this period, which would have inhibited the formation of El Niño events (Dang et al 2020, Fig. 30). Varved sediments from the Santa Barbara Basin (SBB) sensitive to El Niño-driven runoff also indicate a reduction of El Niño frequency between 7-5 kyr BP (Du et al. 2021). El Niño-driven algal blooms from the same site were also less prominent during this time (Nederbragt et al. 2005). A fossil coral reconstruction from Kiritimati dated to approximately 4.3 kyr BP shows an attenuation of ENSO wavelength, with significant periodicities aragonite $\delta^{18}O$ composition of greater than 6 years. This is a substantial attenuation of ENSO wavelength compared to modern coral and SST reconstructions, which show maximum spectral power at wavelengths of less than 5 years (McGregor et al. 2013, Fig. 30). The warm-water sensitive mollusk species *Mesodesma donacium* and *Choromytilus chorus* are present in archaeological middens in coastal Peru between 5.8-2.8 kyr BP, but not afterwards, which indicates an increase in the frequency of lethal marine heatwaves associated with EP/COA El Niño events.

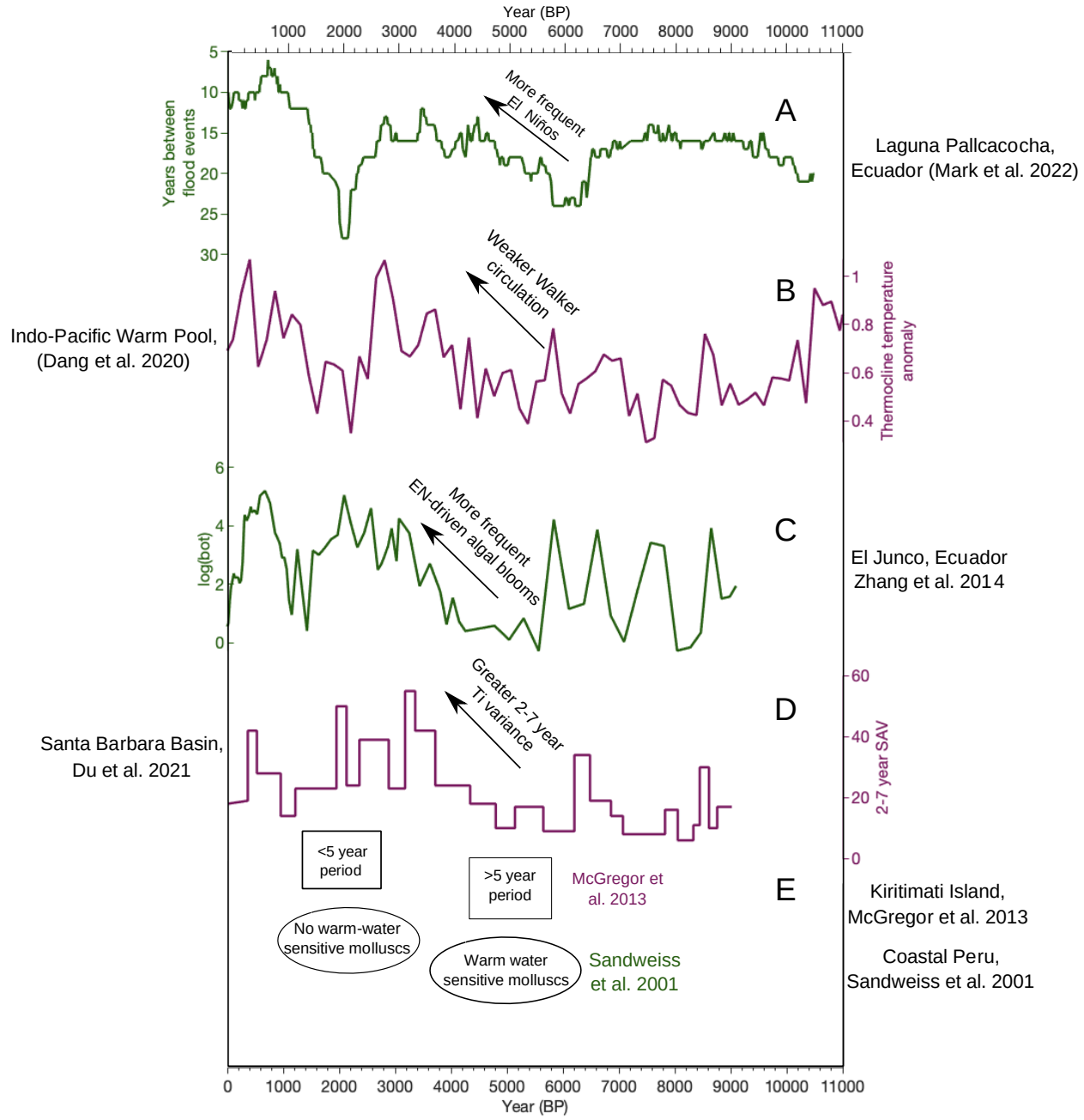

Figure 30. Holocene-scale proxies for ENSO group by their dominant sensitivity to ENSO frequency. (A) Years between successive El Niño-driven flood events at Laguna Pallcacocha, Ecuador (Mark et al. 2022, this study) (B) Indo-Pacific warm pool temperature anomaly (Dang et al. 2020) (C) log of *b. braunii* concentration, indicative of El Niño frequency, at El Junco Lake, Galapagos (Zhang et al. 2014) (D) El Niño-driven algal blooms in the Santa Barbara Basin (Nederbragt et al. 1995), dominant pollen contributions from ODP site 1019, Northern California (Barron et al. 2003). (E) Spectral analysis of *Porites* corals from approximately 4.3 kyr BP indicate longer ENSO wavelength (>5 year period) vs. modern corals from the same location (McGregor et al. 2014) and molluscan assemblages from coastal Peru which indicate an abrupt absence of warm-water sensitive molluscs after 4.3 kyr BP, indicative of more frequent El Niños.

In contrast to El Niño frequency records, El Niño intensity reconstructions from Laguna Martin and Laguna Fondococha both show periods of elevated flood frequency between 5-6 kyr BP (Fig. 31). Periods of elevated ENSO amplitude during the middle Holocene have been noted by other proxy records as well; individual foraminifera from an eastern Pacific marine sediment core (Koutavas and Joanides, 2012) shows enhanced $\delta^{18}O$ variance between 6-7 kyr BP compared to between 3-6 kyr BP (Fig. 31). In the Central Pacific, too, corals record greater ENSO amplitude between 5-7 kyr BP than between 3-5 kyr BP (Grothe et al. 2020) (Fig. 31). In the Indo-Pacific warm pool, discrete windows of hydroclimate variability captured by a speleothem from Bukit Assam Cave, Borneo show lower ENSO-scale amplitude between 3.5-5.5 kyr BP than between 6.5-6.7 kyr BP (Fig. 31, Chen et al. 2016). A synthesis of tropical Pacific coral and molluscan assemblages suggest the period between 3-5 kyr BP was marked by a 64% reduction in ENSO amplitude (Emile-Geay et al. 2016). While these records reflect a variety of different spatial configurations of ENSO, there appears to be approximate coherence between eastern and central tropical Pacific records. In all, greater attention to the unique climatic sensitivities of individual proxy records can resolve many lingering discrepancies in the paleo-ENSO literature.

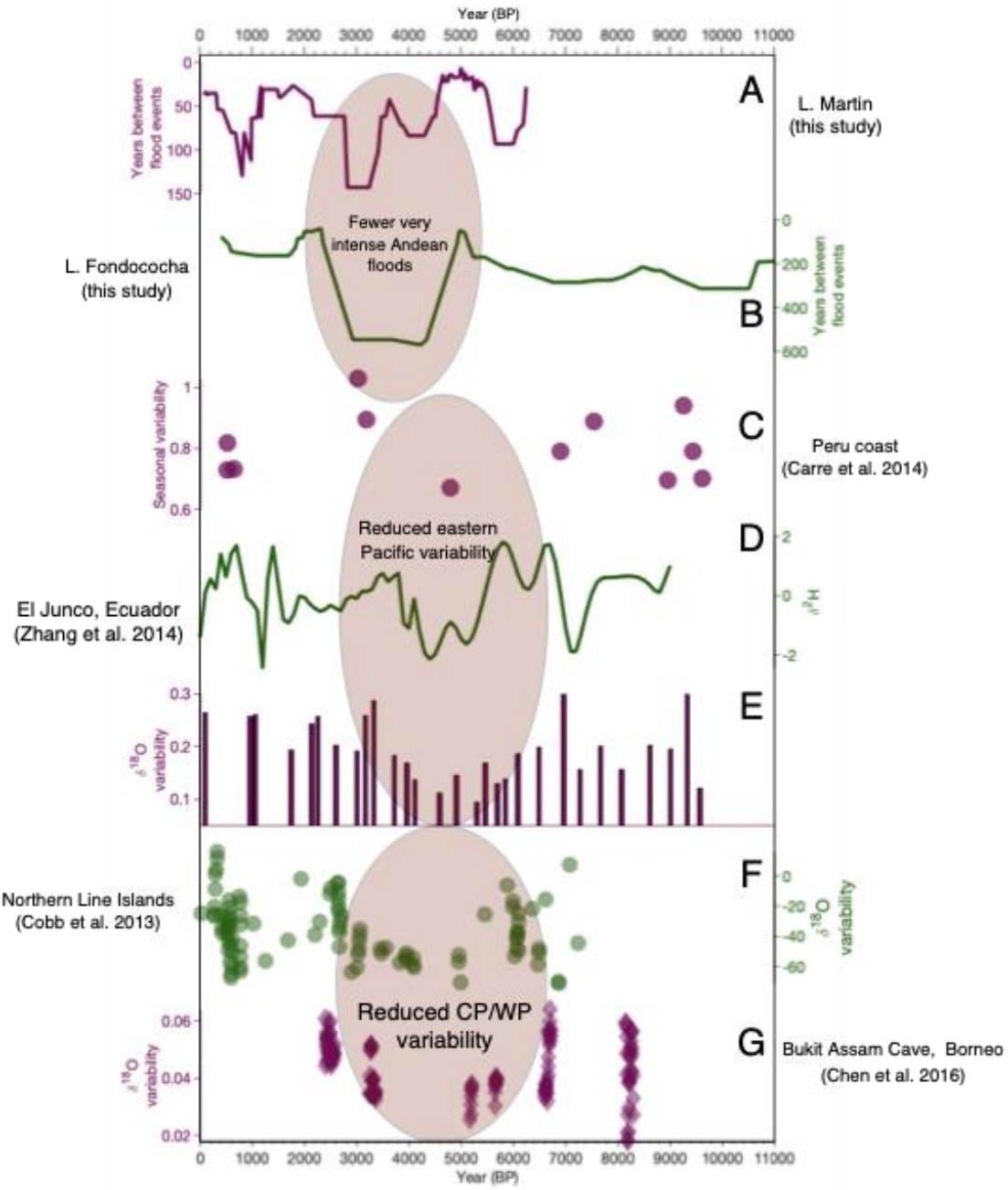

Figure 31. El Niño intensity proxies from around the Pacific. (A and B) Years between successive flood events at Laguna Martin and Laguna Fondococha (this study). (C) Interannual $\delta^{18}O$ variability from coastal Peruvian molluscan assemblages (Carre et al. 2014). (D) $\delta^{2}H$ of *b. braunii* from El Junco Lake, Galapagos (Zhang et al. 2014), in the eastern tropical Pacific. (E) $\delta^{18}O$ variability of eastern Pacific foraminifera (Koutavas and Joanides 2012) (F) ENSO-scale $\delta^{18}O$ variability from Palmyra atoll corals (Grothe et al. 2020) and (G) Bukit Assam Cave, Borneo (Chen et al. 2016), central and western tropical Pacific, respectively.

3.4.4 Drivers of ENSO frequency and intensity

Even if a coherent picture of El Niño frequency and intensity emerges from the qualitative intercomparison of similar proxy records, a more significant question remains unanswered: what drives changes in the frequency and intensity of El Niño events, and of ENSO as a whole? While orbital configurations explain some long-term trends in paleo-ENSO records (White et al. 2020, Carre et al. 2021), prominent high-frequency variability common to these same sources demonstrate that the relationship of ENSO to insolation is not simple (Emile-Geay et al., 2016). The influence of insolation on ENSO has been most pronounced after 6 kyr BP (Carre et al. 2021); prior to this time, other factors such as reduced tropical dust flux, which increased shortwave radiation in the eastern tropical Pacific, may have reduced ENSO variance (Pausata et al. 2017). Additionally, the early Holocene was marked by periodic meltwater fluxes into the North Atlantic, which may serve to both enhance ENSO amplitude as well as shift its spatial configuration (Timmerman et al. 2007, Williamson et al. 2018). Significantly, while some studies indicate meltwater flux and subsequent reduction of the Atlantic Meridional Overturning Circulation (AMOC) will enhance ENSO amplitude (Dong and Sutton, 2007), others indicate it will also lengthen the ENSO period (Williamson et al. 2018). The same forcing mechanism, therefore, may have the opposite effects on ENSO frequency and ENSO amplitude. Some proxy records suggest a decline in the strength of AMOC during the LIA (Moffa-Sanchez and Hall 2017), which could help explain the longer periodicities in ENSO frequency proxies and high amplitude of ENSO intensity proxies. Other studies, however, indicate that AMOC was not uniformly weaker during the LIA (Lapointe and Bradley 2021, Rahmstorf et al. 2015).

Pantropical climate interactions have increasingly been invoked as major components of the ENSO system in recent years (Cai et al. 2019). The magnitude of variability in the Indian

Ocean Dipole (IOD) has been shown to covary with ENSO over a variety of timescales-that is, when IOD variability is high, ENSO variability is also high (Abram et al. 2020a). Additionally, positive IOD events, which peak in boreal summer, may facilitate the formation of particularly intense EP El Niño events (Hameed et al. 2018). We note close correspondence between flood events recorded in Laguna Martin (those likely representing particularly intense El Niño events) and the occurrence of extreme positive IOD events documented in coral oxygen isotope records (Abram 2020b, Fig. 32). The middle 17th century, which has previously been identified as a period of remarkably intense ENSO (Cobb et al. 2003) and IOD (Abram et al. 2020b) variability, also shows frequent flooding at Laguna Martin (Fig. 32) Indeed, three extreme positive IOD events which occurred between 1650 and 1680 are matched by a unique deposit in Laguna Martin which seems to show three flooding events in rapid succession (Fig. 32) Indeed, due to short term increases in sedimentation rate associated with rapid alluviation (Moy et al. 2002), these three events are likely closer in age than can be detected by the age model, making them even more closely match the timing of extreme positive IOD events. As noted by Abram et al. (2020), this temporal clustering of particularly strong IOD-ENSO events has important implications for short- and medium-term forecasting and predictability.

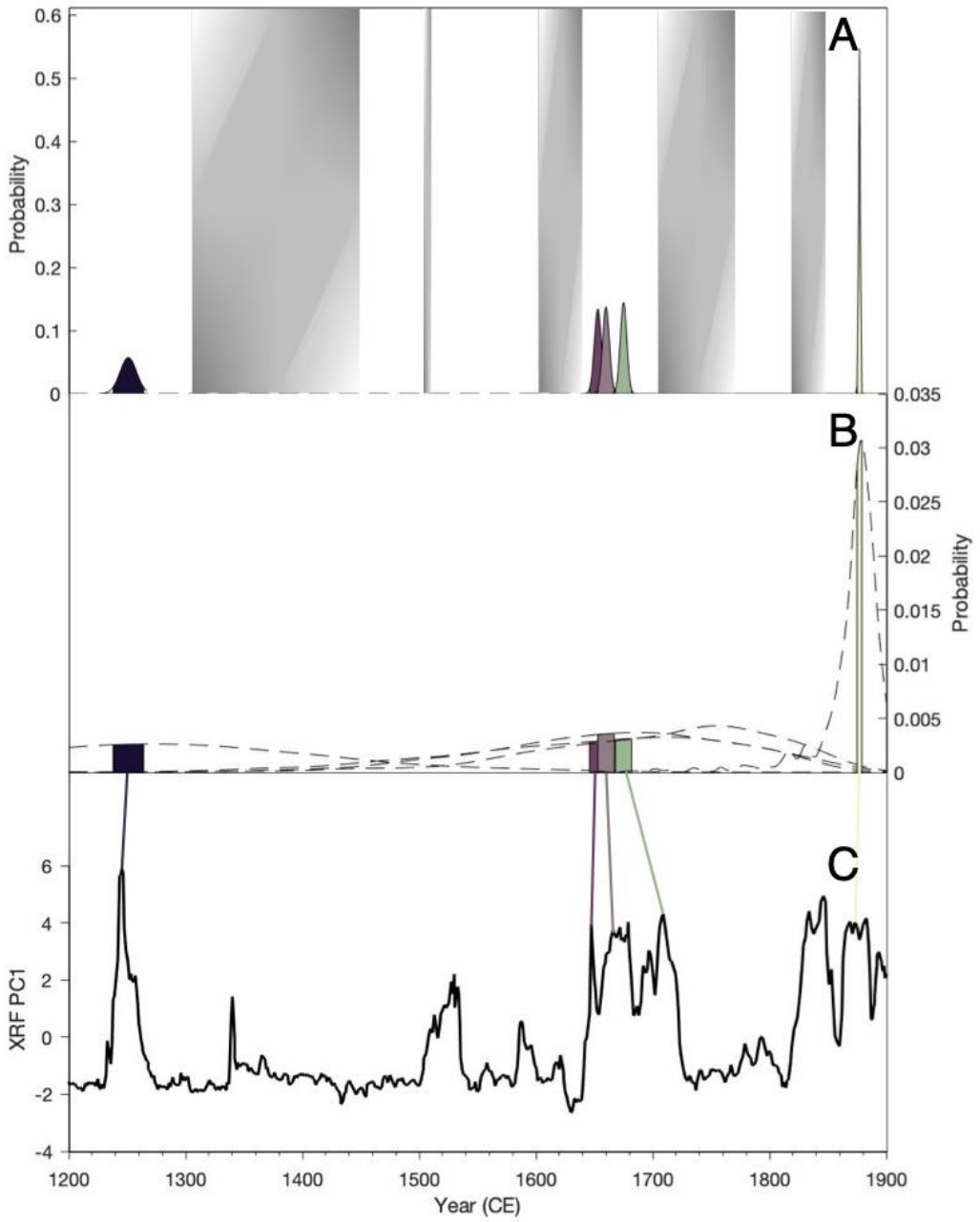

Figure 32. Comparison of extremely powerful Indian Ocean Dipole events (epIOD, Abram et al. 2020) and prominent flood deposits recorded by XRF PC1 of Laguna Martin. Top panel indicates probability density functions (PDFs) of coral-based epIOD events according to the classification scheme of Abram et al. (2020). Middle panel shows PDFs of prominent flood deposits shown in the bottom panel. Highlighted area in middle panel shows the temporal overlap between epIOD PDFs and flood deposit PDFs. Gray bars indicate periods for which there is no coral coverage.

3.5 Conclusions

Watershed-scale topographic and geomorphic features are responsible for differences in flood driven clastic laminae at three lakes in Cajas National Park, Ecuador. These flood deposits in Laguna Pallcacocha have previously been tied to El Niño events and have provided one of the few continuous, high-resolution records of El Niño frequency for the Holocene. By examining two additional basins, we reconstruct the frequency of ENSO events of different magnitudes; hence helping to disentangle both the wavelength and amplitude of the paleo-ENSO signal. The Little Ice Age was marked particularly intense ENSO events, recorded in marine foraminifera, oxygen isotope data from corals which have been bandpass filtered, and flood deposits in the relatively insensitive Laguna Martin and Fondococha basins. The preceding Medieval Climate Anomaly appears to show a shorter ENSO periodicity but fewer extreme events, recorded by spectral analyses of tree rings and varved sediments, and the more sensitive Laguna Pallcacocha sedimentary sequence. While intensity and frequency proxies are generally similar for much of the Holocene, the 7-5 kyr BP ENSO quiescent period seen in proxies sensitive to changes in ENSO wavelength appears to have harbored occasionally extreme El Niño events. Internal dynamics, or external forcing unrelated to insolation (i.e atmospheric dust flux or interactions with other ocean basins) must be invoked to explain changes in ENSO wavelength and amplitude. The records will provide valuable benchmarks against which modelling research devoted to disentangling the respective drivers of changes in the wavelength and amplitude of the ENSO signal can be examined.

4.0 A link between hydroclimate variability and biomass burning during the last millennium in the interior Pacific Northwest

We present oxygen isotope and charcoal accumulation records from two lakes in eastern Washington that have sufficient temporal resolution to quantitatively compare with tree-ring records and meteorological data. Hydroclimate reconstructions from tree-rings and lake sediments show close correspondence after accounting for seasonal- to centennial- scale temporal sensitivities. Carbonate $\delta^{18}O$ measurements from Castor and Round lakes reveal that the Medieval Climate Anomaly (MCA) experienced wetter November-March conditions than the Little Ice Age (LIA). Charcoal records from Castor, Round, and nearby lakes show elevated fire activity during the LIA compared to the MCA. Increased multidecadal hydroclimate variability after 1250 CE is evident in proxy records throughout western North America. In the Upper Columbia River Basin, multidecadal wet periods during the LIA may have enhanced fuel loads that burned in subsequent dry periods. A notable decline in biomass burning occurred with Euro-American settlement in the late 19th century.

4.1 Introduction

Recent droughts and wildfire seasons in western North America are among the most severe in recorded history, driven by accelerating anthropogenic climate change and fire exclusion practies (Higuera and Abatzoglou 2021, Williams et. al 2020, Marlon et al. 2012). Paleoclimate proxy evidence can provide context for current and projected climate-fire relationships (Marlon et

al. 2012). Oxygen isotope ($\delta^{18}O$) records from lake sediments can be used to study precipitation-evaporation balance, while charcoal accumulation records can identify the occurrence of fires on the landscape. In northwestern North America, $\delta^{18}O$ of lacustrine carbonates in hydrologically closed lake basins primarily reflect cool-season (November-March) precipitation (Steinman et al. 2010a), with more depleted $\delta^{18}O$ values indicating wetter conditions. This sensitivity to cool season moisture is due to generally wet cool-seasons and negligible evapotranspiration between November and March, which have outsized effects on overall water balance (Steinman et al. 2013a). Precipitation in the Upper Columbia River Basin (Fig. 33) primarily comes from Pacific frontal storms during the cool-season, with substantial interannual/decadal climate variability resulting from the El Niño Southern Oscillation (ENSO) and the Pacific Decadal Oscillation (McAfee and Wise 2016). El Niño and PDO-positive conditions tend to deflect storm tracks southward, leading to decreased precipitation in northwestern North America; generally wetter cool-season conditions occur during La Niña/PDO negative intervals (Wise 2010). $\delta^{18}O$ records from the region show generally wetter winters during the Medieval Climate Anomaly (MCA, 950-1250 CE) than during the subsequent Little Ice Age (LIA, 1450-1850 CE, Masson-Delmotte et al. 2013, Steinman et al. 2012, Steinman et al. 2014, Shuman et al. 2018), while many tree-ring reconstructions suggest the MCA was marked by widespread summer drought across western North America (Cook et al. 2004).

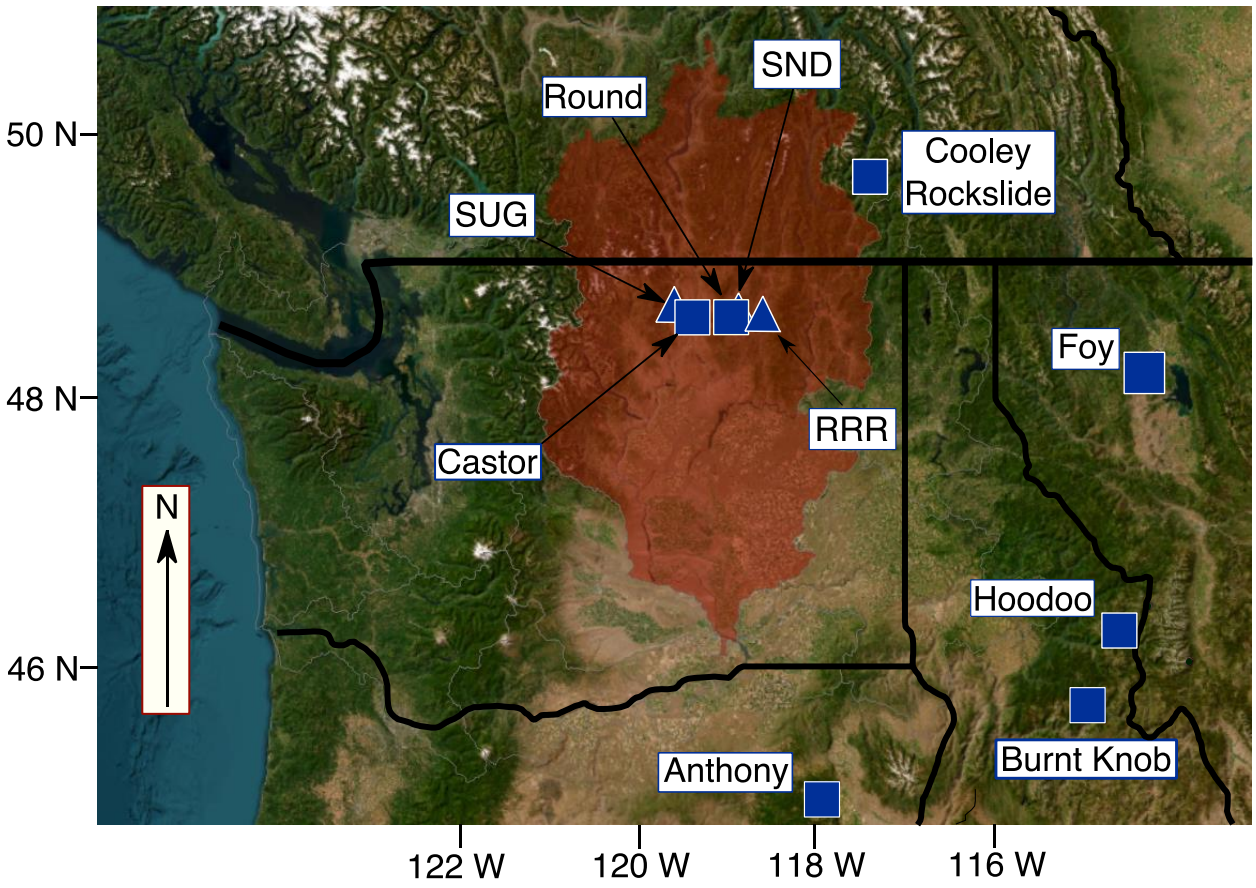

Figure 33. Location of Castor and Round Lakes within the Columbia River Basin (red shading) and other regional proxy records.

Composites of charcoal data show more fire activity during the MCA than in the LIA (Marlon et al. 2012), although there is considerable variability at different sites (Walsh et al. 2015, Walsh 2023). Both charcoal and fire-scarred tree-ring records show abrupt changes in continental-scale climate/fire relationships associated with Euro-American settlement (Marlon et al. 2012). ENSO and the PDO have also been shown to influence fire synchroneity in the eastern Cascades over the past several centuries (Heyerdahl et al. 2008), with severe fire years associated with El Niño/PDO+ conditions. The amplitude of interannual and multidecadal climate variability has also been hypothesized to drive biomass burning, as prolonged wet periods generate abundant well-connected fine fuels which subsequently desiccate and burn during droughts (Walsh et al.

2015, Cooper et al. 2022). Paired, high-temporal resolution evidence linking hydroclimate to fire activity from the same sites remains lacking, however.

Here, we present high-resolution $\delta^{18}O$ and charcoal records from Castor Lake (48.54 N 119.56 W; 594 m a.s.l.) and Round Lake (48.61 N 119.12 W; 654 m a.s.l.) that span the last 1200 years (Fig. 33) and compare them to instrumental climate data and nearby tree-ring records. This approach allows us to better understand the climatic controls on sedimentary $\delta^{18}O$ records, which, when paired with corresponding charcoal accumulation data, improves our understanding of the climatic and non-climatic drivers of fire in this semi-arid western ecosystem.

4.2 Materials and Methods

4.2.1 Study area

Castor and Round Lakes lie in stagnant-ice depressions formed during the late-Pleistocene recession of the Cordilleran Ice Sheet in the Upper Columbia River Basin (Kovanen and Slaymaker 2004, Fig. 33). These sites are surrounded by parkland of *Pinus ponderosa*, *Pseudotsuga menziesii and Abies grandis,* with *Artemisia tridentata* present in forest openings and nearby steppe. Fifty percent of annual precipitation (<400 mm/yr at both sites) falls between November and March (PRISM Climate Group https://prism.oregonstate.edu). Near the lakes are three *P. ponderosa* stands (SUG, 48.60 N -119.70 W 844 m a.s.l; RRR 48.51 N -118.75 W 1156 m a.s.l; SND 48.59 N -119.14 W 965 m a.s.l) that were previously analyzed for standard total ring width, earlywood width, latewood width and blue intensity as part of a paleoclimate investigation (Dannenberg and Wise 2016) (Fig. 33).

4.2.2 Coring and sampling

Freeze cores (Besonen et al. 2008) were retrieved from Castor Lake (core B-18) and Round Lake (core B-18) in February 2018 to recover the mud-water interface and uppermost sediments. The stratigraphy of the Castor Lake freeze core was spliced to that from an existing hammer core (Castor A-03, Nelson et al. 2011) and the Round Lake record was correlated to the stratigraphy of a longer Livingstone piston core taken in 2017.

4.2.3 Lithology and chronology

One cc samples were taken from each core at 0.5-cm intervals and were analyzed for bulk density and carbonate composition according to the method of Heiri et al. 2001. A chronology was developed via Bchron v. 4.7.6 for both lakes using ^{137}Cs radioisotopes (nCastor=3 nRound=1), radiocarbon dates (nCastor=2 nRound=4), the Mount Saint Helens Wn tephra layer in Castor Lake (1480 CE, Mullineaux 1996; not successfully identified at Round Lake) (Fig. 34, Table 3).

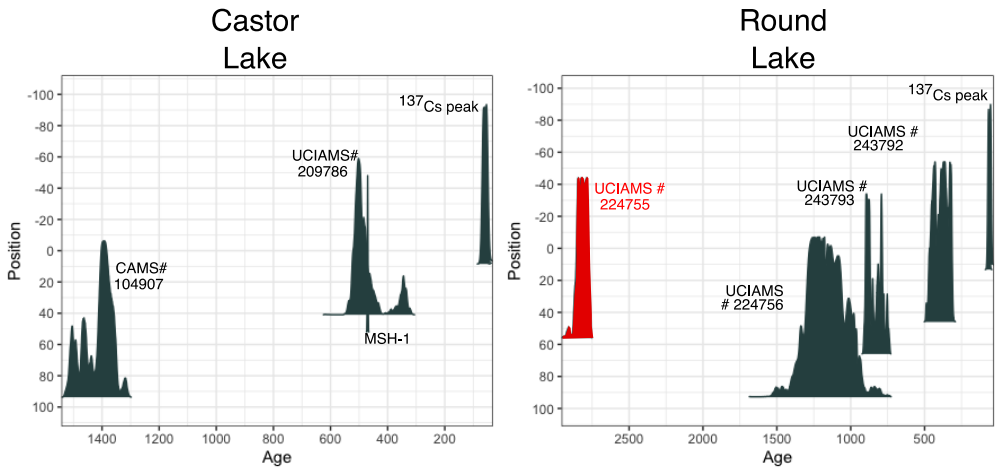

Figure 34. Probability distributions for calibrated age control points in Castor and Round Lake. Red indicates a ^{14}C date that yielded an erroneous date (likely due to low volume).

Table 3. Age model information for Castor (A) and Round Lake (B). Red cells indicate assays that did not yield usable dates for the final age model.

A			**Castor Lake**				
Depth range (cm)	Type	Date (uncalibrated)	1s error	Core	Material	Thickness (cm)	calCurves
0-.5	210Pb	N/A	N/A	Castor B-18 Freeze	Bulk sediment	0.5	N/A
4.5-5	210Pb	N/A	N/A	Castor B-18 Freeze	Bulk sediment	0.5	N/A
5-5.5	210Pb	N/A	N/A	Castor B-18 Freeze	Bulk sediment	0.5	N/A
6-6.5	137 Cs	-16	5	Castor B-18 Freeze	Bulk sediment	0.5	Normal
7-7.5	137 Cs	-13	5	Castor B-18 Freeze	Bulk sediment	0.5	Normal
8.5-9	137 Cs	-9	5	Castor B-18 Freeze	Bulk sediment	0.5	Normal
9-9.5	210Pb	N/A	N/A	Castor B-18 Freeze	Bulk sediment	0.5	N/A
12.5-13	210Pb	N/A	N/A	Castor B-18 Freeze	Bulk sediment	0.5	N/A
13-13.5	210Pb	N/A	N/A	Castor B-18 Freeze	Bulk sediment	0.5	N/A
13.5-14	210Pb	N/A	N/A	Castor B-18 Freeze	Bulk sediment	0.5	N/A
14.5-15	210Pb	N/A	N/A	Castor B-18 Freeze	Bulk sediment	0.5	N/A
15-15.5	210Pb	N/A	N/A	Castor B-18 Freeze	Bulk sediment	0.5	N/A
17-17.5	210Pb	N/A	N/A	Castor B-18 Freeze	Bulk sediment	0.5	N/A
20.5-21	210Pb	N/A	N/A	Castor B-18 Freeze	Bulk sediment	0.5	N/A
41-42	14 C	435	40	Castor B-18 Freeze	Charcoal macro	1	intcal20
52-53	tephra (MSH-1)	470	52	Castor Hammer A-03	Tephra	1	Normal
93.5-94	14 C	1530	35	Castor Hammer A-03	Charcoal macro	0.5	intcal20
B			**Round Lake**				
Depth range (cm)	Type	Date (uncalibrated)	1s error	Core	Material		
5-5.5	210Pb	N/A	N/A	Round A-18 Freeze	Bulk sediment	0.5	N/A
6-6.5	210Pb	N/A	N/A	Round A-18 Freeze	Bulk sediment	0.5	N/A
7-7.5	210Pb	N/A	N/A	Round A-18 Freeze	Bulk sediment	0.5	N/A
8-8.5	210Pb	N/A	N/A	Round A-18 Freeze	Bulk sediment	0.5	N/A
8.5-9	137Cs	-13	5	Round A-18 Freeze	Bulk sediment	0.5	Normal
9-9.5	210Pb	N/A	N/A	Round A-18 Freeze	Bulk sediment	0.5	N/A
45-47	14C	335	25	Round A-17	Charcoal macro	2	intcal20
55-57	14C	2730	25	Round A-17	Charcoal macro	2	N/A
65-66	14C	915	20	Round A-17	Charcoal macro	1	intcal20
95-95.5	14C	1200	130	Round A-17	Charcoal macro	0.5	intcal20

4.2.4 Isotopic analysis

Samples for $\delta^{18}O$ were processed according to the methods of Nelson et al. 2011. Samples were extracted with dehydrated phosphoric acid at 70°C under vacuum and measured with a Kiel-III preparation device coupled to a Finnigan MAT 252 gas-ratio mass spectrometer at the University of Arizona with 1σ precisions of 0.1‰ for $\delta^{18}O$ on repeated measurements of NBS-19 and NBS-18 standards.

4.2.5 Charcoal analysis

Samples for charcoal analysis were taken at contiguous 0.5-cm intervals. 1 or 2 cm^3 samples of sediment were disaggregated in sodium hexametaphosphate and bleach, sieved through a 125-μm mesh screen, and counted under a binocular microscope at <10x magnification following Whitlock and Larsen (2002). Charcoal counts for both lakes were converted to charcoal accumulation rates (CHAR, particles/cm^2 yr^1). The CHAR time series were interpolated to 7-year timesteps, the median timestep of the Castor Lake record (and greater than that of Round Lake). Decadal to sub-decadal fire-return intervals that characterize these dry forests were too short to detect individual fire episodes in the CHAR time series, and we instead relied on the trends in CHAR to describe changes in fire activity (Walsh et al. 2023).

4.2.6 Statistical analysis

Comparison of modern tree-ring chronologies and meteorological data (1895-2012) were conducted by averaging the 9 4-km resolution PRISM climate model grid cells centered on each

site. April 1 snow water equivalence (SWE) data from the Upper Columbia River Basin are from Pederson et al. (2011), covering the period 1936-2006.

For Castor Lake, Pearson's correlations between 1900-2016 were conducted on annually resolved $\delta^{18}O$ measurements (Fig. 35 a and b). For comparison to tree-ring stands SUG, SND, and RRR between 1600-2016, correlations were carried out by interpolating the lowpass-filtered tree-ring chronologies to a 3-year resolution (Fig. 35c, 40). Detrending of the Castor and Round Lake $\delta^{18}O$ records for comparison with tree-ring chronologies were carried out using 1st and 3rd degree polynomials. Autocorrelation was accounted for by estimating the effective degrees of freedom (Hu et al. 2017) per the methodology of Steinman et al. 2022.

We calculate 60-year moving variances (in the case of lake sediment proxies) by linearly interpolating data to the minimum timestep justified by the temporal resolution of each dataset (3 years for $\delta^{18}O$ datasets in Castor and Round Lake, 6 years in $\delta^{18}O$ Foy Lake, MT) and measuring the variance of each proxy in a moving 60 year window. 60 year intervals were used to accurately capture multidecadal climate phenomena; however, window lengths between 48 and 72 years did not substantially alter results. Pearson's correlations between proxies (Table 4) were conducted by interpolating data to the same 6-year time-step over the period covered by each pair of proxies. Correlations between the charcoal accumulation record and the oxygen isotope moving variances were conducted by interpolating the moving variance time series to the same resolution as the charcoal records. Given non-linear relationships, we used Spearman's ranked correlation and compared the charcoal record to the 60-year moving window that ends at the beginning of the charcoal sampling interval (rather than the window centered on the charcoal sampling interval). This was done to evaluate hydroclimate conditions *prior* to each charcoal datapoint,. Correlations between charcoal records and SUG, SND, and RRR were conducted using the lowpass filtered

tree-ring width (TRW) records interpolated to a 3-year time step (the approximate median charcoal sampling interval between 1650 and 1910).

To test for significant differences between the MCA and LIA in the 60-year moving variance time series, two-sample Kolmogorov-Smirnov tests were used. The presence of serial autocorrelation invalidates the assumption of independent observations and can lead to a spurious rejection of the null hypothesis that the two time series come from the same distribution. We use the methods of Lanzante (2021), which developed a Monte Carlo approach with a first-order autoregressive model to account for autocorrelation and improve the robustness of results.

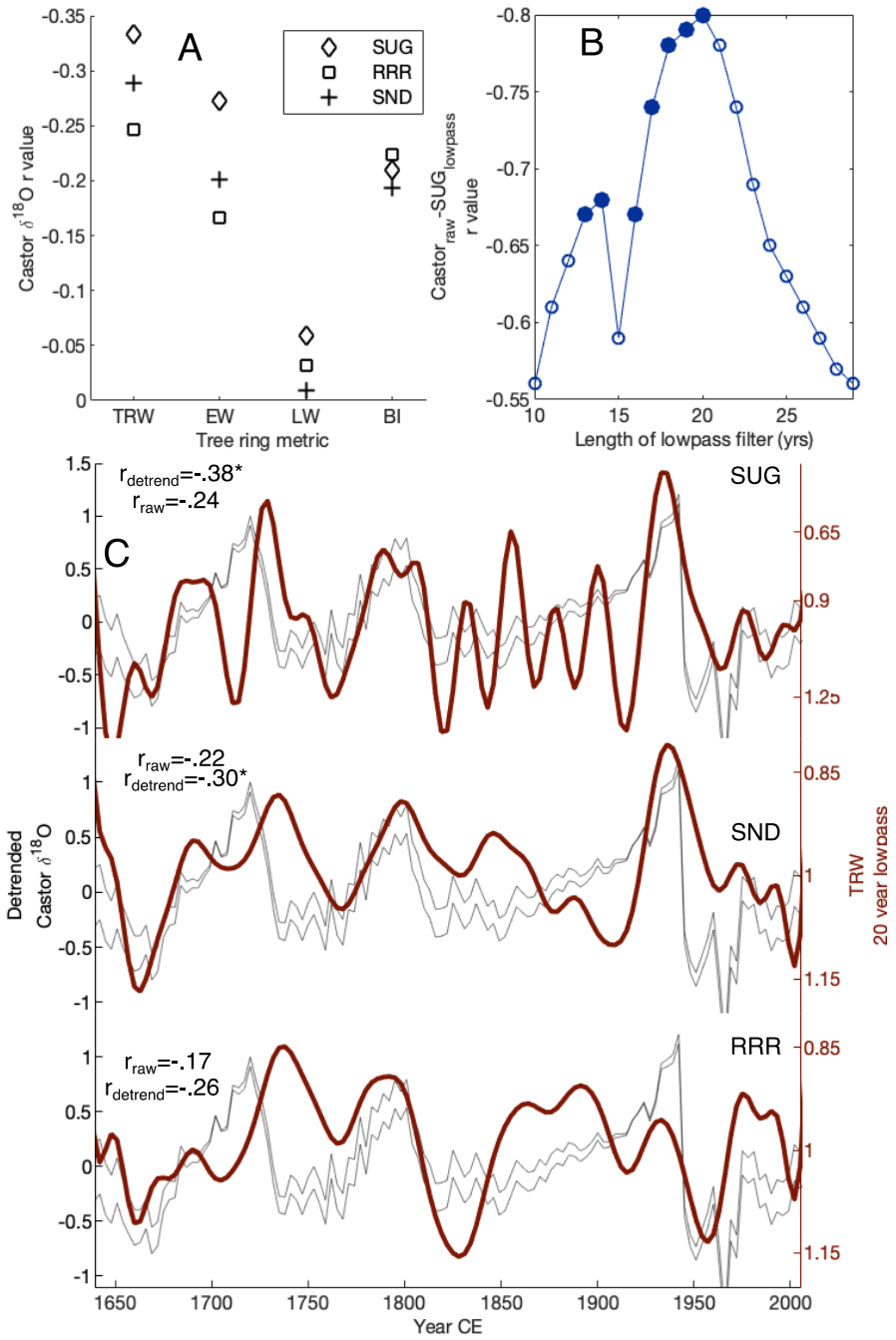

Figure 35. Isotopic correlations with nearby tree-ring records. (A) Correlations between unfiltered Castor Lake annual $\delta^{18}O$ record (1900-2012) and unfiltered total ring-width, earlywood, latewood, and blue-intensity chronologies from three sites in the eastern Washington (Dannenberg and Wise, 2016). (B) Correlation coefficients between the unfiltered Castor $\delta^{18}O$ dataset (1900-2012 CE) and SUG ring-width record with lowpass filters of different lengths. Solid circles represent datapoints for which $p < 0.1$. (C) 20-year lowpass filtered tree-ring chronologies (thick red lines) and detrended Castor Lake $\delta^{18}O$ values (thin black lines indicate 1st and 3rd degree polynomial detrending). Asterisks next to r values indicate statistical significance ($p<0.1$)

4.3 Results

Castor and Round lake waters are evaporatively enriched with respect to the global meteoric water line (Fig. 36). Sediments from Castor and Round lakes from the last 1200 years primarily consist of millimeter-scale laminae alternating between light-colored carbonate-rich and darker-colored organic-rich sediments. Both sequences consist of >25% $CaCO_3$ throughout. $\delta^{18}O$ values vary between -6.5 and -2‰ for Castor Lake and -14 and -8‰ for Round Lake over the past 1200 years. $\delta^{18}O$ values for both lakes were on average more enriched during the LIA (-4.3 and -11.3 at Castor and Round lakes, respectively) than during the MCA (-5.0 and -11.8). Pronounced periods of $\delta^{18}O$ enrichment occurred between approximately 1010-1070 CE, 1330-1430 CE, and 1710-1740 CE at both lakes (Fig. 37).

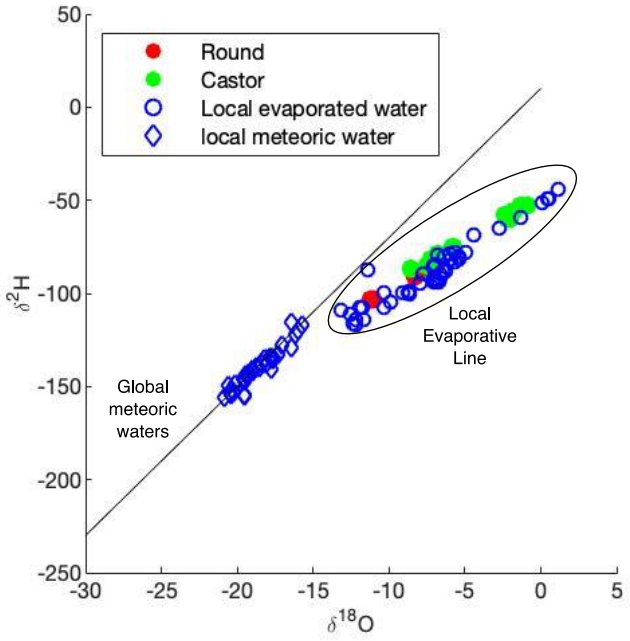

Figure 36. Oxygen and hydrogen isotope composition of global and local meteoric and evaporative waters. Castor Lake (green dots) and Round Lake (red dots) water samples were taken between 2000 and 2018.

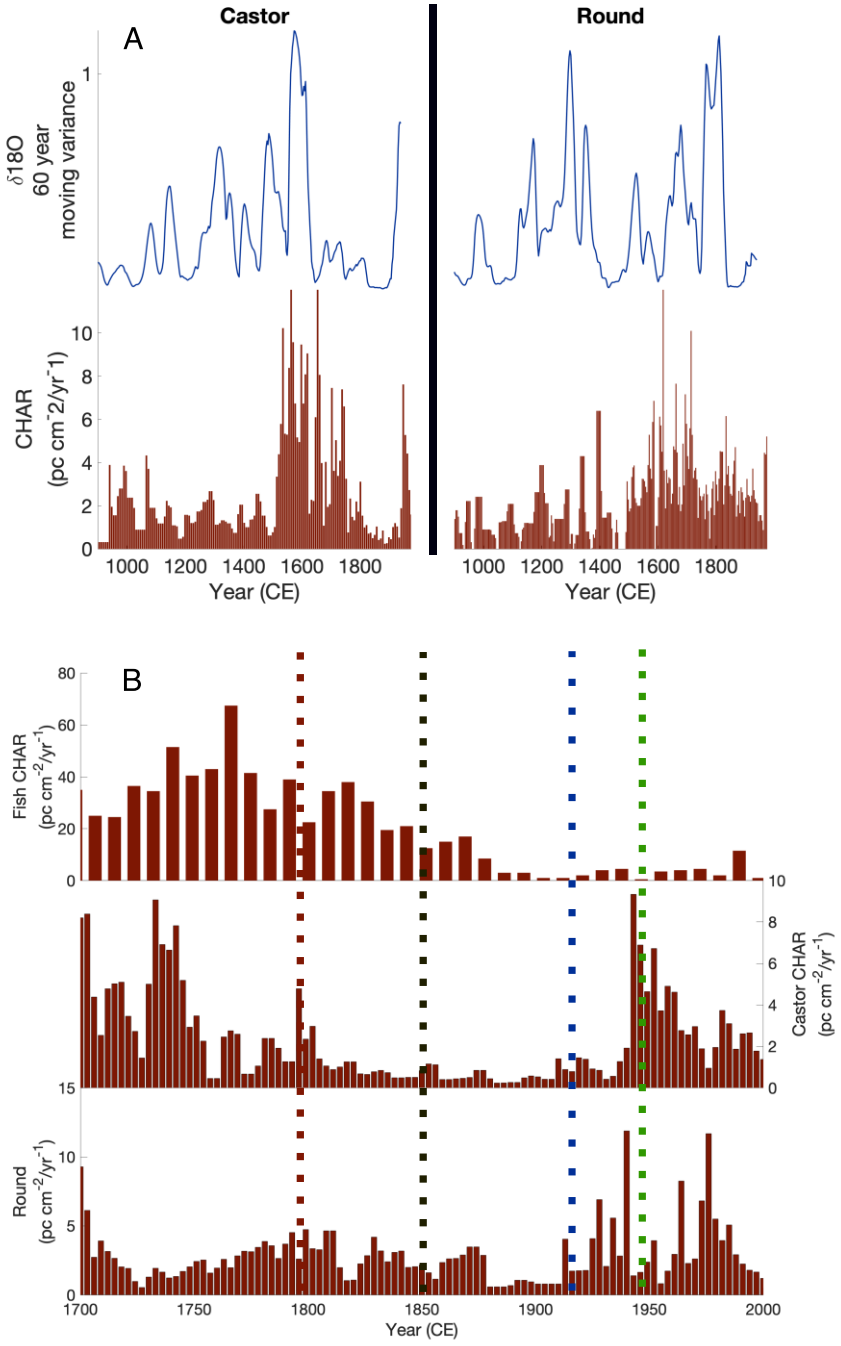

Figure 37. Isotopic and charcoal results from Castor and Round Lakes. (A) Charcoal accumulation rate (CHAR) and 60-year moving average of variances of $\delta^{18}O$ from Castor and Round lakes over the past millennium. (B) CHAR from Fish, Castor, and Round Lake between 1700-2000 CE. Red line indicates the first documented smallpox case (Boyd et al. 1999) among Native American groups in the region, black line indicates the establishment of Euro-American grazing practices in the region (Walsh et al. 2018), blue line represents onset fire suppression policies and green line represents post-WWII increase in fire suppression efficacy.

The Castor Lake $\delta^{18}O$ record is approximately annually resolved between 1900-2016 CE, as indicated by core top ^{137}Cs-derived dates over the past century and constrained by underlying ^{14}C dates (Fig. 35). This resolution allows for quantitative comparison of results with instrumental data and nearby tree-ring records (Schoenemann et al. 2020). In the tree-ring data, cool-season precipitation is most highly correlated with total ring-width, earlywood, latewood, and blue intensity chronologies at SUG and has the lowest correlation with trees in the RRR stand (Fig. 38). Greater sensitivity to cool-season moisture in the SUG and SND stands indicates these chronologies come from moisture-limited trees (Cluster 1 according to Coulthard et al. 2021). RRR trees, which exhibit a weak but statistically significant negative relationship with regional SWE (Fig. 39), may be more limited by energy rather than by moisture, a trait commonly seen in the Cascade Range to the west (Cluster 3, Coulthard et al. 2021). Castor Lake $\delta^{18}O$ values also exhibit statistically significant correlations ($p<0.1$) between 1900-2016 with cool-season and year-round precipitation but not with warm-season precipitation (Fig. 35). The SUG total ring-width record most closely matched Castor Lake $\delta^{18}O$ data (Fig. 35). Castor Lake $\delta^{18}O$ data also show high correlations with earlywood and blue intensity, and the lowest correlations with latewood, a warm-season precipitation indicator (Fig. 35a). Given the shared sensitivity to cool-season precipitation and correlation between recent TRW and ^{18}O, TRW is the most appropriate metric to compare to the sedimentary records (e.g., Fig. 35b and c).

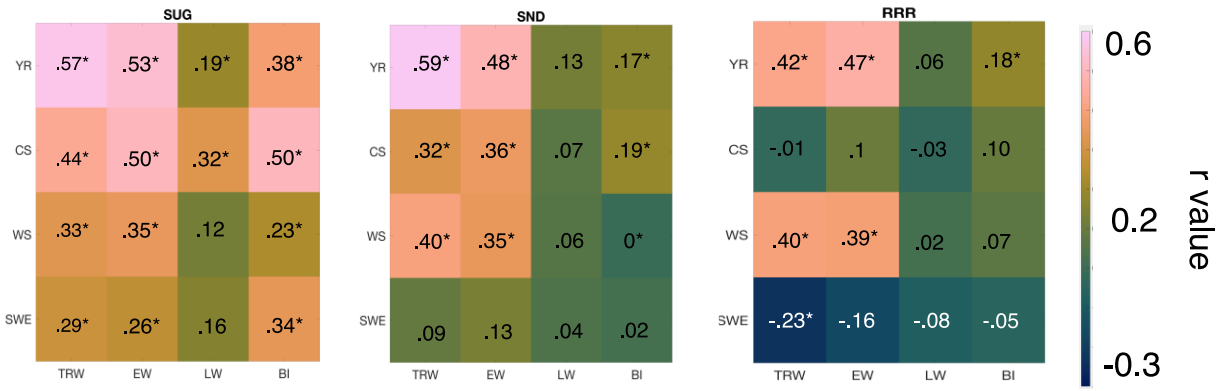

Figure 38. Pearson's correlation coefficients between different tree-ring metrics (TRW=total ring-width, EW=earlywood LW=latewood BI=blue intensity) and various meteorological parameters from 3 different tree-ring chronologies in eastern Washington. YR=year-round precipitation CS=cool season November-March WS=warm-season June-September SWE=snow-water equivalent. Asterisks indicate values which are significant ($p<0.1$) after accounting for autocorrelation.

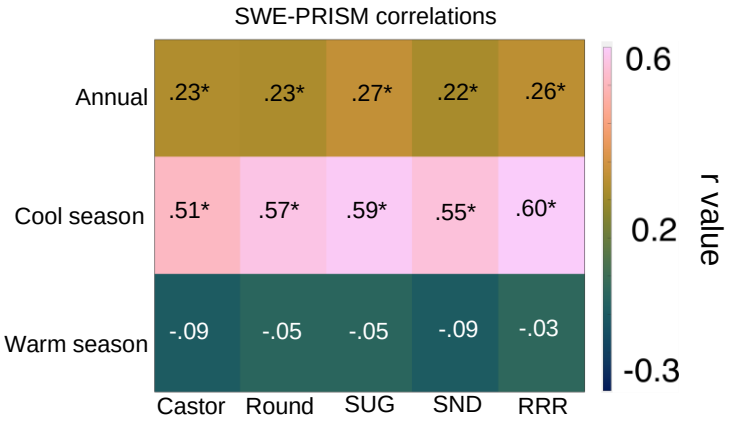

Figure 39. Correlations between the 1936-2006 SWE reconstruction (Pederson et al. 2011) and annual, cool-season, and warm season precipitation from PRISM grid cells. Asterisks indicate values which are significant ($p<0.1$) after accounting for autocorrelation.

Residence time of lake water causes serial autocorrelation in carbonate $\delta^{18}O$ values, effectively smoothing hydroclimate reconstruction (Steinman and Abbott 2013). To quantify the effect of the isotopic "memory" of lake water, lowpass filters of different lengths were applied to the SUG total ring-width record, and the smoothed chronology was regressed against the unfiltered Castor $\delta^{18}O$ record. A 20-year lowpass filter of the total ring-width data produced the most accurate match (Pearson's $r=-0.80$ $p<0.1$) (Fig. 35b, Fig. 40). Higher cutoff frequencies retain

climate variability which is removed by the residence time of lake water, while lower cutoff frequencies excessively smooth the tree-ring chronology (Fig. 40). Importantly, this correspondence empirically supports the modelled relationship between cool-season precipitation and lake sediment $\delta^{18}O$ values, showing that lake water residence time effectively integrates approximately 20 years of (primarily cool-season) precipitation (Steinman et al. 2010).

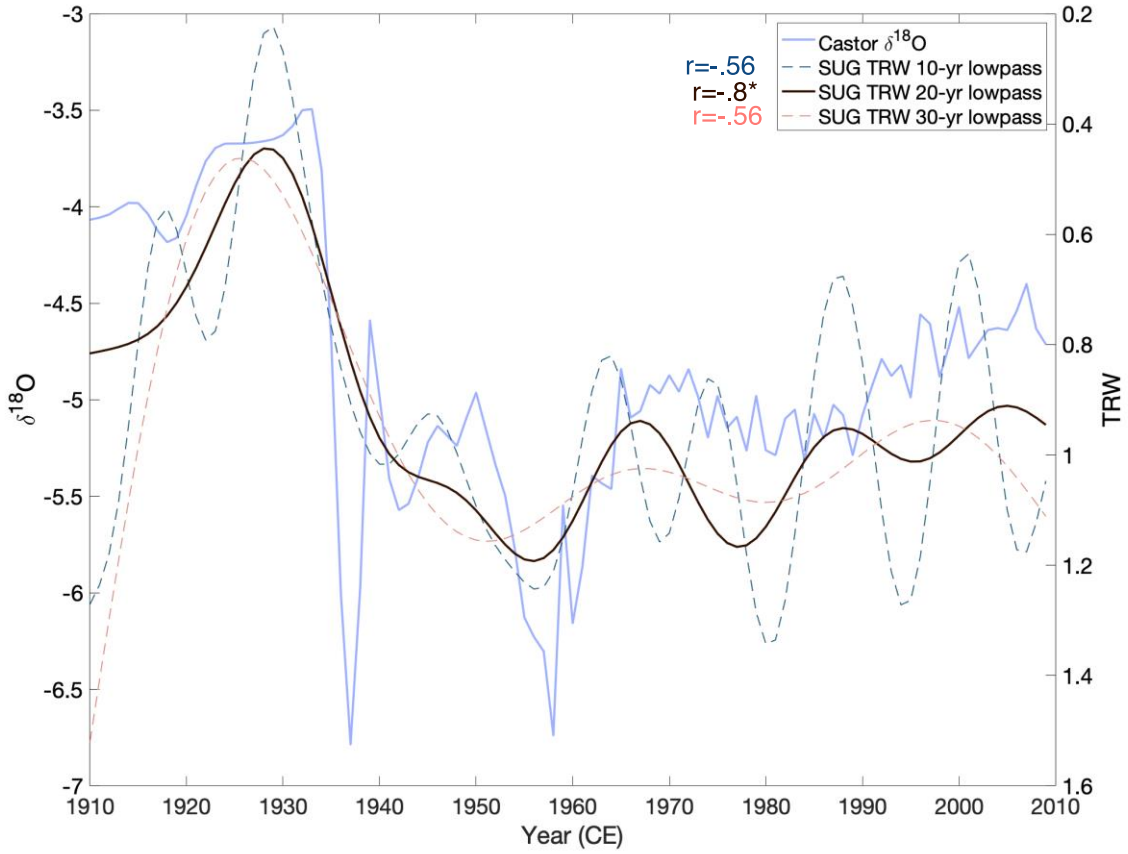

Figure 40. Time series of lowpass filtered SUG TRW and annually resolved Castor Lake isotope record used to generate correlations in Fig. 35B. Lowpass filters of different frequencies were passed through the TRW record to mimic the isotopic buffering experienced by the lake due to residence time of the water. Asterisks indicate statistical significance ($p<0.1$).

Relatively short lifespans of individual trees and the removal of age-related growth signals hinder the detection of low-frequency climate signals (Helama et al. 2017). Detrended Castor and Round Lake $\delta^{18}O$ records show higher correlations with each tree-ring chronology than the original

time series (Fig. 35C, Fig. 41) Hence, while residence time of lake water prevents sedimentary $\delta^{18}O$ records from preserving high-frequency variability, centennial-scale variability preserved in lake sediment records can be removed during the compositing of tree-ring chronologies.

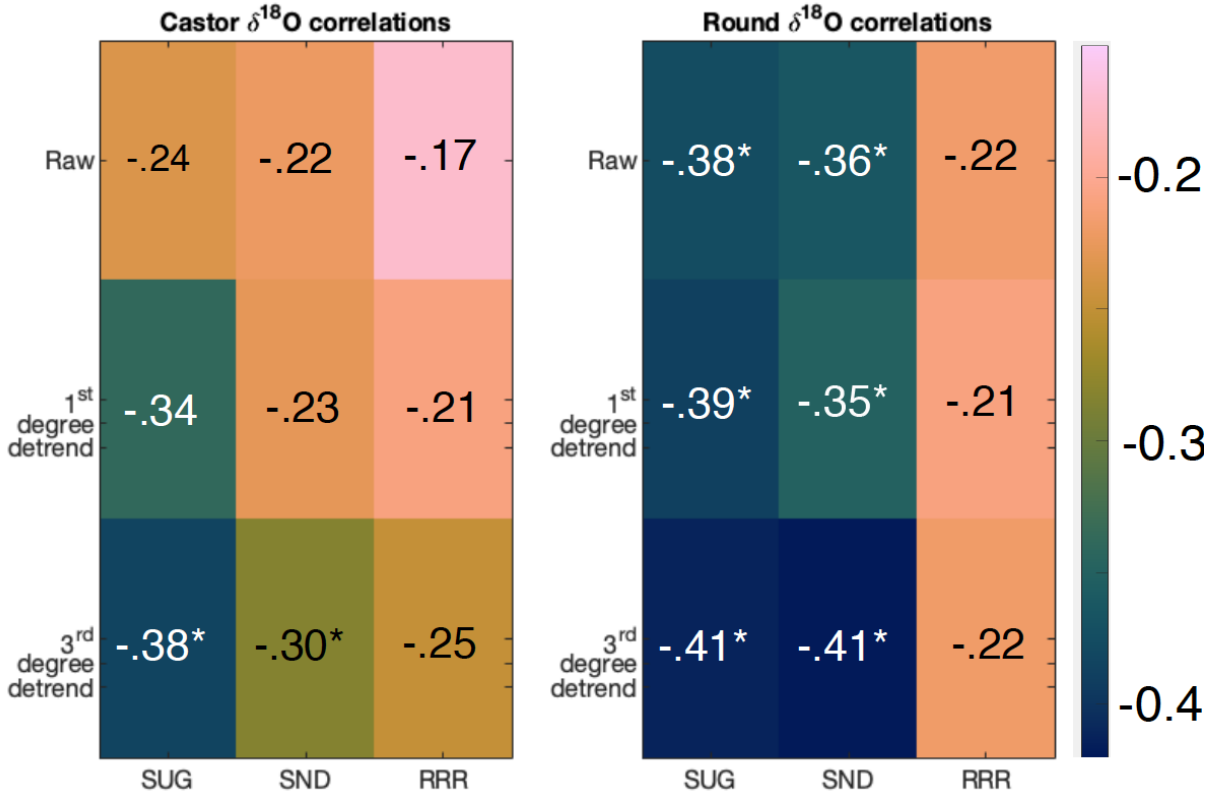

Figure 41. Correlations between Castor and Round Lake δ18O records and total ring-width chronologies (20 year low-pass filtered) with different detrending methods applied to the lake sediment chronologies. All time-series were interpolated to 3-year time steps. Asterisks indicate statistical significance ($p<0.1$).

Charcoal accumulation rates (CHAR) were generally low in both lakes from the beginning of the record to approximately 1000 CE. Between 1000 and 1500 CE, CHAR increased to maximum values of ~10 particles cm^{-2}/yr^{-1} and decline over the 19th and 20th centuries (Fig. 34). CHAR values are not significantly correlated to $\delta^{18}O$ records from either lake, nor to any tree-ring chronology (Fig. 42). At each lake, CHAR is significantly correlated to the 60 year moving variance of $\delta^{18}O$, however (Fig. 43).

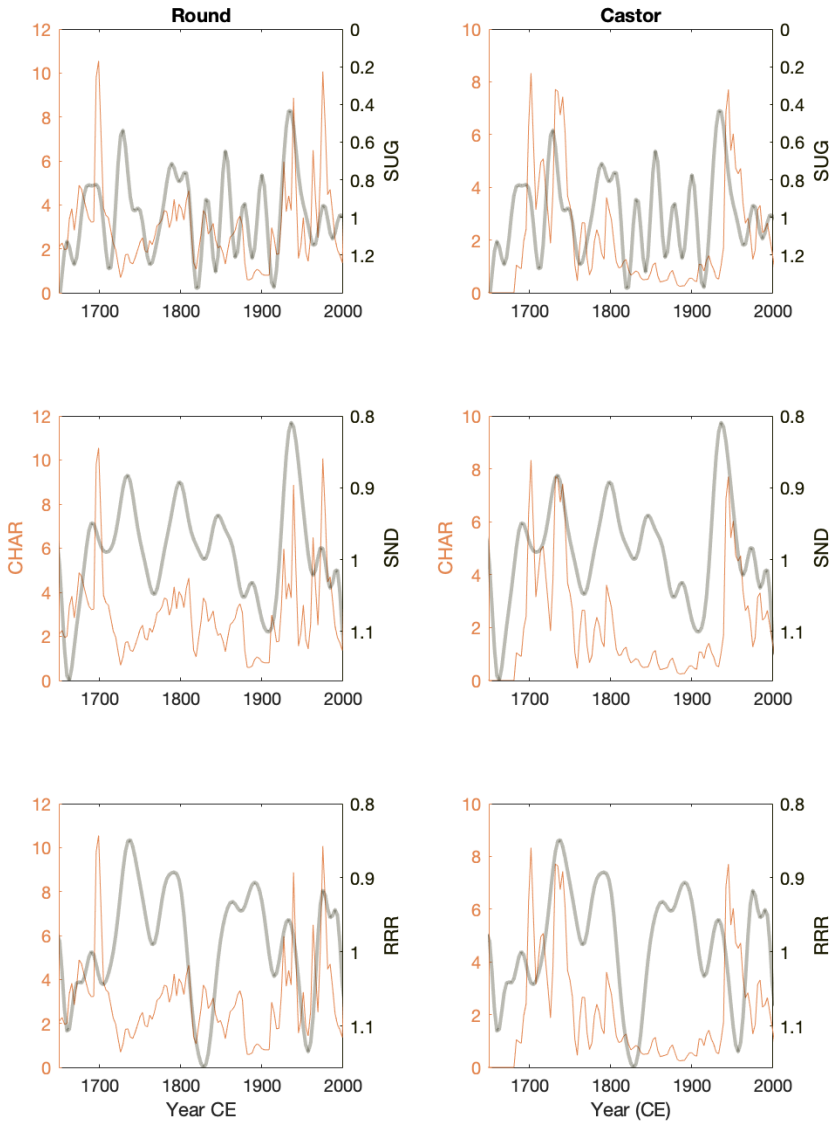

Figure 42. Time series of CHAR from Castor and Round Lake and proximal tree-ring width chronologies SUG, SND, and RRR. Pearson's p-values are greater than p=0.1 in each case.

4.4 Discussion

4.4.1 Climate and biomass burning in the Upper Columbia River Basin

Charcoal accumulation rates in Castor, Round and Fish Lake (Walsh et al. 2018) were low in the MCA and increased during the LIA, when cool-season conditions were generally drier than before (e.g., Steinman et al. 2014, Steinman et al. 2012, Macdonald and Case 2005, Mushet et al. 2023) and multidecadal hydroclimate variability was high (Fig. 37 Fig. 43). Nearby sites in northern Idaho (Baker Lake, 2300 m a.s.l, Hoodoo Lake, 1770 m a.s.l, Burnt Knob Lake, 2250 m a.s.l Fig. 30) and Montana (Foy Lake 1006 m a.s.l Fig. 30), also show increased charcoal accumulation during the LIA compared to the MCA (Brunelle et al. 2005; Brunelle and Whitlock 2003, Power et al. 2006). Raw CHAR values from Anthony Lake, OR (N 44.95, W -118.20, 2174 m a.s.l.) show little systematic trend over the past 1000 years (Long et al. 2019). Two charcoal records from subalpine forests which experience multi-centennial fire return intervals (Cooley and Rockslide lakes, 1515 m a.s.l. and 1539 m a.s.l. respectively, Fig. 33) show little similarity with one another, but document a decrease in fire activity after 1500 CE (Gavin et al. 2006). In summary, sites from the Upper Columbia River Basin which experienced short fire-free intervals prior to Euro-American settlement (Round, Castor, and Fish Lake) all show increased fire activity during the LIA, while the response of nearby montane forest sites which experience longer fire-free intervals are more heterogeneous. This stands in contrast to regional (Walsh et al. 2015) and continental-scale (Marlon et al. 2012) syntheses which indicate greater fire activity during the MCA.

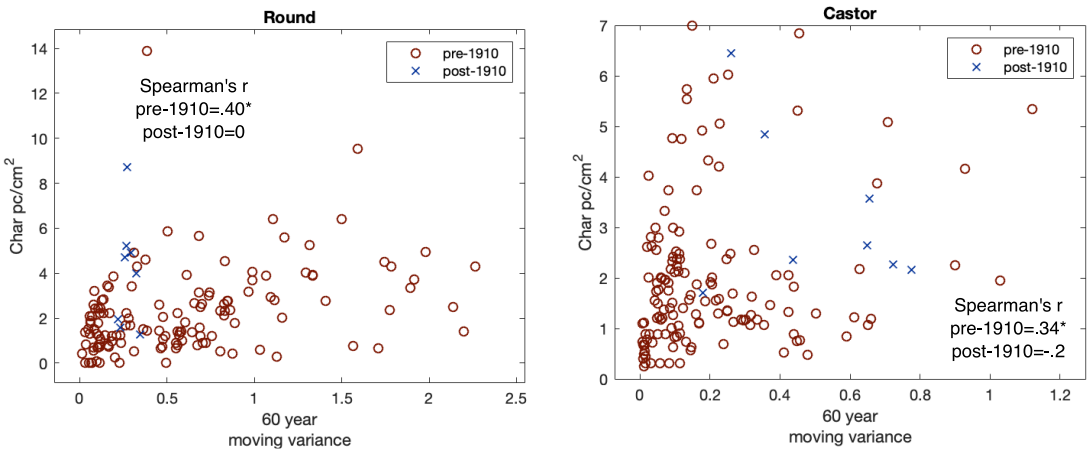

Figure 43. Scatter plots of 60 year δ18O moving variances and charcoal accumulation records from Castor and Round Lakes. Both show significant Spearman's ranked correlations (due to likely non-linear relations between variables) indicating amplified multidecadal climate variability and charcoal accumulation are linked. Asterisks indicate statistical significance at p<0.1 levels.

Although the fire season in the dry forests of the Upper Columbia River Basin occurs between May and October, winter and spring precipitation influences soil moisture and fuel conditions (Wright and Agee 2004, Halofsky 2020). Tree-ring studies from the region tie recent fire activity to variations in ENSO and the PDO, which alters winter moisture delivery as well as summer temperatures (Heyerdahl et al. 2008, Hessl et al. 2004). At Castor and Round Lakes, the amplitude of multidecadal climate variability shows significant correlations with CHAR (Fig. 37, Fig. 43). The assumed mechanism linking Pacific climate variability to fire is as follows: cool-season precipitation during La Niña/negative PDO phases leads to fuel production more densely vegetated landscapes. Subsequent droughts periods desiccate fuels, leading to more intense and regionally synchronous fire seasons. This relationship is most significant in high-frequency fire regimes and helps explain the contrast between Castor, Round, and Fish Lakes and higher elevation sites from elsewhere in the Upper Columbia River Basin which traditionally experience longer fire-free intervals (Gavin et al. 2006) (Fig. 37).

The relationship between the moving variance of $\delta^{18}O$ and CHAR deteriorates after 1910 (Fig. 43), demonstrating the effect of Euro-American land use practices on fire-climate relationships in the region (Hessburg et al. 2021, Walsh et al. 2018). Humans have played a major role in shaping fire regimes in the Columbia River Basin for thousands of years, through deliberate burning practices (Boyd et al. 1999, Walsh et al. 2018, Walsh et al. 2023). The Interior Salish people, who lived in the study region, used fire to enhance valued plant resources, facilitate travel, and hunt game (Wynecoop et al. 2019). Castor and Fish lakes show decreasing CHAR during the 19th century, coincident with the arrival of smallpox in Upper Columbia River Basin (Boyd 1998) (Fig. 37). By the mid-1850s, Euro-American settlement and loss of Native American burning practices Round, Castor, and Fish Lakes all show low CHAR (Fig. 37). Traditional land management practices were replaced by intensive agriculture and forestry after the late 19th century (Hessburg and Agee 2003, Hessburg et al. 2005). Fire suppression efforts starting in the early 20th century drastically lengthened the period between fires in dry forests that traditionally experienced frequent burning (Hessburg and Agee 2003). At Castor and Round, CHAR remained low until the mid-20th century when lake sediment, tree-ring records, and meteorological show an intense drought (Fig. 35, Fig. 37), which would have diminished the effectiveness of fire suppression tactics (Westerling and Swetnam 2003). At Castor Lake, charcoal accumulation declines again after this peak, possibly reflecting improved fire-fighting technology and training, and increased investment in fire prevention after of World War II (Pyne 2010; Dombeck et al. 2004).

4.4.2 Hydroclimate variability in western North America

Low $\delta^{18}O$ values during the MCA, indicating relatively high cool-season precipitation, are consistent with predominantly PDO/IPO negative conditions (e.g., wetter winters in northwestern

North America), consistent with a PDO reconstruction from two long lived tree-ring chronologies in southern California and Alberta (MacDonald and Case, 2005). Tree-ring based April 1 SWE reconstructions from the Upper Colorado River Basin do not extend into the MCA (Pederson et al. 2011); however, those from the southern Colorado River basin indicate drier conditions during the MCA than the LIA, reflecting the north-south dipole pattern in ENSO/PDO induced precipitation anomalies (Sung et al. 2014, Pederson et al. 2011). Pollen-derived temperature reconstructions from North America show moderately warmer conditions during the MCA, but such claims can only be made with low confidence (Viau et al. 2012, Trouet et al. 2013). In all, however, a coherent picture of hydroclimate variability in western North America over the past 1200 years is difficult to derive from the existing proxy data, with few records showing significant correlations with one another (Fig. 44, Table 4).

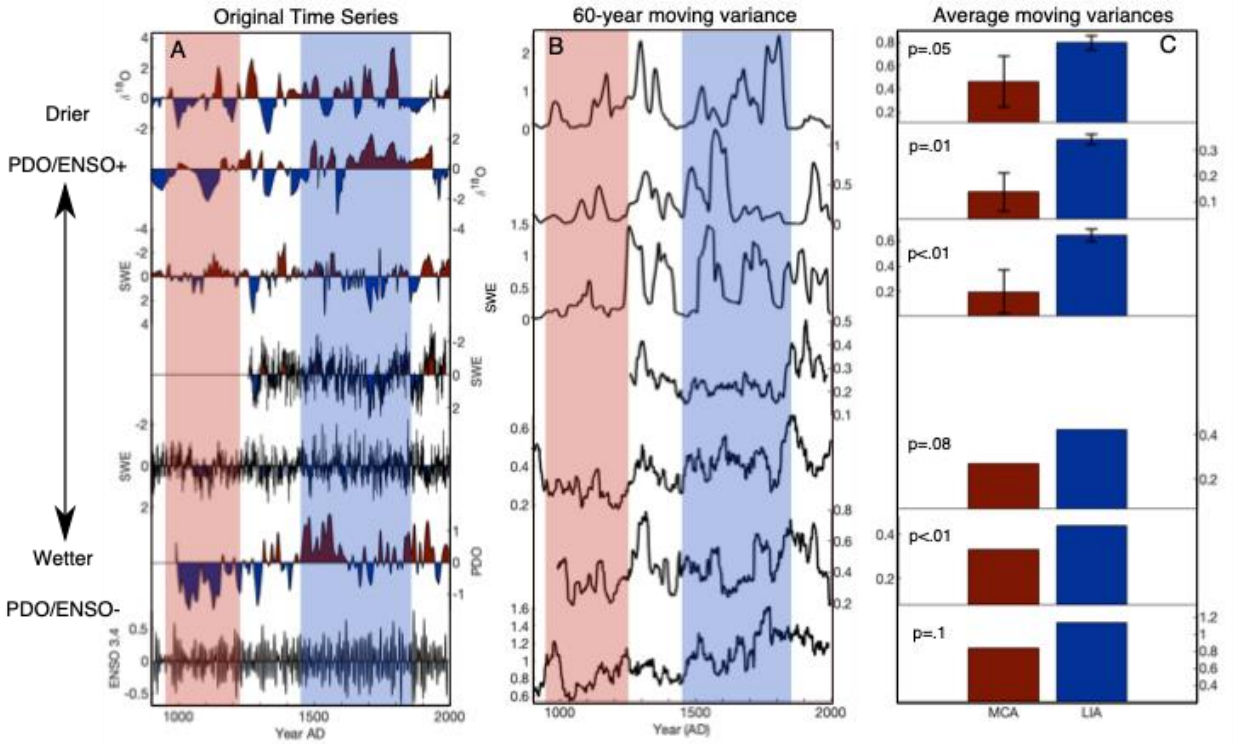

Figure 44. Last millennium hydroclimate of western North America proxy records. (A) Round and Castor lakes $\delta^{18}O$ records (this study), Foy Lake, MT (Schoennemann et al. 2020), Upper Columbia River Basin and Southern Upper Colorado SWE reconstructions (Pederson et al. 2011), Western North America tree-ring based PDO reconstruction (Macdonald and Case, 2005), North American tree-ring ENSO reconstruction (Li et al. 2011) (all

treated with 20-year smoothing. (B) 60-year moving variances of the same proxies. Red and blue shading indicates the MCA (900-1250 CE) and LIA (1450-1850 CE), respectively. (C) Average 60 year moving variance for each proxy record. P values indicate results of 2 sample Kolmogorov-Smirnov tests Error bars on lake sediment records represent 97.5-2.5 percentile age model uncertainty (Castor and Round Lake) and proxy uncertainty (Foy Lake).

Table 4. Pearson's correlation coefficients between different high-resolution proxy records from Fig. 44. Green cells indicate relationships that are significant ($p<0.1$) after accounting for autocorrelation.

	Round	Castor	Foy	UCRB	S Co	MacDonald	Li	Law Dome	Buckley
Round									
Castor	0.22								
Foy	-0.08	-0.1							
UCRB	-0.02	0	0.04						
S Co	-0.11	-0.04	0	-0.15					
MacDonald	-0.05	0.16	-0.05	-0.23	0.2				
Li	0	-0.02	-0.01	-0.03	0.46	0.09			
Law Dome	-0.2	0.01	0.01	-0.17	0.08	0.05	0.02		
Buckley	0.13	0.21	-0.19	-0.05	0.29	0.08	-0.02	0.26	

A consistent feature of high-resolution North American hydroclimate reconstructions, however, is enhanced multi-decadal variability during the LIA compared to the MCA (Fig. 44b, 42c). Snowpack reconstructions from lake sediments (Foy Lake, Schoenemann et al. 2020) and tree-rings (Pederson et al. 2011) all document comparatively high-amplitude wet/dry cycles during the LIA. A North American tree-ring derived ENSO reconstruction previously noted enhanced multidecadal variability during the latter half of the millennium, driven by tropical Pacific forcing (Li et al. 2011, Fig. 44). A prominent shift to more variable conditions in the eastern tropical Pacific during the middle of the last millennium is well documented (Rustic et al. 2015) and is consistent with higher amplitude wet/dry cycles in the western United States. Additionally, the LIA was marked by increased strength in the teleconnection between the tropical Pacific and precipitation in western North America (Dee et al. 2020). The influence of tropical Pacific conditions on winter storm tracks in North America may also explain why high-resolution records of hydroclimate phenomena show enhanced variability during the LIA while centennial-scale proxy compilations derived from pollen records fail to capture distinct transitions between the MCA and LIA (Shuman et al. 2018, Viau et al. 2012).

4.5 Conclusions

High-resolution $\delta^{18}O$ data from Castor and Round lakes show strong similarities to cool-season sensitive tree-ring proxies and winter precipitation data, consistent with modelling studies (Steinman et al. 2010a and b). Applying a 20-year lowpass filter to tree-ring width records greatly improved correlations between the two proxy types, as the residence time of lake water acts to buffer the isotopic response of carbonate sediments to interannual climate variability. Additionally, detrending the $\delta^{18}O$ datasets improves correlations with tree-ring data, as removal of age-related growth trends suppresses low-frequency signals in tree-ring records. The improvement in the comparison of lake and tree-ring records of understanding seasonal biases and temporal sensitivities of different proxy archives.

Castor and Round lakes $\delta^{18}O$ records indicate drier winter conditions during the LIA than the MCA. While other high-resolution proxy records from western North America do not show consistent trends in mean-state hydroclimate conditions, an increase in multi-decadal (~60-year) variability during the LIA is consistent throughout the region. Records from the Upper Columbia River Basin also document an increase in fire activity coincident with enhanced multi-decadal precipitation variability. Increased hydroclimate variability leads to fuel accumulation during wet periods, followed by widespread burning during droughts. However, the arrival of disease and Euro-American land use practices altered previously existing human-fire-climate relationships in the region. The paired use of hydroclimate and fire proxies from the same sedimentary sequence allows for thorough quantitative interrogation of the influence of hydroclimate on biomass burning.

5.0 The influence of multidecadal climate variability and abrupt landscape change on terrestrial ecosystem composition and fire regime in the semi-arid Upper Columbia River Basin

High resolution paleoclimate and ecological proxy datasets from the same lacustrine sedimentary sequence from eastern Washington helps elucidate Holocene environmental dynamics. Round Lake sits near the ecotone between sagebrush steppe and dry pine forest, making the surrounding landscape sensitive to changes in precipitation-evaporation (P-E) balance. During the early Holocene, when summer insolation was significantly higher than at present Round Lake, arid conditions prevailed. Prolonged drought led to less arboreal vegetation, and may have limited fuel accumulation leading to low biomass burning. Sub-centennial hydroclimate variability associated with the Pacific Decadal Oscillation (PDO) is very muted during this period as well. The deposition of the Mazama tephra (~7600 yr BP) in the watershed caused a rapid shift to increased *Artemisia* on the landscape. While winter precipitation was higher during this period, owing to an overall La Niña/PDO- like mean state, elevated *Artemisia* pollen percentages persist for several millennia. Tephra-driven changes in soil characteristics related to weathering of the silica-rich ash led to higher rates of evaporation, increased biomass burning, and enhanced multidecadal hydroclimate variability may have acted simultaneously to delay the re-establishment of *Pinus* and *Pseudotsuga*, even when background climatic conditions favored their growth. Additionally, while isotopic evidence indicates wetter conditions during the middle Holocene, physical stratigraphy and biomass burning proxies indicate lower lake levels prior to 5kyr BP, suggesting that the middle Holocene was marked by enhanced seasonality. The late Holocene is marked by comparatively large swings in multidecadal precipitation, peaking during the last

millennium and possibly related to the amplitude of the El Niño Southern Oscillation. Isotopic correlations with arboreal pollen improve markedly when 60-100 years of antecedent climate proxy data are incorporated. No such pattern exists with *Artemisia* and *Poaceae* indicating that vegetation-climate disequilibria is a persistent feature of slow-growing arboreal species but not with herbaceous vegetation which responds more quickly to ambient hydroclimate conditions. These findings highlight the importance of climate-ecosystem interactions which operate at multidecadal frequencies and which are difficult to discern without the use of high-resolution multiproxy perspectives.

5.1 Introduction

Water stress and wildfire activity in semi-arid western North America have begun to surpass 20th century maxima (Higuera et al. 2021). Thus, any empirical understanding of climate-ecosystem variability under drought extremes resembling those projected over the next century must rely on paleoclimate proxy data from arid periods of the past. Lake sediments offer a particularly useful avenue for exploration, as they archive multiple physical, chemical, and biological proxies which are sensitive to different aspects of the Earth system. Oxygen isotopes from authigenic carbonate minerals (Nelson et al. 2011), pollen (Whitlock and Bartlein 1997), and sedimentary facies (Shuman et al. 2009a) have all provided valuable insight into environmental conditions in northwestern North America (PNW) during times when orbital parameters, glacial extent, and greenhouse gas concentrations differed from those of the modern era. These sources provide valuable context to our understanding of modern environmental change; oxygen isotopes

suggest the early Holocene was marked by extensive and continuous drought conditions exceeding modern moisture deficits in both length and severity (Lehmann et al. 2021). Long-term ecological data from charcoal and pollen data suggest Euro-American land use and fire suppression policies during the past century have led to a modern "fire deficit", complicating our understanding of climate-fire interactions (Marlon et al. 2012, Walsh et al. 2015). Unfortunately, the greater temporal coverage gained by using lake sediments often comes at the expense of temporal resolution, with most studies lacking the sampling frequency to resolve shifts in important climate systems such as the El Niño Southern Oscillation (ENSO) and Pacific Decadal Oscillation (PDO). As these systems exert influence on water balance (McAfee and Wise 2016), moisture delivery pathways (Wise and Dannenberg 2017), and fire activity (Heyerdahl et al. 2008) in northwestern North America, developing paired high-resolution paleoclimate and paleoecological records is crucial to a process-based understanding of climate-vegetation-fire relationships.

5.1.1 Holocene-scale moisture balance in the PNW

Paleoclimate records from the Pacific Northwest tend to indicate warm and dry conditions prevailing after the end of the Pleistocene (approximately 11.7 kyr BP-8.2 kyr BP, Lehmann et al. 2021, Galloway et al. 2011, Shuman et al. 2009a). Elevated summer insolation has long been invoked to explain early Holocene aridity and associated ecological change (Millspaugh et al. 2000, Brunelle and Whitlock 2003). During the middle Holocene, oxygen isotope based sedimentary records indicate wetter than present conditions in northwestern North America between approximately 7500-2500 BP, while reconstructions from other archive types indicate the opposite pattern (Steinman et al. 2016). These differences have been attributed to conflicting seasonal sensitivities between proxy types, with the middle Holocene potentially marked by wetter

winters and drier summers. Hydrological modeling results indicate the oxygen isotope composition of carbonates from the northwest primarily reflects the isotopic composition of cool-season precipitation (Steinman and Abbott 2013, Steinman et al. 2016), given the winter-dominance of precipitation seasonality and negligible evapotranspiration during cool-seasons. Other proxy types (namely lake level reconstructions, pollen spectra, and chironomid assemblages) are more sensitive to year-round conditions and indicate drier conditions between 7500-2500 BP, owing to enhanced warm-season insolation and an enhanced North Pacific blocking high pressure system (Bartlein et al. 2014). From roughly 6000 BP to present, winter sensitive records generally display a drying trend (Steinman et al. 2016), with increasingly severe wet/dry cycles superimposed over this low-frequency pattern (Nelson et al. 2011).

5.1.2 The role of multidecadal climate variability in the PNW

Prominent high-frequency variability (interannual to decadal shifts in climate patterns, not necessarily associated with long term mean-state shifts) apparent in many paleorecords is often attributed to the El Niño Southern Oscillation (ENSO) (Nelson et al. 2011) and the Pacific Decadal Oscillation (PDO) (Kirby et al. 2010, Stone and Fritz 2006). Positive ENSO (El Niño) and PDO phases are associated with a strengthened Aleutian Low pressure system which deflects storm tracks south, causing drier than average conditions throughout the northwest (McAfee and Wise 2016). The opposite conditions hold true during La Niña/PDO- phases (Fig. 45). This produces a north-south dipole pattern in moisture anomalies in western North America centered at approximately 40°N (Wise 2010, Sung et al. 2014, Fig. 45A, Fig. 45B). Many records indicate a severe reduction of ENSO variance (Tudhope et al. 2001, Carre et al. 2021) or predominantly La Niña like conditions (Mark et al. 2022, Conroy et al. 2008, Thompson et al. 2017) during the

middle Holocene. Long-term shifts in the tropical Pacific mean-state and ENSO are at least partially related to changing orbital configuration (Carre et al. 2021). However, intense centennial-millennial scale variability that cannot be explained through insolation alone (Emile-Geay et al. 2016) is a prominent feature of many reconstructions (Cobb et al. 2013).

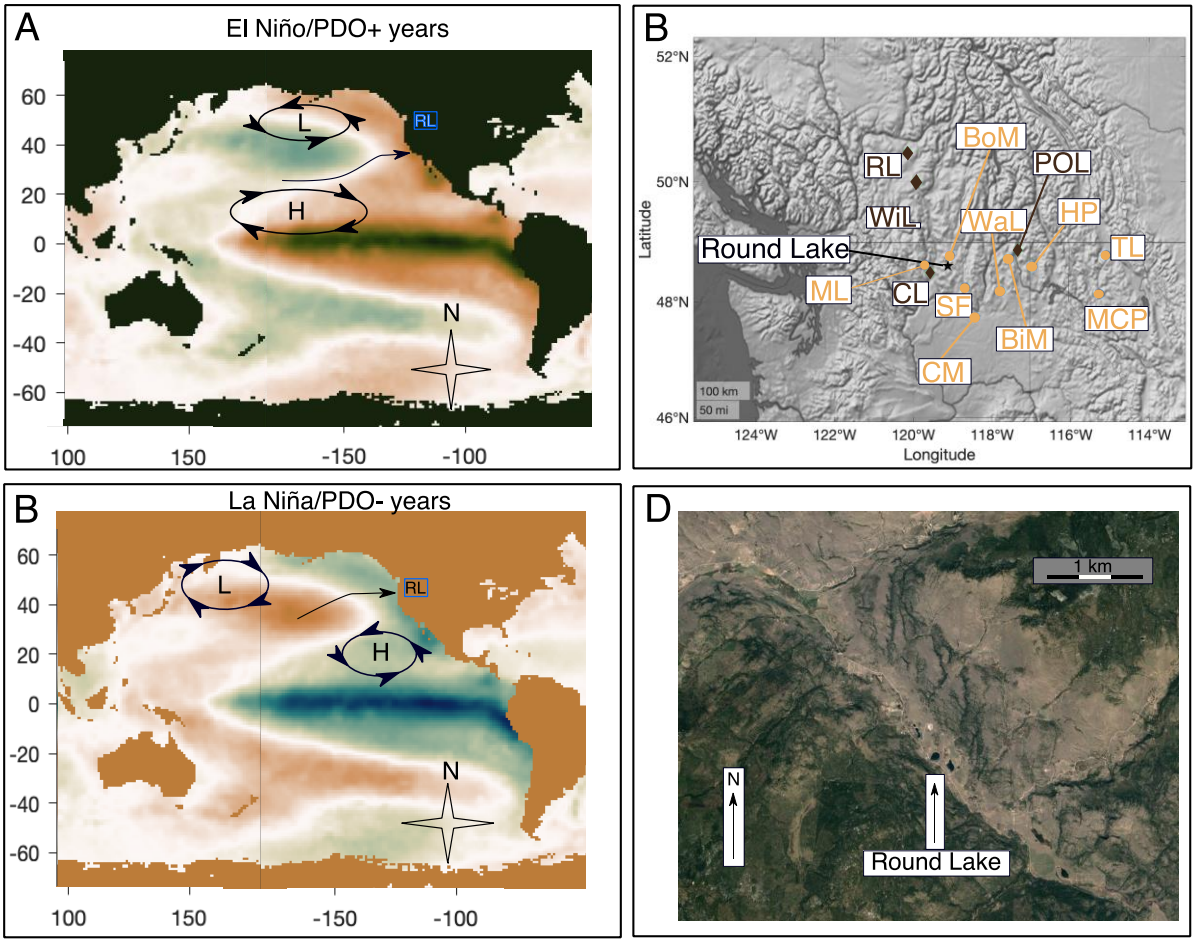

Figure 45. Study area and setting. (A) The impact of El Niño/PDO+ conditions on prevailing pressure systems (circular arrows) and stormtracks (black arrows) in the mid-latitude eastern Pacific. Study site (Round Lake) represented in blue circle. (B) Same as in (A) but for La Niña/PDO- conditions. (C) Location of different proxy sites discussed in the text. Orange circles represent pollen sites from Fig. 8, from E to W: TL=Tepee Lake MCP=McKillop Creek Pond HP=Hagar Pond BiM=Big Meadows WaL=Waits Lake CM=Creston Mire BoM=Bonaparte Meadows ML=Mud Lake. Maroon diamonds indicate other reconstructions plotted in Fig. 7, from E to W: POL=PO Lime Lake CL=Castor Lake WiL=Windy Lake RL=Roche Lake. Round Lake is the black star. (D) Aerial image of the Round Lake watershed.

The Holocene-scale evolution of the PDO (or Pacific Multidecadal Variability, which does not imply a clear oscillatory component) is very poorly constrained. Tree-ring based proxies from the last millennium indicate considerable shifts in multidecadal hydroclimate variability (Wise and Dannenberg 2014, Macdonald and Case 2005, D'Arrigo et al. 2001), but few longer records have sufficient temporal resolution and span to address the persistence and magnitude of PDO-scale climate variability throughout the Holocene (Stone and Fritz 2006, Kirby et al. 2010). The degree to which mid-latitude multidecadal phenomena are intrinsic to the climate system—and the degree to which they are driven by external forcing mechanisms such as periodic volcanic eruptions and anthropogenic aerosol emissions (Mann et al. 2021, Sun et al. 2022)—remains unclear, owing in part to a lack of proxy records well-suited to answering this question. Marine sediments from the North Pacific seemingly reflect a La Niña/PDO- mean state between 8000-4000 yr BP (Barron and Anderson 2011). This pattern would theoretically help explain wetter winter conditions seen in northwestern proxy reconstructions between 6-4 kyr BP (Lehmann et al. 2021, Steinman et al. 2016). Whether or not this period was marked by significant multidecadal variability superimposed skewed towards a more La Niña/PDO- background state, or simply multi-millennial scale quiescence which resembles a modern La Niña/PDO- configuration, is not clear.

5.1.3 The impact of high-frequency climate variability on ecosystems

Different modes of climate variability, operating over nested and overlapping timescales, influence the composition of ecological communities. For example, while long-term warming trends during the last deglaciation allowed for the gradual expansion of forests in previously glaciated regions (Adam et al. 2021), abrupt changes in temperature and precipitation patterns can

elicit comparatively rapid vegetation responses (Shuman et al. 2009b). Quasi-periodic phenomena such as the PDO, superimposed over drifting climatic background states as well as abrupt changes, play an important role in modulating terrestrial vegetation. Pulses of tree recruitment in the semi-arid western United States have been tied to the onset of multidecadal periods of above average moisture balance (Gray al. 2006). Given that the nature of such variability has recently been called into question (Mann et al. 2020, Mann et al. 2021), and given the lack of existing proxy records well-suited to addressing such questions, it is not clear whether similar climate-vegetation relationships have been significant in structuring terrestrial ecosystems over the Holocene.

Biomass burning in the eastern Cascades has also been linked to ENSO and the PDO (Heyerdahl et al. 2008) with particularly intense fire seasons generally occurring during PDO/ENSO positive conditions. The cyclic nature of these shifts in P-E balance, rather than just fire season moisture deficits, are important to fire dynamics in semi-arid regions. Wet periods foster fine fuel production and connectivity, followed by widespread desiccation and burning during subsequent droughts (Walsh et al. 2015, Brunelle 2022, Cooper et al. 2022). Understanding how high-frequency climate signals, which play out over low-frequency background trends, influence ecosystem dynamics is crucial to future management concerns. Unfortunately, climate-ecosystem coevolution at the multidecadal scale exists at too low a frequency to be discerned from direct observation and at too high a frequency (and with too many variables) to be quantitatively discerned from existing paleolimnological data. While recent work has called attention to relatively short-term (50-200 year) climate-vegetation relationships (Williams et al. 2021, Svenning and Sandel 2013), paired proxy studies which investigate terrestrial vegetation change in the context of independent hydroclimate reconstructions from the same site are lacking.

5.1.4 Problems and approach

Our existing knowledge of climate-ecosystem variability in western North America is hindered by short records from observational datasets and tree-ring chronologies on one hand, and by the generally low temporal resolution of long-term sedimentary records without paired hydroclimate-ecological proxies on the other. For example, fire years during the past century tend to be more extreme during intense summer droughts. Does this relationship hold true during the early Holocene, when other sites in the region record long-term aridity which may have suppressed the accumulation of fine fuels? Similarly, ENSO and the PDO have been shown to vary widely over the past millennium--are these high-frequency climate phenomena still important influences on water balance during different climatic background states? Here, we use multiple perspectives to inform one another and present a high-resolution multi-proxy dataset from Round Lake, eastern Washington (Fig. 46). The oxygen and carbon isotope data presented are of particularly high resolution for Holocene-scale records (median age-step=4.5 years) and can be quantitatively compared to stratigraphy, organic carbon isotopic ratios, and most crucially, charcoal and pollen data taken the same core. This approach eliminates relative age-uncertainty and helps disentangle the complex influence of interannual, decadal, centennial, and millennial-scale climate dynamics on terrestrial ecosystems.

5.2 Methods

5.2.1 Study site

Round Lake (48.61 N 119.12 W; 654 m a.s.l.) is a small (surface area ~.07 km^2) lake formed in a dead ice depression during the recession of the Okanogan Lobe of the Cordilleran Ice Sheet (Koyanen and Slaymaker 2004). The lake floor is generally flat, with a maximum depth of approximately 12m on the eastern half of the lake. The surficial geology is calcium rich quaternary glacial drift and sits within the Lime Belt of eastern Washington (Oroville Quadrangle, Fox 1970). The southwest facing slope of the watershed is largely devoid of arboreal vegetation, while the northeast facing slope is primarily comprised of *pinus ponderosa* forest (Fig. 46D), an aspect-driven pattern previously noted in the region (Walsh et al. 2015). Fire return intervals prior to the imposition of Euro-American land use practices were sub-decadal (Everett et al. 2000) and the combination of fire exclusion and cattle grazing has led to canopy closure and a decline in biomass burning (Walsh et al. 2015).

Round Lake receives an annual average of approximately 330 mm of precipitation, which primarily falls during the cool season. Between November and March, the Aleutian Low strengthens and moves southward, bringing moisture from the Pacific Ocean inland via the mid-latitude westerly winds (Rodinov 2007). These patterns are modulated by ENSO and the PDO. During El Niño/PDO+ conditions, the average position of Pacific storm tracks moves south (Wise and Dannenberg 2017) and drier conditions generally prevail in the Northwest. The opposite pattern generally holds during La Niña/PDO- conditions.

5.2.2 Sample collection

Surface water samples from Round Lake were collected in 2003, 2006, 2007, 2008, 2009, 2011, 2016, 2017, and 2018. Cores from Round Lake were collected in August 2017 and February 2018 in 12 meters of water, using a Livingstone piston corer (Wright et al. 1984) and a freeze corer (Besonen et al. 2008, Mark et al. 2023). The uppermost 454 centimeters of the sedimentary sequence were captured with 50cm overlapping drives. Beneath this horizon, the use of external casing, which necessitated the repeated use of the same drill hole, prevented the collection of overlapping material. All cores were transported to the University of Pittsburgh sedimentology laboratory. Surface sediments were collected in February 2018 and analyzed at a higher resolution, and were subsequently spliced to the remainder of the core (see Chapter 4).

5.2.3 Imagine and physical sedimentology

Cores were imaged using a GeoTek line scanning camera and aligned according to the laminated visible stratigraphy. 1 cm^3 volumetric samples were taken at 1cm resolution down the entirety of the sedimentary sequence and weighed, dried, and re-weighed to calculate bulk density. The remainder of the sample was then combusted at 550C and re-weighed to determine organic content, then re-combusted at 1000C and weighed a third time to determine carbonate content and residual mineral material (Heiri, 2001).

5.2.4 Chronological control

An age model for the full sedimentary sequence was developed using a combination of ^{137}Cs, ^{14}C, and tephrachronology. The uppermost 20cm was analyzed at .5cm resolution on a Canberra BE-3825 Germanium Detector at the University of Pittsburgh and yielded two ^{137}Cs dates corresponding to the onset of nuclear weapons testing (Foucher et al. 2021). Charcoal and seeds were selected from disaggregated sediments using a paintbrush under 3-10x magnification and treated using a standard acid-base-acid pretreatment (Santos et al. 2014) for ^{14}C dating. The samples were subsequently combusted and graphitized at the University of California-Irving W.M Keck Carbon Cycle Accelerator Mass Spectrometer on a National Electrostatics Corporation 500kV 1.5SDH-1 Compact AMS device. The 6730+-40 ^{14}C yr Mazama tephra is well documented throughout western North America. This tephra layer is prominent in the Round Lake sedimentary record, represented by a ~60 cm ash deposit. The 60cm of tephra were subtracted from the overall depth of the sedimentary record when constructing the final age model. Individual age control points were converted into an age-depth model with quantified uncertainty using the BChron program in R (Parnell et al. 2014). All ^{14}C dates were calibrated using the IntCal20 calibration curve (Reimer et al. 2020).

5.2.5 Isotopic analysis

Surface water isotopes were measured for $\delta^{2}H_{water}$ and $\delta^{18}O_{water}$ at Indiana University Purdue University Indianapolis using a Picarro L2130-I Analyzer. Volumetric sedimentary samples of 1 cm^3 were collected every half centimeter for the entirety of the core, excepting the top 60cm where they were sampled with a razor blade at the finest possible resolution according

to the visual stratigraphy of the freeze cores (see Mark et al. 2023 for a full description). Samples were disaggregated in a solution of 7% H_2O_2 to remove the labile organic fraction and sieved through a 63-μm mesh screen to remove any remaining coarse mineral fraction and isolate the $CaCO_3$. The remaining fine fraction was treated with 3% NaClO, and was then rinsed, lyophilized, and homogenized (Nelson et al. 2011). Prepared samples were sent to the University of Arizona Environmental Isotope Laboratory. $\delta^{18}O_{carb}$ and $\delta^{13}C_{carb}$ measurements were conducted on a Finnigan MAT 252 gas ratio mass spectrometer and are presented in standard δ-notation.

Total organic carbon:total Nitrogen (TOC:TN) ratios and carbon isotopic analysis of organic material was conducted by lyophilizing and homogenizing 1 cm^3 samples at down core. Homogenized samples were then weighed and placed in silver capsules. To remove carbonate without preferentially dissolving labile organic material, samples were vaporously acidified for 6 hours (Komada et al. 2008). Samples were then combusted and analyzed on a Thermo Scientific Delta V Advantage IRMS system at the University of Pittsburgh to determine $\delta^{13}C_{Organic}$.

5.2.6 Pollen and charcoal analysis

Volumetric 1 cm3 samples were taken at approximately 8cm intervals down the length of the core. Samples were counted at Montana State University according to standard methodology (Bennett and Willis, 2001). Volumetric 1 or 2 cm^3 charcoal samples were collected every 4cm for charcoal analysis and prepared according to the methodology of Whitlock and Larsen (2001). *Pinus, Picea, Pseudotsuga, Artemisia, Graminae,* and *Cyperaceae* records published by Mack et al. (1976, 1978a, b, c, 1979, 1983) were digitized and ^{14}C chronologies were recalibrated, with age depth models generated in the same manner previously described for Round Lake.

5.2.7 Mercury analysis

Mercury samples were taken at approximately 8cm resolution, lyophilized, homogenized and run on a DMA-80 Direct Mercury Analysis System.

5.2.8 Statistical analysis

Canonical correspondence analysis (CCA) was conducted in R using the package 'vegan' (Oksanen et al. 2013). The three sedimentary variables which explained the highest degree of inertia ($\delta^{13}C_{Organic,}$ $\delta^{13}C_{CaCO3}$, and % organic) were selected for CCA. As samples used to generate each proxy dataset derived from the same material, correlations in Fig. 6 were performed on real (non-interpolated) increments, eliminating relative age uncertainty. For comparison of antecedent climate conditions to pollen spectra, oxygen isotope samples were interpolated to constant ten-year increments to achieve consistency in the time domain (Fig. 61). Where appropriate, effective degrees of freedom were estimated when calculating correlations between time series' according to the formula (1+p)/(1-p) where p is the lag-1 autocorrelation (Steinman et al. 2016). Moving variances for Round Lake and Castor Lake (Lehmann et al. 2021) $\delta^{18}O$ records were calculated by interpolating samples to constant 8 year time steps (justified given the median temporal resolution of each proxy record) and calculating the variance in 9 sample (72 year) sliding windows. This interval was used to capture patterns multi-decadal variability described by Newman et al. (2016) and different intervals ranging from 56-96 years did not substantially alter patterns. Wavelet analyses were carried out on the same linearly interpolated dataset using the MATLAB code developed by Torrence and Compo (1998). Cross-wavelet analysis was carried out in MATLAB using the code developed by Grinsted et al. (2004).

5.3 Results

5.3.1 Sedimentary facies

Three distinct units in the Round Lake sedimentary sequence were delineated based on abrupt changes in mass accumulation rate of $CaCO_3$ (Fig. 46). The bottom unit (Unit I, 730-800 cm) of the Round Lake stratigraphic sequence consists of dense, banded packages of alternating dark organic-rich sediment and light-colored carbonate-rich sediments (Fig. 46). The middle unit (Unit II) is comprised of light colored banded and mottled carbonate rich (>30% $CaCO_3$) sediment. This unit is interrupted by an approximately 60cm Mazama tephra deposit between 606-666cm. Carbonate rich sediments continue immediately above the Mazama, with thick (10-20 cm-scale) calcareous bands interspersed with finer (mm-scale) laminations (Fig. 46). At 314 cm (4950 BP, 2σ 141 yr), there is an abrupt transition to dark colored finely laminated sediments which persist for the remainder of the core (Unit III). This unit remains relatively rich in $CaCO_3$, consisting of between 12% and 65% throughout. The sedimentation rate is highest in Unit II (approximately 0.4 cm/yr, Fig. 46). Both carbonate and organic mass accumulation rates are highest in this unit (Fig. 46). The percentage of organic matter is lowest in Unit II, indicating that the high sedimentation rate is primarily driven by drastically enhanced carbonate precipitation and preservation.

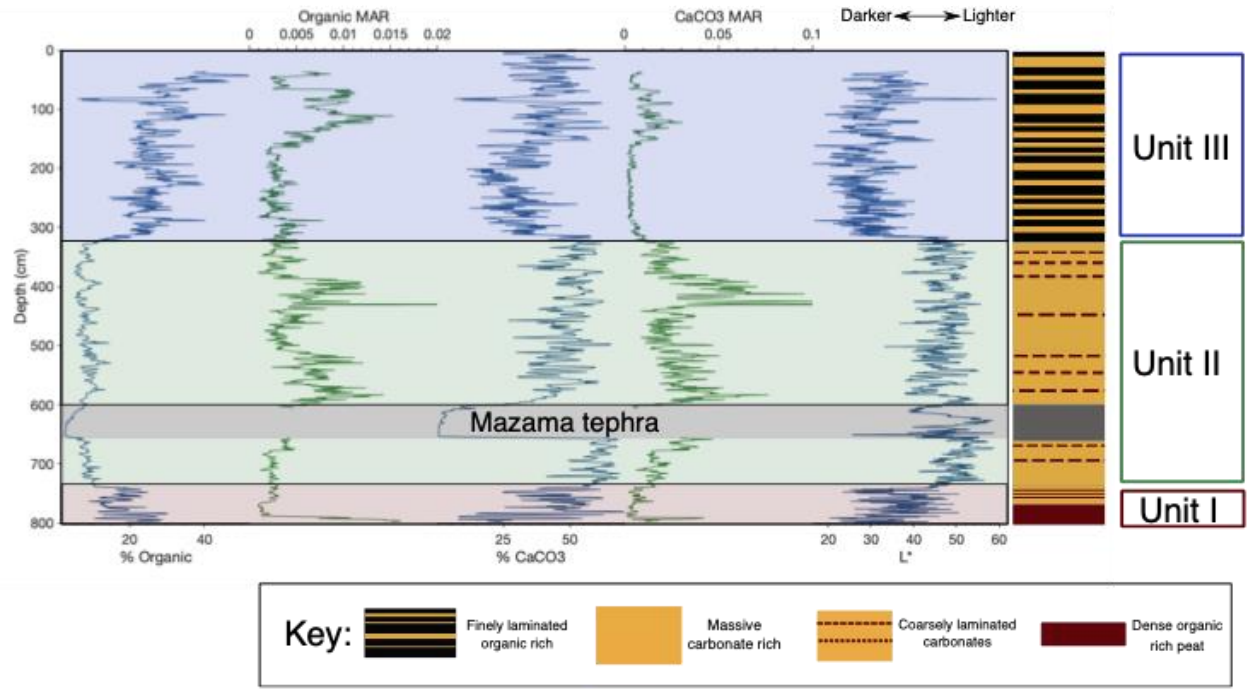

Figure 46. Physical sedimentology data for Round Lake A-17 and B-18. Calcium carbonate and organic content are represented both as percentages (blue lines) and mass accumulation rates (green lines). X axes for Organic and $CaCO_3$ MAR have been cut off to emphasize variability.

5.3.2 Carbon and oxygen isotopes

Water taken from Round Lake between 2006-2018 had $\delta^{18}O_{water}$ values which ranged between -6.9 and -11.2 ‰. Water is therefore evaporatively enriched with respect to local meteoric water (annual average of -12.9‰) and ground water (-15.8‰) by several per mille (Fig 36). $\delta^{18}O_{carb}$ values range between -14.01‰ and -8.30‰ over the course of the record. Unit I has the most enriched $\delta^{18}O_{carb}$ values, averaging -10.68‰. Unit II has the lowest overall mean $\delta^{18}O_{carb}$ of -11.41 ‰. More depleted $\delta^{18}O_{carb}$ values in this unit tend to correspond with darker, more organic rich sediments (Fig. 47). Unit III has a mean $\delta^{18}O_{carb}$ value of -11.27 ‰ (Fig. 48A). $\delta^{13}C$ values vary between -.79‰ and -6.78‰ and are significantly positively correlated with $\delta^{18}O$ (r=.53, p=<.01) throughout the entirety of the record (Fig. 48B), typical of evaporatively enriched water bodies (Li and Ku 1996).

Figure 47. Representative Unit II stratigraphy with oxygen isotopes overlain.

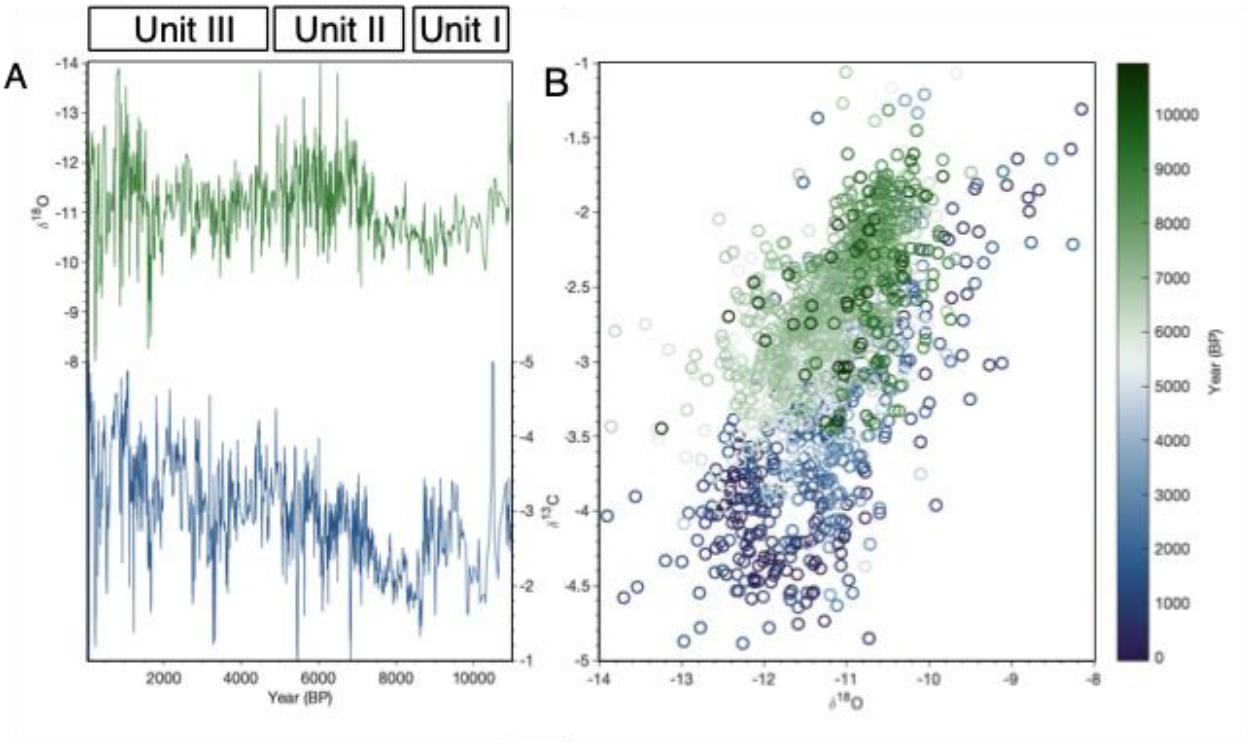

Figure 48. Carbonate isotopic results from Round Lake A-17 and Round Lake B-18. (A) 18O and 13C time series from 11 kyr BP-present. (B) Scatter plot of ^{18}O and ^{13}C. Color for each data point represents age BP (see color bar).

5.3.3 Organic matter isotope measurements of C and N

TOC/TN values and $\delta^{13}C_{Organic}$ indicate that organic matter in the sediment derives from a mix of lacustrine algae and terrestrial (primarily C4) vegetation (Fig. 49). TOC/TN values vary between 10-14 for the entirety of the record, and generally increase over the Holocene. During the early Holocene, $\delta^{13}C_{Organic}$ values are approximately -31‰ (Fig. 49). During the middle Holocene, $\delta^{13}C_{Organic}$ values reach their maximum point over the entirety of the record, approximately -27‰ at 6 kyr BP (Fig. 49). $\delta^{13}C_{Organic}$ ratios never approach values enriched enough (approximately -15 ‰) to indicate dominant C3 plant cover (Meyers and Lallier-Verges 2002). After the peak at 6 kyr BP, $\delta^{13}C_{Organic}$ declines to minimum values (-33‰) at approximately 4500 BP. Values then become increasingly variable and generally more enriched towards the modern portion of the core.

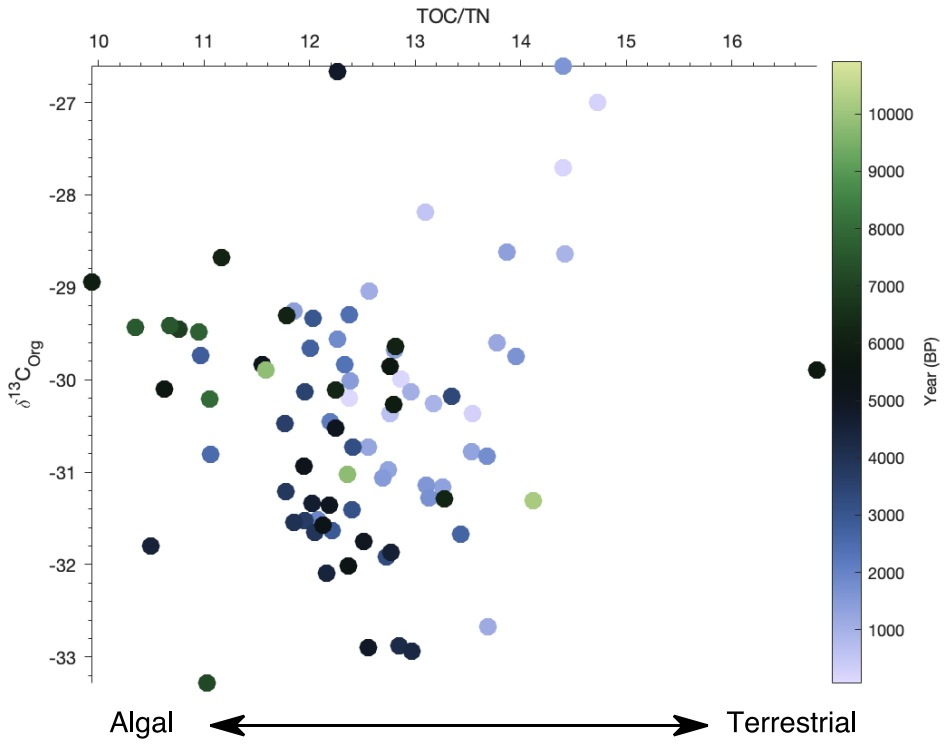

Figure 49. Scatter plot of organic 13C isotopes and TOC/TN. Representative elemental/carbon isotopic compositions from major contributing groups are represented in shaded regions. Color of each data point represents age BP (see color bar).

5.3.4 Pollen and charcoal

Dominant pollen types over the course of the Holocene include *pinus* (both *contorta* and undifferentiated varieties), as well as nonarboreal species *artemisia* and *poaceae* (Fig. 50). Non-arboreal species are generally high during the early Holocene. After the Mazama tephra deposition, *artemisia* pollen reaches its maximum level and remains elevated for several millennia (Fig. 50, Fig. X). *Pinus* pollen declines rapidly in the immediate aftermath of the Mazama tephra but then slowly increases until approximately 5 kyr BP, when *pinus* stabilizes and remains high for the duration of the Holocene (Fig. 50). Aquatic *myriophyllum* pollen appears abruptly in the record after 5 kyr BP and persists throughout Unit III (Fig. 50, Fig. 51). Charcoal accumulation rates are generally low during the early Holocene and increase markedly after the Mazama tephra,

remaining high for several thousand years and declining abruptly after 5kyr BP. This pattern is replicated in both micro-charcoal as well as in the larger <125 um fraction (Fig. 50, Fig. 56).

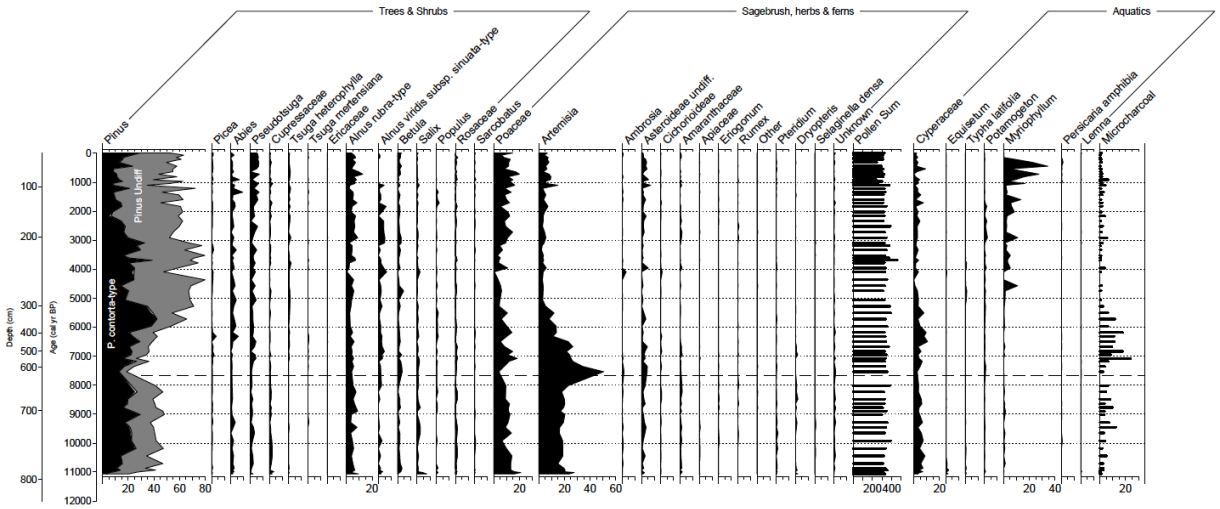

Figure 50. Round Lake pollen percentages and charcoal flux, plotted as both age (yr BP,interior y-axis) and depth (cm, exterior y axis). Dashed horizontal line represents Mazama ash layer.

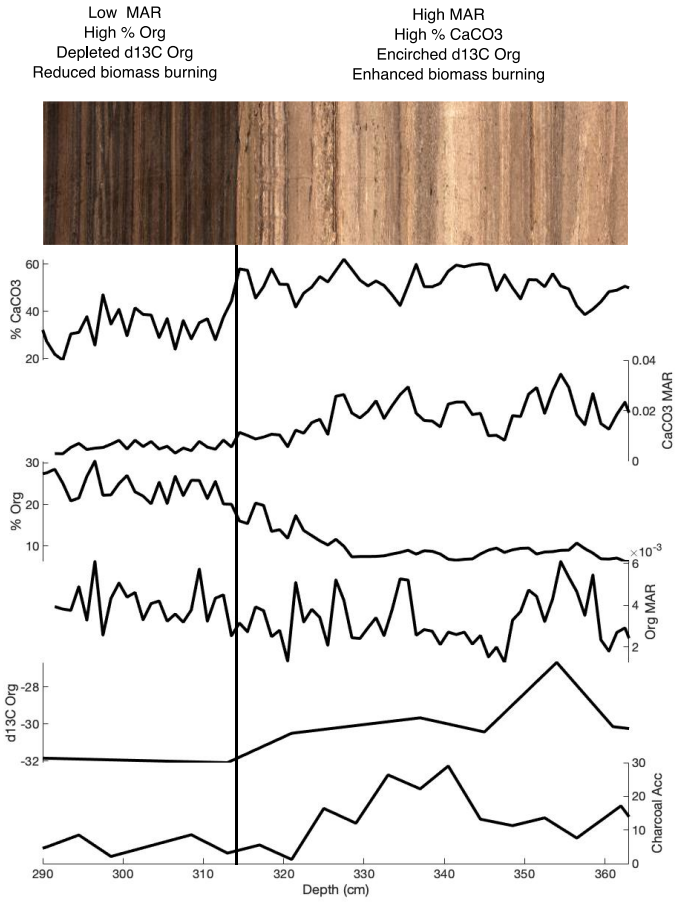

Figure 51. The abrupt transition between light colored carbonate rich sediments of the middle Holocene and dark, finely laminated sediments of the late Holocene, with several proxies across this boundary.

5.3.5 Mercury accumulation

Mercury accumulation rates are lowest during the early Holocene until the Mazama tephra layer. Values then increase to their pre-modern maximum at approximately 6 kyr BP and decline abruptly thereafter (Fig. 52, Fig. 53). Values increase very abruptly at 100 BP (CE 1850) to values approximately 50 times the Holocene average and remain elevated through the 20th century (Fig. 53).

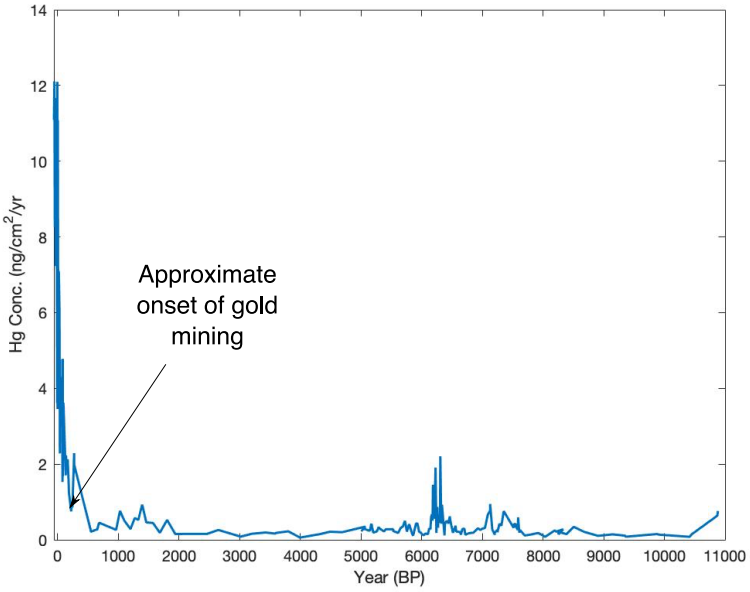

Figure 52. Full Holocene record of Round Lake mercury accumulation.

5.3.6 The relationship between climate and vegetation

Many sedimentary proxies show statistically significant relationships with pollen abundances (Fig. 53). Lower $\delta^{18}O_{carb}$ values, interpreted as primarily reflecting increased winter precipitation (Steinman and Abbott, Steinman et al. 2016, Mark et al. 2023), are associated with greater arboreal pollen (i.e. greater cool-season precipitation is associated with increased tree cover on the landscape). *Artemisia* and *poaceae* pollen, conversely, are significantly positively correlated with $\delta^{18}O_{carb}$. These values, however, do not meet the threshold for statistical significance ($p>0.1$).

Though $\delta^{13}C_{Carb}$ and $\delta^{18}O_{carb}$ are tightly coupled (Fig. 48B), pollen correlations are almost uniformly higher when compared to $\delta^{13}C_{Carb}$ (Fig. 53). Most studies of oxygen and carbon isotopes in lacustrine carbonates focus on oxygen isotopes (Horton et al. 2016). In closed or semi-closed systems like Round Lake, evaporation acts on both oxygen and carbon pools (Horton et al. 2016),

leading to covariance between the two (Li and Ku 1996). The comparatively small carbon pool may be disproportionately influenced by biological mediation which is primarily carried out during the warm season (Kelts and Hsu, 1978). The photosynthetic effect, which is most strongly expressed during the warm-season season, may then exert a comparatively large influence over the isotopic composition of both dissolved inorganic and organic carbon. Hence, carbon isotopes may reflect growth season conditions to a greater degree than the more winter-sensitive oxygen isotope signal and can therefore explain their more pronounced correlation to pollen species.

Greater organic content and darker color (here measured with L*, see Murton and Crowhurst 2020) are associated with the increase in arboreal pollen and decrease in herbaceous pollen seen in Unit III. The aquatic species *myriophyllum* appears at the transition between Units II and III and is thus negatively correlated with CaCO3 and positively correlated with both organic content and darker color (Fig. 53).

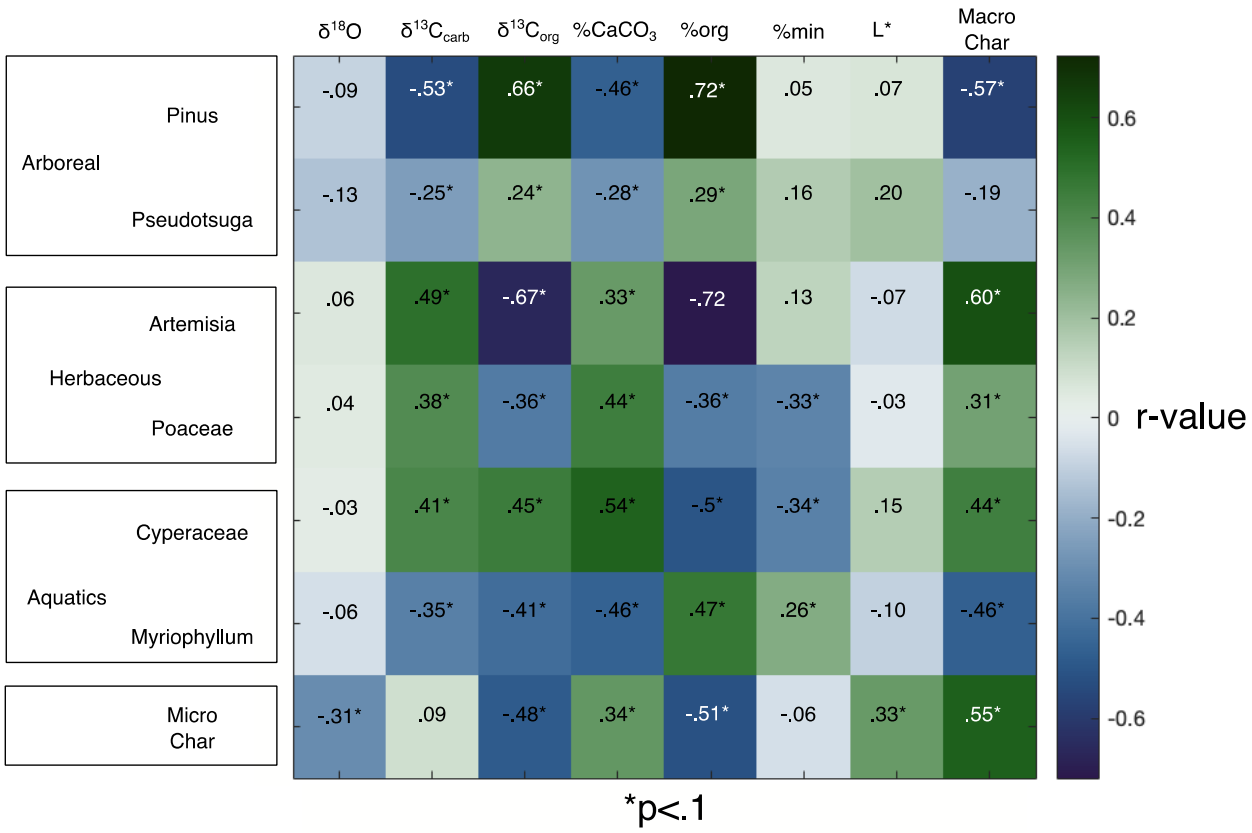

Figure 53. Correlation matrix of Round Lake multiproxy data and pollen counts. Shading of each box represents the r value. Number in each box represents the r value of each proxy combination.

5.4 Discussion

5.4.1 Unit I (11-8.5 kyr BP)

Physical stratigraphy, $\delta^{18}O_{carb}$, and pollen spectra all support the claim that the early Holocene was marked by prolonged aridity. Sedimentary facies of closed basin lakes reflect changes in lake level driven by shifting P-E balance (Schnurrenberger et al. 2003). Coarser

sediments reflect relatively shallower depositional environments, as increased energy is required to carry larger particle towards the center of the lake (Shuman et al. 2009a). Finely laminated sediments, conversely, indicate lower energy depositional settings of deeper waters relatively unaffected by wave energy or bioturbation. A coarse sandy layer between 793-795cm is perhaps the clearest stratigraphic indication of early Holocene lowstands (10931 BP 2σ 141 yr). The remainder of Unit III is marked by alternating dense, peat-like organic layers and more carbonate rich lithofacies. Oxygen isotopes in this unit are also enriched compared to the remainder of the core, suggesting reduced precipitation (Fig. 48, Fig. 54). Sites from east of the Cascade crest to the Northern Rocky Mountains all show elevated *artemisia* and *poaceae* and very low arboreal vegetation (Fig. 55), indicative of sagebrush steppe. These findings are consistent with a sediment core from nearby Castor Lake, which indicated prolonged drought throughout the early Holocene (Lehmann et al. 2021, Fig. 54). Elevated summer insolation promoted hot, evaporative summers, consistent with chironomid and diatom-based evidence from Southern British Columbia (Mushet et al. 2021, Chase et al. 2008, Fig. 54). Lower winter insolation (Fig. 54) also may have reduced the strength and altered the position of winter storm tracks (Bartlein et al. 2014).

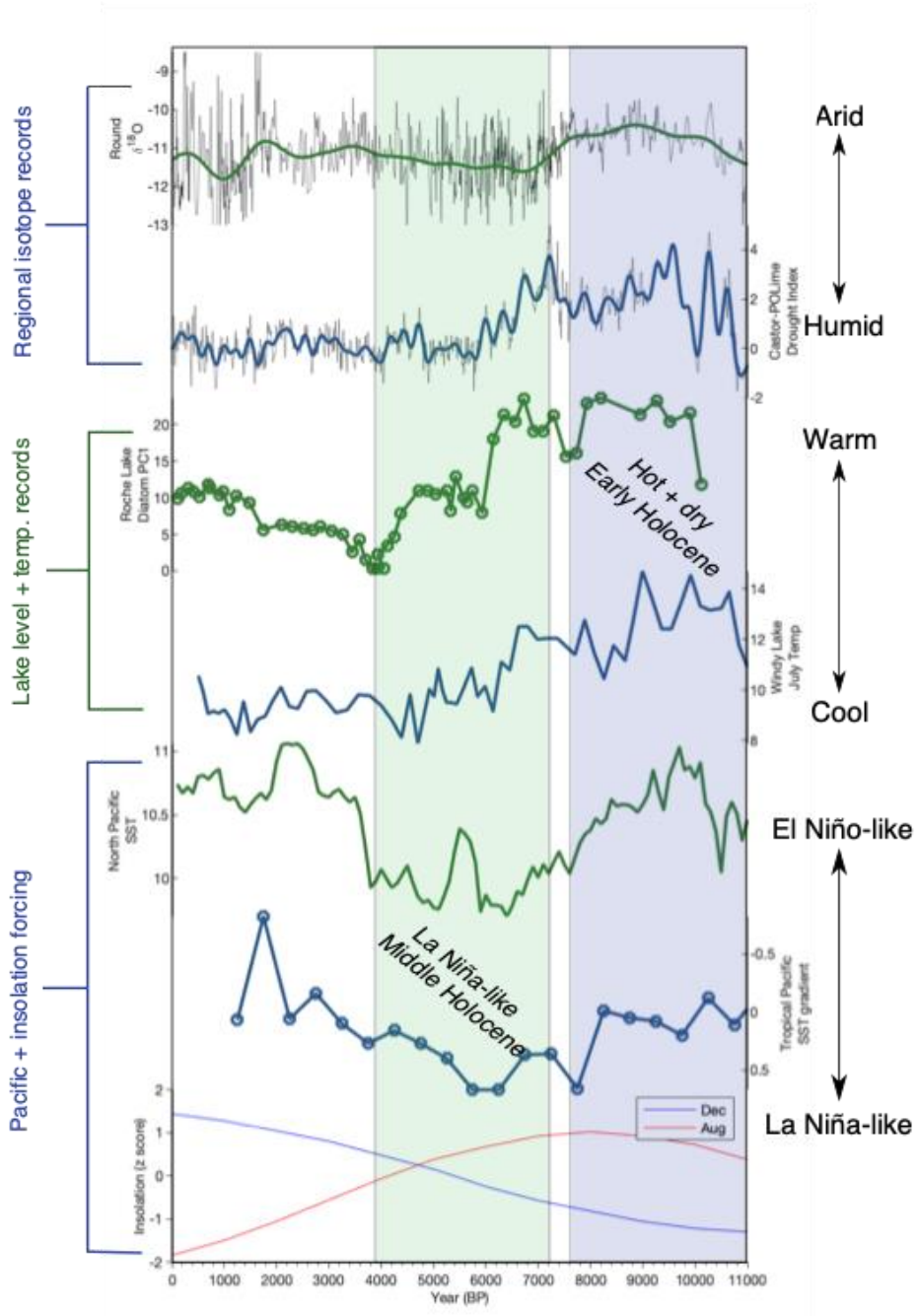

Figure 54. Summary of proxy reconstructions and potential forcing mechanisms. $\delta^{18}O$ Round Lake $\delta^{18}O$ reconstruction, Castor-PO Lime Lake drought index reconstruction (Lehmann et al. 2021), PC1 of diatom abundances indicating lake level history from Roche Lake (Mushet et al. 2022), Windy Lake chironomid based July temperature reconstruction (Chase et al. 2008), North Pacific sea-surface temperature reconstruction (Praetorius et al. 2020), east-west tropical SST gradient (Koutavas and Joanides, 2012) and Dec/Aug insolation anomalies.

The processes controlling fire in the Pacific Northwest during the early Holocene are overlapping and complex; the retreat of the Cordilleran Ice Sheet at the onset of the Holocene

drastically altered both landscape coverage (Whitlock et al. 1992) and atmospheric circulation patterns (Menounos et al. 2017). As the ice sheet retreated, previously glaciated landscapes were colonized by vegetation, and summer insolation maxima (peaking at approximately 10kyr BP) led to arid fire-season conditions (Fig. S5). As such, fire was relatively widespread in much of the PNW between 11-8 kyr BP (Walsh et al. 2015). At Round Lake, however, CHAR, micro-CHAR, and mercury accumulation are all relatively low over this period (Fig. S6). Unlike elsewhere in western North America where P-E balance was sufficient to foster greater biomass production, arid conditions surrounding Round Lake limited the production of fuel on the landscape. *Poaceae, artemisia,* and *asteroideae* are all comparatively high during the arid early Holocene (Fig. 5). The steppe-like landcover of this period would have prevented high-intensity, stand replacing fires common to more closed forests.

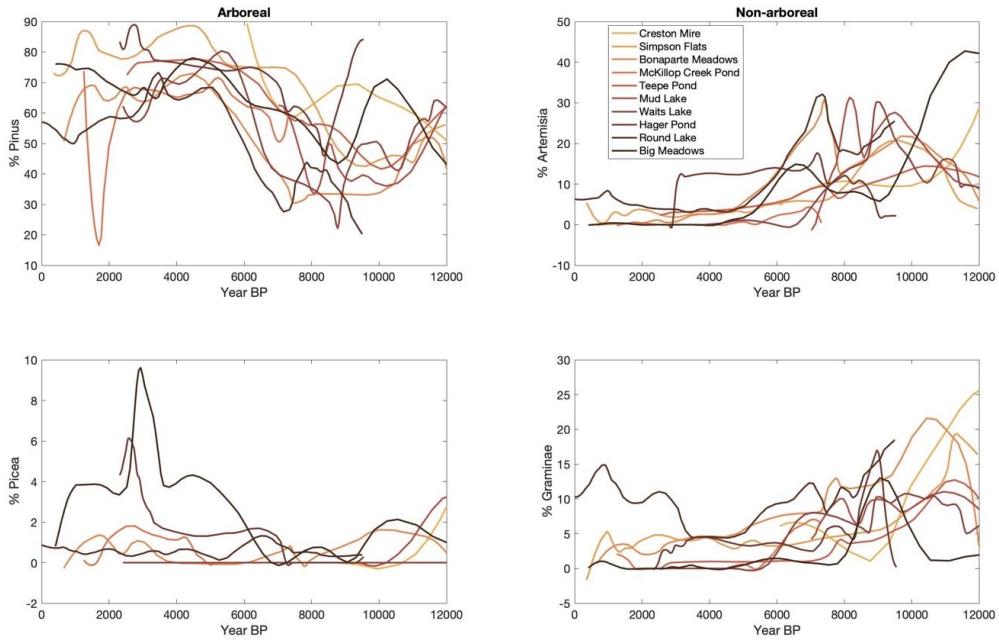

Figure 55. Pollen percentages of common arboreal and non-arboreal taxa from lakes in northwestern North America. Mud Lake (Mack et al. 1979), Round Lake (this study), Bonaparte Meadows (Mack et al. 1979), Simpson's Flats (Mack et al. 1978a), Creston Mire (Mack et al. 1976), Waits Lake (Mack et al. 1978b), Big Meadows (Mack et al. 1978c), Hager Pond (Mack et al. 1978c), McKillop Creek Pond (Mack et al. 1983), and Tepee Lake (Mack et al. 1983).

Reduced multidecadal hydroclimate variability during the early Holocene also may have muted regional fire activity (Fig. 56). Multidecadal periods of elevated moisture would have encouraged the growth and connectivity of fine fuels (and potentially suppressed biomass burning). This in turn would have led to widespread fire activity during subsequent droughts (Cooper et al. 2022, Brunelle et al. 2022). Climate was arid overall as well as *consistently* arid, preventing cyclic shifts in P-E balance from shaping fire ecology during the early Holocene.

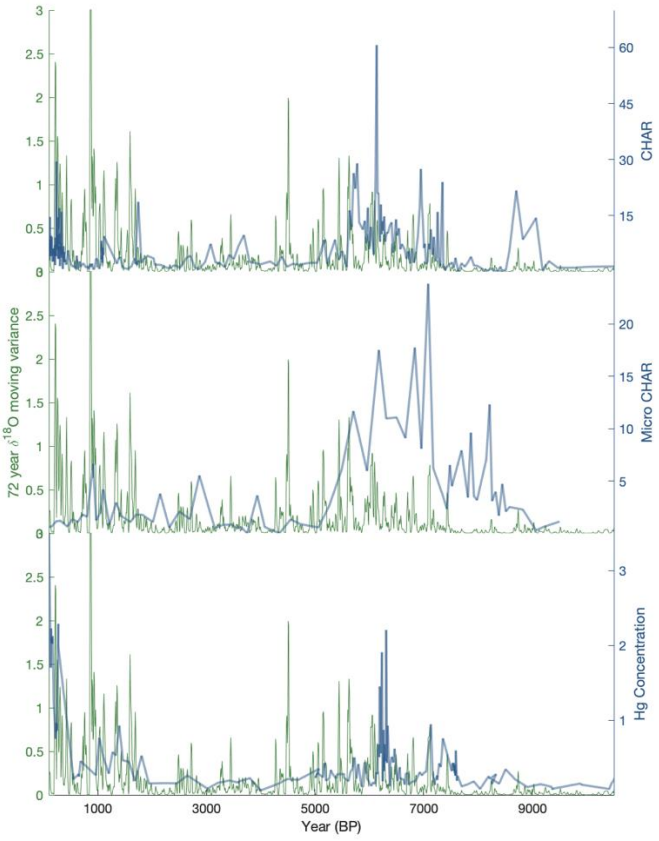

Figure 56. 72-year moving variance of δ18O records and three different fire indicators. (top) Macro charcoal accumulation rate (middle) micro charcoal accumulation rate and (bottom) Mercury concentration.

5.4.2 Unit II (8.5-4.95 kyr BP)

5.4.2.1 Opposing stratigraphic and isotopic indicators

Unit II is characterized by very carbonate rich sediments and alternations between fine laminae and massive carbonate packages indicative of variable lake levels. $CaCO_3$ accumulation rate is very high throughout in Unit II (Fig. 46). Lower lake levels can both increase $CaCO_3$ production rates and decrease $CaCO_3$ dissolution (Anderson et al. 2005). Additionally, the absence of *Myriophyllum* pollen prior to the abrupt stratigraphic shift to darker, more finely laminated sediments (Fig. 51) supports the idea that fluctuating lake levels periodically exposed shallow parts of the lake during Unit II, as *Myriophyllum* requires sufficient water levels to remain submerged in the littoral zone (Ge et al. 2021). While $\delta^{13}C_{Organic}$ values remain in the range of C3 vegetation, the most enriched Holocene values occur at approximately 6 kyr BP, indicating increased primary productivity and more complete biological sequestration of isotopically light carbon during hot summers with low lake levels (Hillman et al. 2018, Hodell and Schelske 1998). Enriched $\delta^{13}C_{Organic}$ values may suggest a greater contribution from vegetation which utilizes the C4 photosynthetic pathway—however pollen spectra shows a landscape containing primarily C3 vegetation (arboreal species and *Artemisia)* without a drastic increase in *graiminae* which is generally associated with C4 photosynthesis.

Curiously, $\delta^{18}O$ is lowest during this period, suggesting wet cool-season conditions (Fig. 48, Fig. 54). Steinman et al. (2016) attributed discrepancies in middle Holocene hydroclimate records to different seasonal sensitivities. As $\delta^{18}O_{carb}$ largely reflects the amount of cool-season precipitation and pollen, lake-level, and diatom-based reconstructions are more sensitive to year-round effective moisture, these discrepancies may well reflect enhanced seasonal contrast. Tropical Pacific mean-state conditions were broadly La Niña/PDO- like between 8000-4200 BP,

which brought increased cool-season precipitation to northwestern North America (Barron et al. 2011). A reduced east-west temperature gradient in the tropical Pacific (Koutavas and Joanides, 2012) and cooler northeast Pacific sea surface temperatures (Praetorious et al. 2020) support this claim (Fig. 54). Summer insolation, however, was still elevated compared to modern values, and model simulations have long indicated a strengthened eastern Pacific subtropical high, which would have produced hot, dry summers (Bartlein et al. 1998). Crucially, multiproxy analyses from Crevice Lake, WY and Castor Lake, WA also pair $\delta^{18}O_{carb}$ measurements with pollen (Crevice Lake, Whitlock et al. 2012) and stratigraphic (Castor Lake, Lehmann et al. 2021) records. Sedimentary facies from Castor Lake also indicate low stands until 6200 BP despite the lowest $\delta^{18}O_{carb}$ values occurring at approximately this time (Lehmann et al. 2021). This pattern may in part result from the hydrological influence of the Mazama tephra on the landscape, however (Steinman et al. 2019, see section 4.2.2). $\delta^{18}O_{carb}$ from Crevice Lake, WY also supports wetter winter conditions during the middle Holocene (7500-2500 BP) than during the late Holocene (2500-0 BP). Crucially, pollen assemblages from Crevice point to the middle Holocene being drier overall as well. In summary, Round Lake, Castor Lake, and Crevice Lake all support the idea that the northwestern United States was marked by drier summers and wetter winters between 5-7 kyr BP.

5.4.2.2 Impacts of the Mazama tephra deposition on the landscape

The eruption of Mount Mazama (approximately 7.6 kyr BP) left an ash blanket spanning approximately 1.7 million km^2 of western North America. Previous research has demonstrated the capacity for the resultant tephra to enhance water retention in soils given its high porosity (Steinman et al. 2019). Other studies have focused on terrestrial ecological response to the ash blanket on the landscape. Long et al. (2014), working close to the site of the eruption in high-

altitude sites in central Oregon, suggest that the ash blanket initially disrupted understory vegetation, as herbaceous pollen accumulation rates decrease in the immediate aftermath of the tephra. Further away from the eruption, a series of high-resolution pollen records from the Greater Yellowstone area show an increase in *Artemisia* on the landscape for an extended period (Schiller et al. 2020). An increase in *Artemisia* pollen and a decline in *Pinus* pollen follow the Mazama tephra layer at Round Lake (Fig. 57); a post-Mazama *Artemisia* maxima in several other records from the northern Rockies and interior northwest is also apparent (Fig. 55). Associated with these shifts is a long-term increase in charcoal accumulation as well as mercury deposition, another indicator of biomass burning (e.g. Pompeani et al. 2018).

At Round Lake, canonical correspondence analysis performed with 3 environmental variables ($\delta^{13}C_{Organic,}$ $\delta^{13}C_{CaCO3}$, and % organic matter) explained 55% of the total inertia in the pollen dataset and indicates that the landscape remains rich in herbaceous taxa until approximately 4.6 kyr BP, about 3 kyr after the Mazama eruption (Fig. 58). $\delta^{18}O_{carb}$ values over this time are low, indicating relatively wet conditions and cannot explain the sustained prevalence of herbaceous taxa and fire (Fig. 57). Instead, five overlapping factors likely contributed to the persistence of *Artemisia* on the landscape after the Mazama eruption. First, as described in section 4.2.1, $\delta^{18}O_{carb}$ values show wet cool-seasons, but arid and evaporative summers may have prevented the colonization of arboreal vegetation on the landscape. Next, the immediate transition to *Artemisia* may have increased the prevalence of fire on the landscape. In some sagebrush dominated regions, wetter winter conditions such as those indicated by the $\delta^{18}O_{carb}$ record, are generally associated with greater fire activity (Miller and Tausch 2001). As pulses of tree-recruitment in dry western forests rely on longer fire-free intervals (Dugan and Baker 2015), this would have inhibited the establishment of arboreal species. Frequent fires in sagebrush steppe-dry forest ecotones have

previously been demonstrated to hinder the spread of trees even when climatic and edaphic conditions are favorable to their growth (Mensing et al. 2006). Third, more variable hydroclimate over multidecadal timescales may have hindered the re-establishment of *pinus* on the landscape. Intense, cyclic shifts between wet and dry periods become prominent features of the Round Lake $\delta^{18}O$ record after the deposition of the Mazama tephra (Fig. 57, Fig. 59). The establishment of *pinus* in dry western forests is hindered by multidecadal droughts (Gray et al. 2006). This may have forestalled the rise in arboreal taxa despite long-term increases in winter precipitation. Additionally, the amplitude of multidecadal wet/dry cycles has also been shown to enhance fire activity (Mark et al. 2023, Fig. 56). As described above, this would have the effect of further inhibiting the recruitment of arboreal vegetation. Fourth, the deposition of tephra on the landscape created long-term edaphic conditions favorable to *Artemisia.* Steinman et al. (2019) note that the Mazama eruption altered catchment hydrological characteristics for centuries at nearby Castor Lake, resulting from the development soils with high water retention capacities (McDaniel et al. 2005) which *Artemisia* grows well in (Schiller et al. 2020). Finally, the abrupt decrease in *pinus* on the landscape may have increased runoff and decreased evapotranspiration which would increase overall P-E balance. Forest clearance has previously been shown to make $\delta^{18}O_{carb}$ values more negative (Rosenmeier et al. 2002). Thus, the actual hydroclimate conditions of the watershed may be drier than $\delta^{18}O_{carb}$ values indicate in the immediate aftermath of the Mazama tephra. These five factors, operating simultaneously, help elucidate the means through which autoregressive ecosystem processes operate, preserving a sagebrush steppe environment when ambient hydroclimate would have favored the establishment of dry forests.

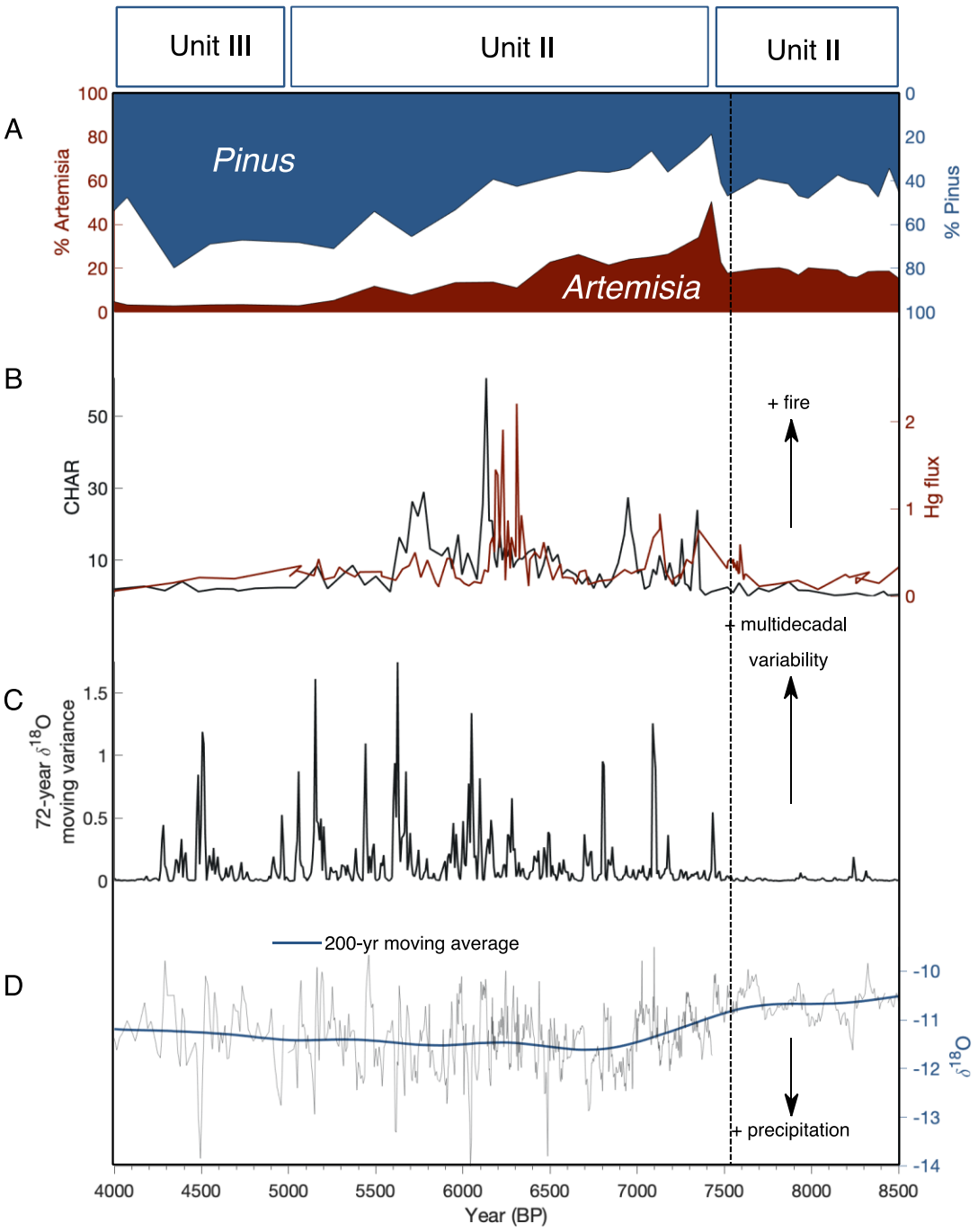

Figure 57. Post Mazama landscape disruption. (A) *Artemisia* and *Pinus* percentages (B) CHAR and Hg concentration (C) multidecadal hydroclimate variability and (d) $\delta^{18}O$ from Round Lake (blue line is raw data, green line indicates 200 year loess smoothing filter) during immediately before and after the deposition of the Mazama tephra (vertical dashed line).

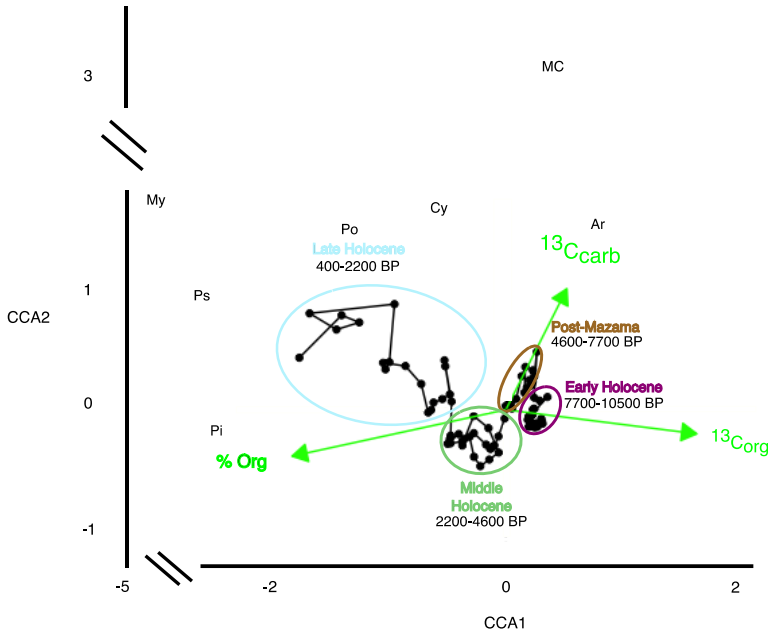

Figure 58. Canonical correspondence analysis (CCA) of pollen types and microcharcoal accumulation with δ13Ccarbonate , δ13Corganic and % organic material as explanatory variables. Pi=*Pinus* Ps=*Pseudotsuga* My=*Myriophyllum* Po=*Poaceae* Cy=*Cyperaceae* MC=microcharcoal Ar=*Artemisia*. Diagonal black lines indicate axes breaks.

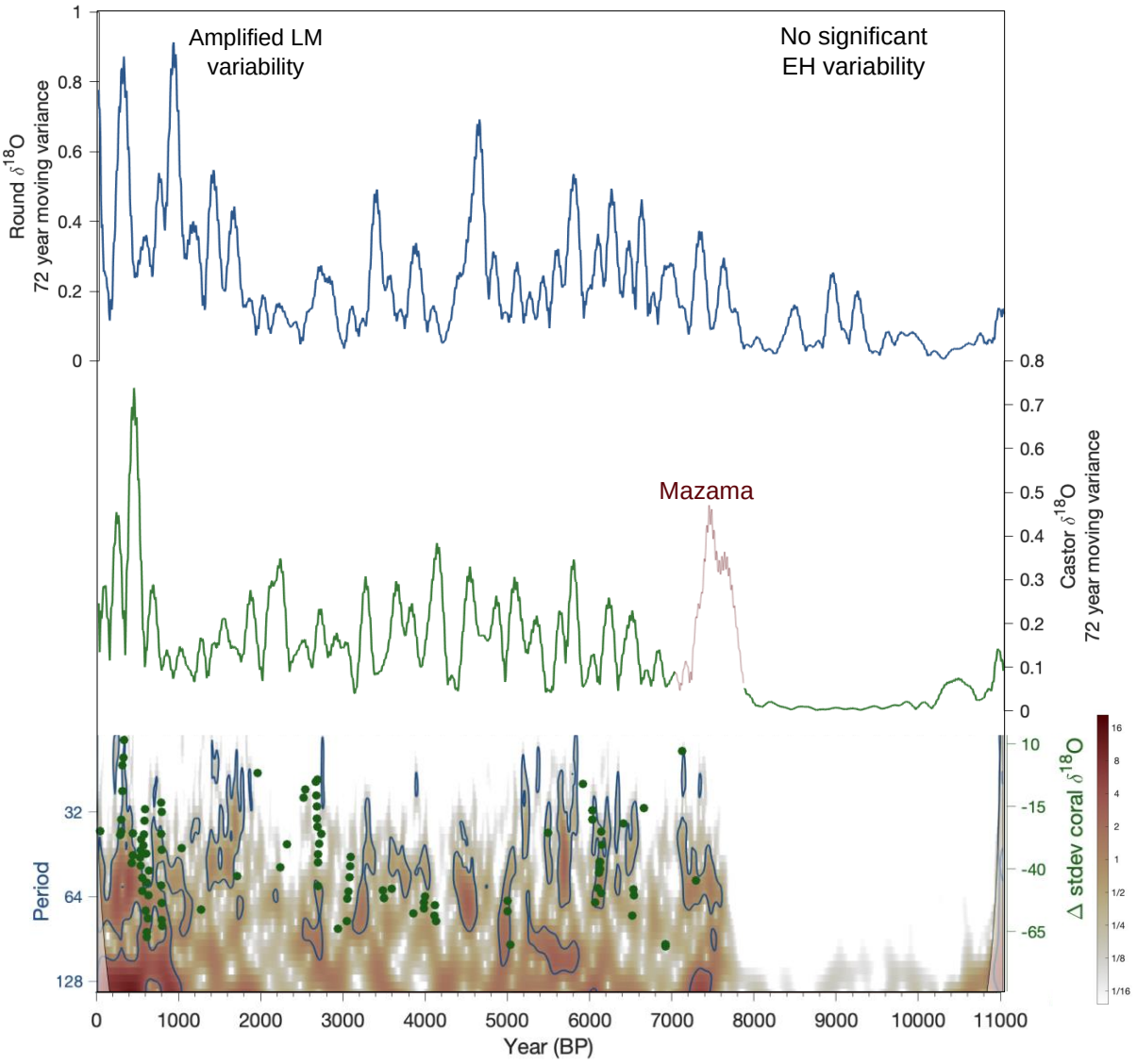

Figure 59. 72-year moving variance in δ18O records from Round, Castor, and PO Lime lakes and cross-wavelet for both records. Thin red line in Castor Lake record covers the period immediately following the Mazama tephra deposition, which created enriched oxygen isotope values for several centuries afterward (see Steinman et al. 2019).

5.4.3 Unit III (4.95 kyr-present)

The 4.95 kyr-present Round Lake sequence consists of finely laminated black, organic-rich sediments interspersed with light, carbonate rich layers (Fig. 46, Fig. 51), indicative of lake levels which remained high for the remainder of the sequence. This interpretation is supported by the persistence of *Myriophyllum* pollen, which suggest the littoral zone remained submerged. Despite this, late Holocene, $\delta^{18}O$ values indicate conditions have gotten slightly drier over the past 6 kyr BP and much more variable over the last millennium consistent with nearby Castor Lake (Nelson et al. 2011, Fig. 57, Fig. 59). The inferred shift to higher lake levels, then, may be a result of reduced summer temperatures and decreased evaporative demand, resulting from lower summer insolation. Cooler summers are consistent with a chironomid-based July temperature reconstruction from proximal Windy Lake, BC (Chase et al. 2008). A resultant transition to greater effective moisture and higher lake levels, is also consistent with diatom-based hydrological reconstructions from Roche and Big Lakes, BC (Fig. 54, Mushet et al. 2022).

Pinus and *pseudotsuga* increase after 4.5 kyr BP, at the expense of *poaceae* and *artemisia*, heralding a shift towards the modern dry forest setting of Round Lake. Charcoal accumulation rates are generally lower than they are during the middle Holocene, indicating that the transition to greater arboreal vegetation and higher/more stable lake levels was associated with reduced fire activity. The Medieval Climate Anomaly (MCA, 950-1250 CE) is seemingly moist and stable compared to the subsequent Little Ice Age (LIA, 1450-1850) (Steinman et al. 2014, Mark et al. 2023). Mercury accumulation rates are similar to trends in charcoal accumulation for the majority of the Holocene (Fig. 52, Fig. 56), as fire volatilizes mercury previously sequestered in soil and vegetation, which can then be transported to the lake via runoff or aeolian deposition (Pompeani et al. 2018). Fire is not the sole source of Hg flux in lacustrine ecosystems, however, and However,

the onset of extensive gold mining in the Cascades in the late 19th century (Helmer et al. 2020) led to an abrupt increase in Hg concentration in the Round Lake sedimentary record (Fig. 52). Artisanal gold mining is the largest global source of anthropogenic Hg emissions, as extraction practices generally involve adding elemental Hg to sediments to isolate gold (Eagles-Smith et al. 2018).

5.4.4 Holocene-scale trends of multidecadal climate variability

Few Holocene-scale hydroclimate proxy records are analyzed at sufficient temporal resolution to detect shifts in multidecadal variability. Developing proxy reconstructions sensitive to these systems is crucial to understanding how multidecadal climate variability changes under different background climate configurations, or whether these systems persist at all, absent volcanic and anthropogenic aerosol forcing (Mann et al. 2021). During the early Holocene, multidecadal variability in the Round Lake $\delta^{18}O$ record is very muted and Castor and Round Lakes are entirely devoid of significant multidecadal periodicities (Fig. 59, Fig. 60). Multidecadal variability at both Castor and Round Lakes becomes prominent prior to 7 kyr BP and both sites exhibit significant PDO-scale oscillations between 7-5 kyr BP. Crucially, this indicates that while overall cool-season precipitation may have been enhanced at 6 kyr BP, PDO-scale oscillations were still a prominent feature of regional climate. Why multidecadal variability prior to 7 kyr BP should be so minimal is not clear; there was a major reconfiguration of atmospheric circulation patterns in the North Pacific at approximately 8kyr BP which may have weakened the Aleutian Low and moved it westward (Lasher et al. 2021). This configuration would, theoretically, more closely resemble PDO- conditions.

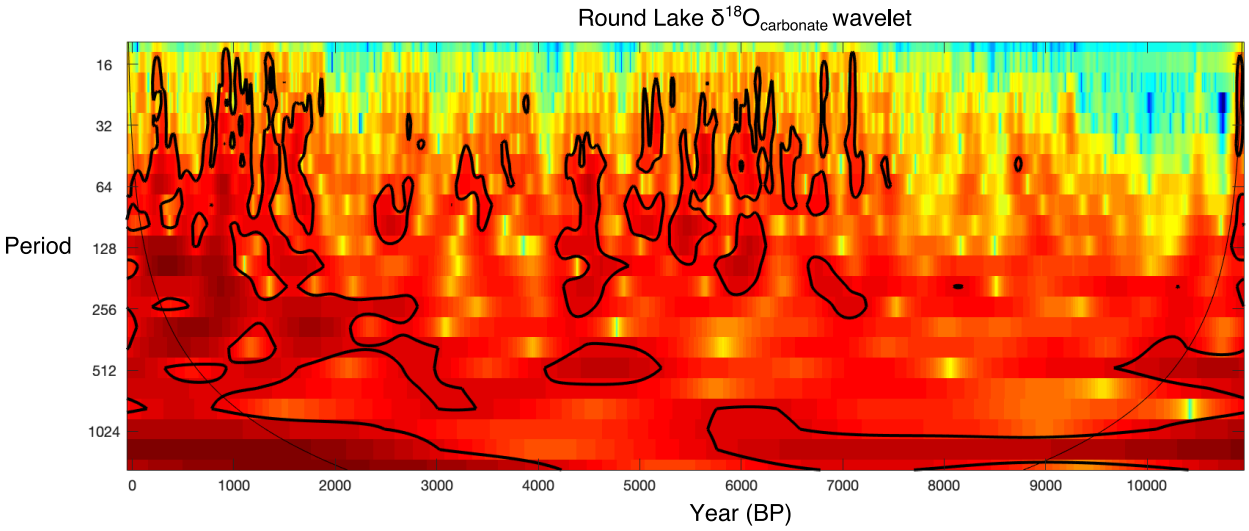

Figure 60. Wavelet power spectrum for the Round Lake δ18O carbonate record. Portions outlined in black indicate periodicities that are significant at a 95% confidence interval.

Interannual tropical Pacific climate variability (ENSO) influences PDO-scale climate phenomena in the northern mid-latitude Pacific (Nidheesh et al. 2017, Newman et al. 2016). To test the long-term relationship between ENSO strength and multidecadal climate variability, we compare the $\delta^{18}O$ cross-wavelet from Castor and Round Lakes to the Palmyra Atoll coral record of ENSO variability (Grothe et al. 2020). When ENSO variance recorded by the corals is high, Castor and Round Lakes share significant periodicities in the 16-32 year band (Fig. 59). Between 5-3 kyr BP coral records, including those from Palmyra Atoll, note a severe decrease in ENSO variance (Emile-Geay et al. 2016). Shared oscillations in the Castor and Round Lake $\delta^{18}O$ records at this time are almost entirely absent and confined to periodicities of 64-years or greater (Fig. 59). These findings highlight how high-frequency variability characteristic of ENSO in the tropical Pacific is integrated and smoothed at the mid-latitudes, manifesting as PDO-scale climate variability.

5.4.5 Ecosystem dynamics and their relation to multidecadal-centennial hydroclimate forcing

The degree to which vegetation exists in equilibrium with climate is the focus of considerable discussion over long timescales and across abrupt climatic transitions (Webb et al. 1986, Tinner and Lotter 2001, Mann et al. 2019). Considerably less attention has been paid to the role persistent multi-decadal and centennial-scale climate variability plays in modulating terrestrial ecosystem composition (Jackson et al. 2009) even though equilibrium dynamics on this scale have important implications for management decisions (Williams et al. 2021, Svenning and Sandel 2013). Existing studies tend to focus on the geographic distribution of species during abrupt climate changes (Tinner and Lotter 2001, Shuman et al. 2009) or the response of ecological communities to the introduction of non-native species (Willis and Birks 2006). Almost no studies pair independent hydroclimate data with pollen and wildfire data from the same sedimentary sequence (Williams et al. 2002). To better understand the sensitivity of terrestrial ecosystems to antecedent climate forcing, we correlated arboreal and herbaceous taxa to mean $\delta^{18}O$ values over a range of time spans (Fig. 10); that is, rather than comparing each pollen sample to the $\delta^{18}O_{carb}$ sample from the same horizon, we compared them to mean $\delta^{18}O_{carb}$ values of preceding samples (Fig. S9). For arboreal species *pinus, pseudotsuga,* and *picea,* and for CHAR, incorporating 60+ antecedent years of $\delta^{18}O$ averages show the highest correlations (Fig. 10a, see Fig. S9 for schematic illustration of methodology). Arboreal vegetation in the study area is constantly "playing catchup" and never fully reaches equilibrium with climate during the Holocene. Williams et al. (2002) used cross-correlation analysis to demonstrate lag-times between pollen and $\delta^{18}O_{chironomid}$ of approximately 100 years across the glacial-interglacial transition at 11 sites in northern Europe and eastern Canada, consistent with the findings presented here. This study demonstrates that

these disequilibria (1) do not arise solely from abrupt shifts in climate, but rather are a persistent feature of slow-growing arboreal populations throughout the Holocene and (2) can result from changes in precipitation in addition to temperature. Significantly, *artemisia* and *poaceae* are seemingly less sensitive to antecedent P-E balance. This discrepancy likely reflects the more immediate response of perennial, shallow-rooted grasses and shrubs than long-lived arboreal species to long-term precipitation variability (Verbruggen et al. 2021). Experimental results suggest that shrub and grass species respond to interannual climate variability on sub-decadal timescales (Winkler et al. 2019, Gherardi and Sala 2015). As precipitation is anticipated to become more variable in response to anthropogenic warming, smaller, faster growing herbaceous vegetation may fare better in response to future climate change even absent mean-state precipitation decreases and increased evaporative stress.

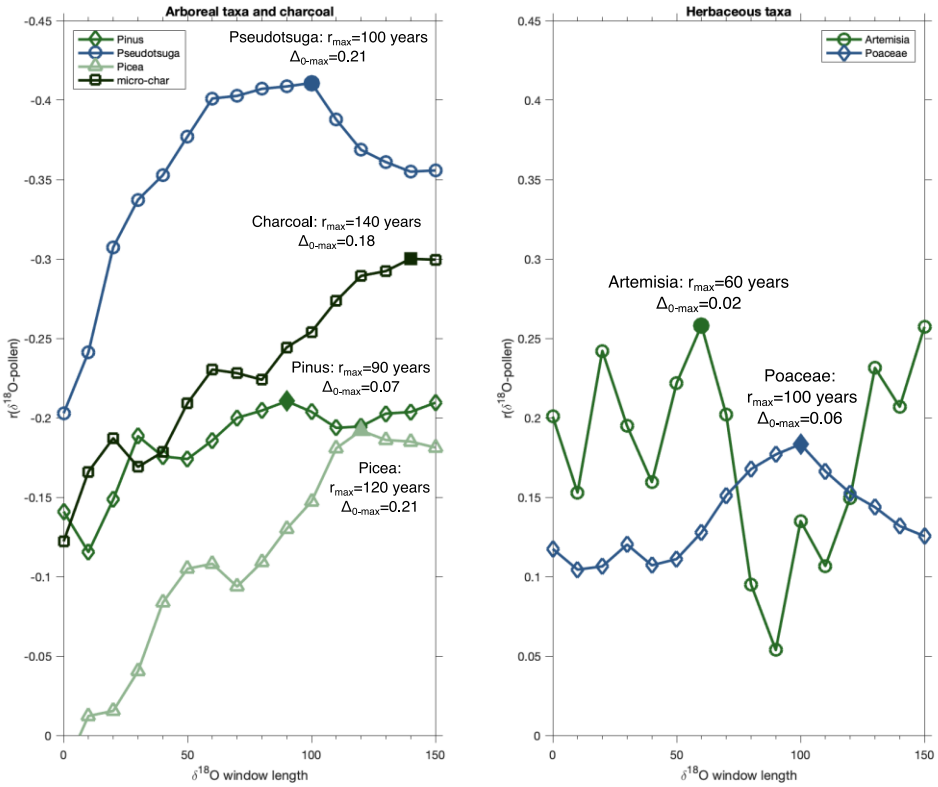

Figure 61. Correlation between Round Lake δ18O values with different preceding window lengths (see Fig. 62 for illustration of method). (A) shows arboreal and charcoal results while (B) shows herbaceous pollen. Solid shape indicate the time step with the highest r value.

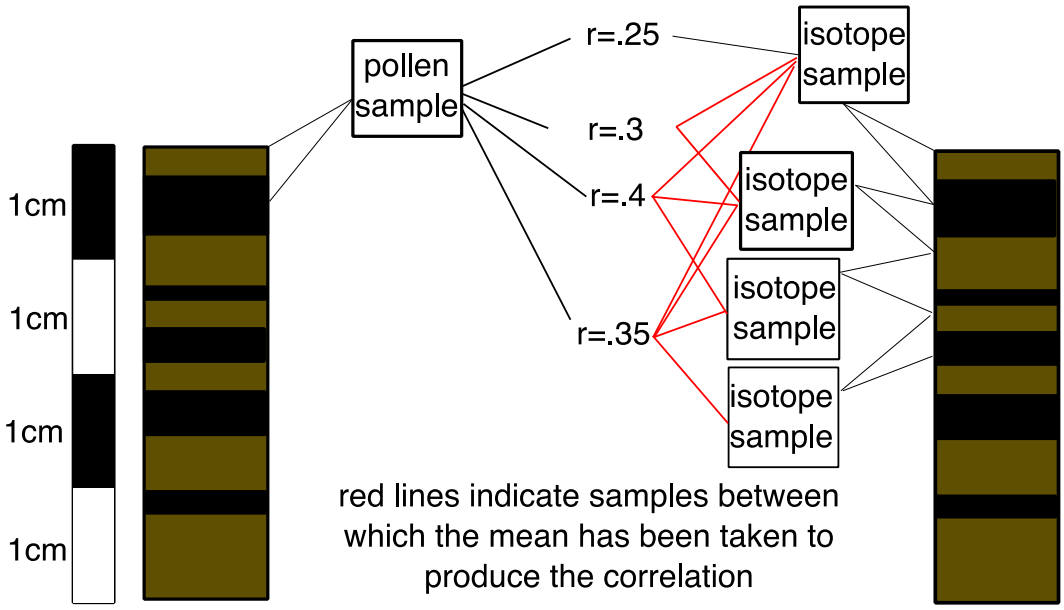

Figure 62. Simplified conceptual representation of the method used to create Fig. 61.

5.5 Conclusions

High-resolution multiproxy analysis from Round Lake, WA sheds light on the coevolution of regional hydroclimate climate and ecology over the course of the Holocene. Stratigraphic indicators and oxygen isotopes both suggest earliest part of the Holocene was marked by persistent aridity and steppe-like vegetation. Fire activity was reduced in this period, owing to a lack of fuels on the landscape. The eruption of Mount Mazama at ~7600 BP left a thick blanket of ash on the landscape and caused an immediate shift towards greater *Artemisia*. Despite increased precipitation in the millennia following the eruption, pollen assemblages indicate the landscape remains largely steppe-like. This owes to several overlapping factors, including increased hydroclimate variability, with multidecadal droughts inhibiting tree recruitment, increased fire activity, and changes in soil characteristics. Additionally, increases in runoff immediately after of

the eruption (Rosenmeier et al. 2002) may have reduced water retention on the landscape and increased runoff into the lake, skewing the oxygen isotope balance of lake water more negative. The stratigraphy of the core between the Mazama tephra and 4950 BP is indicative of lower and variable lake levels. As the oxygen isotopes primarily reflect the amount of cool-season precipitation, we conclude this period was marked by amplified hydroclimatic seasonality—that is, wetter winters and drier summers. Between 4950 BP and present, stratigraphy and the persistence of *Myriophyllum* pollen suggest overall P-E balance increased, even as oxygen isotopes suggest decreasing cool-season precipitation over the same period. Pollen and fire indicators suggest the establishment of a more closed forest and decreasing fire over this interval as well.

The resolution of the oxygen isotope record at Round Lake also offers the opportunity to examine multidecadal hydroclimate variability and test its relationship to Pacific-wide climate systems such as the El Niño Southern Oscillation. At both Round Lake and nearby Castor Lake, multidecadal variability is very muted during the early Holocene. Both lakes begin to detect statistically significant periodicities in the 16-32 year (PDO-scale) band at approximately 7 kyr BP. Between 5-3 kyr BP, significant periodicities at both sites only persist at lower frequency (~64 year) scales, but the past millennium contains the highest amplitude cycles between wet and dry of any period over the Holocene. These trends closely match reconstructed ENSO strength from coral $\delta^{18}O$ records in the tropical Pacific. When ENSO amplitude is high, PDO-scale variability is prominent at Castor and Round Lakes.

The multidecadal component of hydroclimate variability is important to the ecological communities surrounding Round Lake. Correlations between arboreal pollen species and $\delta^{18}O_{carb}$ improve when 50-100 years of antecedent $\delta^{18}O$ measurements are considered. No such pattern holds true with *Artemisia* or *Poaceae*, reflecting the shorter response of shallow rooted, faster

growing taxa to ambient climate conditions. Fire activity, too, is sensitive to the amplitude of multidecadal climate forcing. The increased amplitude of wet/dry cycles leads to abundant fuel production during wet phases, which subsequently desiccate and burn readily during dry periods. The use of high-resolution multi-proxy analyses help shed light on how Pacific dynamics influence hydroclimate in northwestern North America, and how these dynamics in term shape terrestrial ecosystems.

6.0 Summary and Direction for Future Research

The previous four chapters provide high-resolution paleoclimate perspectives on changes in Pacific climate systems over the past 12,000 years. Each chapter demonstrates long-term variability in (quasi)-oscillatory climate modes which would be difficult or impossible to detect using lower-frequency paleoclimatic and paleolimnological analyses. Chapter 2 focuses on refining the interpretation of the widely cited Laguna Pallcacocha sedimentary record from the Ecuadorian Andes. The finely laminated sediments of Laguna Pallcacocha had previously been analyzed for changes in color, with lighter colored layers indicating flood deposits driven by short-lived high-intensity rainstorms. After refining the age model using new ^{210}Pb and ^{137}Cs dates, recent flood deposits show good agreement with instrumentally and historically documented El Niño events in which warming is focused in the eastern tropical Pacific. XRF-based records of rapid terrigenous sedimentation are largely consistent with sediment color metrics over the past 7000 years, but diverge in the early Holocene, possibly owing to changes in land cover. The new XRF dataset suggests that El Niño-driven floods were more frequency during the early Holocene than in the middle Holocene, but less frequent than in the late Holocene. This pattern is broadly consistent with an emerging consensus of proxy records from different archive types and different locations, as well as with hypothesized orbital controls on El Niño development. However, centennial-scale variability in El Niño frequency cannot be explained through orbital variations, preserving a role for either internal dynamics or alternative forcing mechanisms.

Chapter 3 expands on the work presented in chapter 2 by incorporating sedimentary records from lakes proximal to Laguna Pallcacocha. Topographic and geomorphic characteristics unique to each watershed dictate the production and transport of clastic material from the surrounding

basin into the lake, making each sedimentary record sensitive to flooding events of different magnitudes. Laguna Pallcacocha, the most sensitive sedimentary, is effectively a record of El Niño frequency, while the other two basins, which require comparatively high intensity precipitation maxima to generate clastic deposits, are indicative of particularly high amplitude El Niño events. While frequency and amplitude are largely coupled throughout the Holocene, the Medieval Climate Anomaly was marked by frequent, low amplitude El Niños and the Little Ice Age was marked by comparatively fewer events, but a preponderance of high amplitude events. While the middle Holocene seemingly contained relatively few El Niño's overall, many of these events were of particularly high intensity. By interpreting proxies according to their sensitivity to frequency and amplitude, lingering discrepancies between existing records from different archive types can be largely resolved.

Chapter 4 focuses on high-resolution oxygen isotope and charcoal accumulation records from Castor and Round Lakes in eastern Washington, USA. The oxygen isotope records are of sufficient resolution to be quantitatively compare to instrumental records and tree-ring proxies. Consistent with previous proxy-system modeling work, the oxygen isotope signal is most strongly controlled by cool-season precipitation. Correlations between oxygen isotopes and nearby tree-ring width records are highest when a 20-year lowpass filter is applied to the tree-ring chronologies, mimicking the residence time of lake water. Detrending of the lake sediment records also produces higher correlations to tree-ring chronologies, as the removal of growth signals when compositing individual organisms into a synthesis removes low-frequency climate variability. The Medieval Climate Anomaly experienced greater cool-season precipitation and more stable hydroclimatic conditions than the subsequent Little Ice Age. Charcoal accumulation rates from the semi-arid eastern Cascades all show greater biomass burning during the Little Ice Age,

associated with enhanced multidecadal hydroclimate variability, possibly reflecting cyclic periods of fuel accumulation, desiccation, and burning. The forced removal of native Americans from the landscape during the middle of the 19th century.

Chapter 5 extends the Round Lake sedimentary record through the entirety of the Holocene, and pairs oxygen isotope measurements with pollen accumulation, organic carbon isotopes, mercury accumulation rates, and physical sedimentology. The oxygen isotope record is broadly consistent with nearby Castor Lake, showing a persistently arid early Holocene, moist winter conditions during the middle Holocene, and a moist and highly variable late Holocene. The eruption of the Mazama tephra at ~7700 BP had pronounced impacts on the surrounding terrestrial ecology, fostering the spread of *Artemisia* at the expense of arboreal taxa, even despite wetter background conditions. The onset of more variable hydroclimate conditions, high summer insolation, and increased fire activity contributed to the persistence of this climate-vegetation disequilibria.

Several directions for future research, in both the Ecuadorian Andes and the Pacific Northwest, follow naturally from this project. While the three records excel at resolving abrupt, short-lived hydrological extremes, they fail to capture low-frequency changes in regional water balance. Additionally, the region receives precipitation from both Pacific (particularly during El Niños) and Atlantic (via the South American Seasonal Monsoon) sources. Isotopes from leaf wax lipids in the three records would help constrain changes in the relative strength and importance of both ENSO and the monsoon. Given the importance of El Niño in influencing societal development in western South America, quantitative comparison of flood deposits with archaeological evidence would be valuable in understanding the complex human-climatic relationships which have emerged over the past several thousand years.

In the northwest, the paired use of hydroclimate and fire proxies is severely underexplored. A major shortcoming of this study is that fire return intervals in Castor and Round Lake are too short to be resolved using charcoal accumulation records. Other sites with existing Holocene-scale oxygen isotope reconstructions (such as Paradise Lake, British Columbia and Cleland Lake, British Columbia) derive from regions which experience low frequency-high severity fire regimes in which individual fire events can be discerned. Continuous charcoal accumulation records from these sites will allow for long-term quantitative reconstructions of how fire return intervals change under different background climate states. Additionally, polycyclic aromatic hydrocarbons (PAHs) could provide insight into the fuel source and intensity of fires in different biomes across the region. As fire in the western United States exceeds the relatively short-lived durations of instrumental observations, paired climate-fire proxy data represents our only means of empirically understanding the long-term impact of climate change on this keystone ecological process.

Bibliography

Abram, N. J., et al. (2020). "Palaeoclimate perspectives on the Indian Ocean dipole." Quaternary Science Reviews **237**: 106302.

Abram, N. J., et al. (2020). "Coupling of Indo-Pacific climate variability over the last millennium." Nature **579**(7799): 385-392.

An, S.-I. and J. Choi (2014). "Mid-Holocene tropical Pacific climate state, annual cycle, and ENSO in PMIP2 and PMIP3." Climate Dynamics **43**(3-4): 957-970.

Anderson, B. T., et al. (2013). "Triggering of El Niño onset through trade wind–induced charging of the equatorial Pacific." Geophysical Research Letters **40**(6): 1212-1216.

Anderson, L., et al. (2005). "Regional atmospheric circulation change in the North Pacific during the Holocene inferred from lacustrine carbonate oxygen isotopes, Yukon Territory, Canada." Quaternary Research **64**(1): 21-35.

Andreoli, R. V., et al. (2017). "The influence of different El Niño types on the South American rainfall." International Journal of Climatology **37**(3): 1374-1390.

Anttila-Hughes, J. K., et al. (2021). "ENSO impacts child undernutrition in the global tropics." Nature communications **12**(1): 5785.

Arnaud, F., et al. (2002). "Flood and earthquake disturbance of 210Pb geochronology (Lake Anterne, NW Alps)." Terra Nova **14**(4): 225-232.

Ashok, K., et al. (2007). "El Niño Modoki and its possible teleconnection." Journal of Geophysical Research: Oceans **112**(C11).

Asmerom, Y., et al. (2020). "Intertropical convergence zone variability in the Neotropics during the Common Era." Science advances **6**(7): eaax3644.

Astudillo, P. X., et al. (2014). "The impact of roads on the avifauna of páramo grasslands in Cajas National Park, Ecuador." Studies on neotropical fauna and environment **49**(3): 204-212.

Bandowe, B. A. M., et al. (2018). "A 150-year record of polycyclic aromatic compound (PAC) deposition from high Andean Cajas National Park, southern Ecuador." Science of the total environment **621**: 1652-1663.

Barron, J. A. and L. Anderson (2011). "Enhanced Late Holocene ENSO/PDO expression along the margins of the eastern North Pacific." Quaternary International **235**(1-2): 3-12.

Barron, J. A., et al. (2003). "High-resolution climatic evolution of coastal northern California during the past 16,000 years." Paleoceanography **18**(1).

Bartlein, P. J., et al. (1998). "Paleoclimate simulations for North America over the past 21,000 years: features of the simulated climate and comparisons with paleoenvironmental data." Quaternary Science Reviews **17**(6-7): 549-585.

Bartlein, P. J., et al. (2014). "Paleoclimate." Climate Change in North America: 1-51.

Bennett, K. D. and K. J. Willis (2001). "Pollen." Tracking environmental change using lake sediments: terrestrial, algal, and siliceous indicators: 5-32.

Berntsson, A., et al. (2014). "Late-Holocene temperature and precipitation changes in Vindelfjällen, mid-western Swedish Lapland, inferred from chironomid and geochemical data." The Holocene **24**(1): 78-92.

Besonen, M. R., et al. (2008). "A 1,000-year, annually-resolved record of hurricane activity from Boston, Massachusetts." Geophysical Research Letters **35**(14).

Bjerknes, J. (1969). "Atmospheric teleconnections from the equatorial Pacific." Monthly weather review **97**(3): 163-172.

Boyd, R. (1999). Indians Fire and the Land, Oregon State University Press Corvallis, Oregon, USA.

Boyd, R. T. (1998). "Demographic history until 1990." Handbook of North American Indians **12**: 467-483.

Brown, E. T. (2015). Estimation of biogenic silica concentrations using scanning XRF: insights from studies of Lake Malawi sediments. Micro-XRF studies of sediment cores, Springer**:** 267-277.

Brunelle, A. (2022). "Interactions Among the Fire, Vegetation, the North American Monsoon and the El Niño-Southern Oscillation in the North American Desert Southwest." Frontiers in Ecology and Evolution **10**: 145.

Brunelle, A. and C. Whitlock (2003). "Postglacial fire, vegetation, and climate history in the Clearwater Range, Northern Idaho, USA." Quaternary Research **60**(3): 307-318.

Brunelle, A., et al. (2005). "Holocene fire and vegetation along environmental gradients in the Northern Rocky Mountains." Quaternary Science Reviews **24**(20-21): 2281-2300.

Buchanan, P. and K. Savigny (1990). "Factors controlling debris avalanche initiation." Canadian Geotechnical Journal **27**(5): 659-675.

Bush, M. B., et al. (2017). "Human disturbance amplifies Amazonian El Niño–Southern Oscillation signal." Global change biology **23**(8): 3181-3192.

Cai, W., et al. (2019). "Pantropical climate interactions." Science **363**(6430): eaav4236.

Carré, M., et al. (2021). "High-resolution marine data and transient simulations support orbital forcing of ENSO amplitude since the mid-Holocene." Quaternary Science Reviews **268**: 107125.

Carré, M., et al. (2014). "Holocene history of ENSO variance and asymmetry in the eastern tropical Pacific." Science **345**(6200): 1045-1048.

Chase, M., et al. (2008). "Midge-inferred Holocene summer temperatures in southeastern British Columbia, Canada." Palaeogeography, Palaeoclimatology, Palaeoecology **257**(1-2): 244-259.

Chen, L., et al. (2019). "Towards understanding the suppressed ENSO activity during mid-Holocene in PMIP2 and PMIP3 simulations." Climate Dynamics **53**(1): 1095-1110.

Chen, S., et al. (2016). "A high-resolution speleothem record of western equatorial Pacific rainfall: Implications for Holocene ENSO evolution." Earth and Planetary Science Letters **442**: 61-71.

Cobb, K. M., et al. (2003). "El Niño/Southern Oscillation and tropical Pacific climate during the last millennium." Nature **424**(6946): 271-276.

Cobb, K. M., et al. (2013). "Highly variable El Niño–Southern Oscillation throughout the Holocene." Science **339**(6115): 67-70.

Cole, J. E., et al. (1993). "Recent variability in the Southern Oscillation: Isotopic results from a Tarawa Atoll coral." Science **260**(5115): 1790-1793.

Collins, J. A., et al. (2017). "Rapid termination of the African Humid Period triggered by northern high-latitude cooling." Nature communications **8**(1): 1-11.

Conroy, J. L., et al. (2008). "Holocene changes in eastern tropical Pacific climate inferred from a Galápagos lake sediment record." Quaternary Science Reviews **27**(11-12): 1166-1180.

Cook, E. R., et al. (2004). "Long-term aridity changes in the western United States." Science **306**(5698): 1015-1018.

Cooper, C. S., et al. (2021). "A lake sediment–based paleoecological reconstruction of late Holocene fire history and vegetation change in Great Basin National Park, Nevada, USA." Quaternary Research **104**: 28-42.

Coulthard, B. L., et al. (2021). "Snowpack signals in North American tree rings." Environmental Research Letters **16**(3): 034037.

d'Arrigo, R., et al. (2005). "On the variability of ENSO over the past six centuries." Geophysical Research Letters **32**(3).

d'Arrigo, R., et al. (2001). "Tree-ring estimates of Pacific decadal climate variability." Climate Dynamics **18**(3): 219-224.

Dang, H., et al. (2020). "Pacific warm pool subsurface heat sequestration modulated Walker circulation and ENSO activity during the Holocene." Science advances **6**(42): eabc0402.

Dannenberg, M. P. and E. K. Wise (2016). "Seasonal climate signals from multiple tree ring metrics: A case study of Pinus ponderosa in the upper Columbia River Basin." Journal of Geophysical Research: Biogeosciences **121**(4): 1178-1189.

Davies, A., et al. (2012). "El Niño–southern oscillation variability from the late cretaceous Marca shale of California." Geology **40**(1): 15-18.

Davies, S. J., et al. (2015). "Micro-XRF core scanning in palaeolimnology: recent developments." Micro-XRF studies of sediment cores: 189-226.

Dee, S., et al. (2020). "Enhanced North American ENSO teleconnections during the Little Ice Age revealed by paleoclimate data assimilation." Geophysical Research Letters **47**(15): e2020GL087504.

Dee, S. G., et al. (2020). "No consistent ENSO response to volcanic forcing over the last millennium." Science **367**(6485): 1477-1481.

Denniston, R. F., et al. (2015). "Extreme rainfall activity in the Australian tropics reflects changes in the El Niño/Southern Oscillation over the last two millennia." Proceedings of the National Academy of Sciences **112**(15): 4576-4581.

Dombeck, M. P., et al. (2004). "Wildfire policy and public lands: integrating scientific understanding with social concerns across landscapes." Conservation biology **18**(4): 883-889.

Domínguez-Villar, D., et al. (2017). "The control of the tropical North Atlantic on Holocene millennial climate oscillations." Geology **45**(4): 303-306.

Dong, B. and R. T. Sutton (2007). "Enhancement of ENSO variability by a weakened Atlantic thermohaline circulation in a coupled GCM." Journal of Climate **20**(19): 4920-4939.

Du, X., et al. (2021). "High-resolution interannual precipitation reconstruction of Southern California: Implications for Holocene ENSO evolution." Earth and Planetary Science Letters **554**: 116670.

Dugan, A. J. and W. L. Baker (2015). "Sequentially contingent fires, droughts and pluvials structured a historical dry forest landscape and suggest future contingencies." Journal of Vegetation Science **26**(4): 697-710.

Emile-Geay, J., et al. (2016). "Links between tropical Pacific seasonal, interannual and orbital variability during the Holocene." Nature Geoscience **9**(2): 168-173.

Emile-Geay, J., et al. (2013). "Estimating central equatorial Pacific SST variability over the past millennium. Part II: Reconstructions and implications." Journal of Climate **26**(7): 2329-2352.

Emile-Geay, J. and M. Tingley (2016). "Inferring climate variability from nonlinear proxies: application to palaeo-ENSO studies." Climate of the Past **12**(1): 31-50.

Everett, R. L., et al. (2000). "Fire history in the ponderosa pine/Douglas-fir forests on the east slope of the Washington Cascades." Forest Ecology and Management **129**(1-3): 207-225.

Fasullo, J., et al. (2018). "ENSO's changing influence on temperature, precipitation, and wildfire in a warming climate." Geophysical Research Letters **45**(17): 9216-9225.

Fleischbein, K., et al. (2006). "Water budgets of three small catchments under montane forest in Ecuador: experimental and modelling approach." Hydrological Processes: An International Journal **20**(12): 2491-2507.

Foucher, A., et al. (2021). "A worldwide meta-analysis (1977–2020) of sediment core dating using fallout radionuclides including 137 Cs and 210 Pb xs." Earth System Science Data **13**(10): 4951-4966.

Fowler, A. M., et al. (2012). "Multi-centennial tree-ring record of ENSO-related activity in New Zealand." Nature Climate Change **2**(3): 172-176.

Fox Jr, K. F. (1970). Geologic map of the Oroville quadrangle, Okanogan County, Washington.

Freund, M. B., et al. (2019). "Higher frequency of Central Pacific El Niño events in recent decades relative to past centuries." Nature Geoscience **12**(6): 450-455.

Galloway, J. M., et al. (2011). "Hydrological change in the central interior of British Columbia, Canada: diatom and pollen evidence of millennial-to-centennial scale change over the Holocene." Journal of paleolimnology **45**: 183-197.

Garcia-Herrera, R., et al. (2008). "A chronology of El Niño events from primary documentary sources in northern Peru." Journal of Climate **21**(9): 1948-1962.

Gavin, D. G., et al. (2006). "Weak climatic control of stand-scale fire history during the late Holocene." Ecology **87**(7): 1722-1732.

Ge, Y., et al. (2021). "Revealing anthropogenic effects on lakes and wetlands: Pollen-based environmental changes of Liangzi Lake, China over the last 150 years." Catena **207**: 105605.

Gedalof, Z. e., et al. (2002). "A multi-century perspective of variability in the Pacific Decadal Oscillation: New insights from tree rings and coral." Geophysical Research Letters **29**(24): 57-51-57-54.

Gherardi, L. A. and O. E. Sala (2015). "Enhanced precipitation variability decreases grass-and increases shrub-productivity." Proceedings of the National Academy of Sciences **112**(41): 12735-12740.

Goddard, L. and A. Gershunov (2020). "Impact of El Niño on weather and climate extremes." El Niño Southern Oscillation in a Changing Climate: 361-375.

Gray, S. T., et al. (2006). "Role of multidecadal climate variability in a range extension of pinyon pine." Ecology **87**(5): 1124-1130.

Greene, C. A., et al. (2019). "The climate data toolbox for MATLAB." Geochemistry, Geophysics, Geosystems **20**(7): 3774-3781.

Griffiths, M. L., et al. (2020). "End of Green Sahara amplified mid-to late Holocene megadroughts in mainland Southeast Asia." Nature communications **11**(1): 1-12.

Grinsted, A., et al. (2004). "Application of the cross wavelet transform and wavelet coherence to geophysical time series."

Grissino Mayer, H. D. and T. W. Swetnam (2000). "Century scale climate forcing of fire regimes in the American Southwest." The Holocene **10**(2): 213-220.

Grothe, P. R., et al. (2020). "Enhanced El Niño–Southern oscillation variability in recent decades." Geophysical Research Letters **47**(7): e2019GL083906.

Hagemans, K., et al. (2021). "Patterns of alluvial deposition in Andean lake consistent with ENSO trigger." Quaternary Science Reviews **259**: 106900.

Hagemans, K., et al. (2022). "Intensification of ENSO frequency drives forest disturbance in the andes during the holocene." Quaternary Science Reviews **294**: 107762.

Halofsky, J. E., et al. (2020). "Changing wildfire, changing forests: the effects of climate change on fire regimes and vegetation in the Pacific Northwest, USA." Fire Ecology **16**(1): 1-26.

Hansen, B., et al. (2003). "Late-glacial and Holocene vegetational history from two sites in the western Cordillera of southwestern Ecuador." Palaeogeography, Palaeoclimatology, Palaeoecology **194**(1-3): 79-108.

Haug, G. H., et al. (2001). "Southward migration of the intertropical convergence zone through the Holocene." Science **293**(5533): 1304-1308.

Hayes, F. and E. Anthony (1958). "Lake Water and Sediment: I. Characteristics and Water Chemistry of Some Canadian East Coast Lakes 1." Limnology and Oceanography **3**(3): 299-307.

Heiri, O., et al. (2001). "Loss on ignition as a method for estimating organic and carbonate content in sediments: reproducibility and comparability of results." Journal of paleolimnology **25**: 101-110.

Helama, S., et al. (2017). "Regional curve standardization: State of the art." The Holocene **27**(1): 172-177.

Helmer, M., et al. (2020). "Mapping heritage ecosystem services in ecological restoration areas: A case study from the East Cascades, Washington." Journal of Outdoor Recreation and Tourism **31**: 100314.

Henke, L. M., et al. (2017). "Was the Little Ice Age more or less El Niño-like than the Medieval Climate Anomaly? Evidence from hydrological and temperature proxy data." Climate of the Past **13**(3): 267-301.

Hereid, K. A., et al. (2013). "Coral record of reduced El Niño activity in the early 15th to middle 17th centuries." Geology **41**(1): 51-54.

Hessburg, P. F. and J. K. Agee (2003). "An environmental narrative of inland northwest United States forests, 1800–2000." Forest Ecology and Management **178**(1-2): 23-59.

Hessburg, P. F., et al. (2005). "Dry forests and wildland fires of the inland Northwest USA: contrasting the landscape ecology of the pre-settlement and modern eras." Forest Ecology and Management **211**(1-2): 117-139.

Hessburg, P. F., et al. (2021). "Wildfire and climate change adaptation of western North American forests: a case for intentional management." Ecological Applications **31**(8): e02432.

Hessl, A. E., et al. (2004). "Drought and Pacific Decadal Oscillation linked to fire occurrence in the inland Pacific Northwest." Ecological Applications **14**(2): 425-442.

Heyerdahl, E. K., et al. (2008). "Climate drivers of regionally synchronous fires in the inland Northwest (1651–1900)." International Journal of Wildland Fire **17**(1): 40-49.

Higley, M. C., et al. (2018). "Last millennium meridional shifts in hydroclimate in the central tropical Pacific." Paleoceanography and Paleoclimatology **33**(4): 354-366.

Higuera, P. E. and J. T. Abatzoglou (2021). "Record-setting climate enabled the extraordinary 2020 fire season in the western United States." Global change biology **27**(1).

Hillman, A. L., et al. (2018). "Climate and anthropogenic controls on the carbon cycle of Xingyun Lake, China." Palaeogeography, Palaeoclimatology, Palaeoecology **501**: 70-81.

Hilton, J. (1985). "A conceptual framework for predicting the occurrence of sediment focusing and sediment redistribution in small lakes." Limnology and Oceanography **30**(6): 1131-1143.

Hodell, D. A. and C. L. Schelske (1998). "Production, sedimentation, and isotopic composition of organic matter in Lake Ontario." Limnology and Oceanography **43**(2): 200-214.

Hogg, A. G., et al. (2020). "SHCal20 Southern Hemisphere calibration, 0–55,000 years cal BP." Radiocarbon **62**(4): 759-778.

Hooke, J. (2003). "Coarse sediment connectivity in river channel systems: a conceptual framework and methodology." Geomorphology **56**(1-2): 79-94.

Horton, T. W., et al. (2016). "Evaporation induced 18O and 13C enrichment in lake systems: A global perspective on hydrologic balance effects." Quaternary Science Reviews **131**: 365-379.

Hsiang, S. M., et al. (2011). "Civil conflicts are associated with the global climate." Nature **476**(7361): 438-441.

Hu, J., et al. (2017). "Correlation-based interpretations of paleoclimate data–where statistics meet past climates." Earth and Planetary Science Letters **459**: 362-371.

Hu, S. and A. V. Fedorov (2018). "Cross-equatorial winds control El Niño diversity and change." Nature Climate Change **8**(9): 798-802.

Jackson, S. T., et al. (2009). "Ecology and the ratchet of events: climate variability, niche dimensions, and species distributions." Proceedings of the National Academy of Sciences **106**(supplement_2): 19685-19692.

Jiang, L., et al. (2021). "ENSO variability during the medieval climate Anomaly as recorded by Porites corals from the northern South China Sea." Paleoceanography and Paleoclimatology **36**(4): e2020PA004173.

Karamperidou, C. and P. N. DiNezio (2022). "Holocene hydroclimatic variability in the tropical Pacific explained by changing ENSO diversity." Nature communications **13**(1): 7244.

Kelts, K. and K. Hsü (1978). "Freshwater carbonate sedimentation." Lakes: chemistry, geology, physics: 295-323.

Kiefer, J. and C. Karamperidou (2019). "High-Resolution Modeling of ENSO-Induced Precipitation in the Tropical Andes: Implications for Proxy Interpretation." Paleoceanography and Paleoclimatology **34**(2): 217-236.

Kirby, M., et al. (2010). "A Holocene record of Pacific decadal oscillation (PDO)-related hydrologic variability in southern California (Lake Elsinore, CA)." Journal of paleolimnology **44**: 819-839.

Kitzberger, T., et al. (2007). "Contingent Pacific–Atlantic Ocean influence on multicentury wildfire synchrony over western North America." Proceedings of the National Academy of Sciences **104**(2): 543-548.

Komada, T., et al. (2008). "Carbonate removal from coastal sediments for the determination of organic carbon and its isotopic signatures, δ13C and Δ14C: comparison of fumigation and direct acidification by hydrochloric acid." Limnology and Oceanography: Methods **6**(6): 254-262.

Koutavas, A. and S. Joanides (2012). "El Niño–Southern oscillation extrema in the holocene and last glacial maximum." Paleoceanography **27**(4).

Koutavas, A. and J. Lynch-Stieglitz (2004). Variability of the marine ITCZ over the eastern Pacific during the past 30,000 years. The Hadley circulation: Present, past and future, Springer**:** 347-369.

Kovanen, D. J. and O. Slaymaker (2004). "Glacial imprints of the Okanogan Lobe, southern margin of the Cordilleran Ice Sheet." Journal of Quaternary Science: Published for the Quaternary Research Association **19**(6): 547-565.

Kumar, K. K., et al. (1999). "On the weakening relationship between the Indian monsoon and ENSO." Science **284**(5423): 2156-2159.

Kumar, K. K., et al. (2006). "Unraveling the mystery of Indian monsoon failure during El Niño." Science **314**(5796): 115-119.

Lanzante, J. R. (2021). "Testing for differences between two distributions in the presence of serial correlation using the Kolmogorov–Smirnov and Kuiper's tests." International Journal of Climatology **41**(14): 6314-6323.

Lapointe, F. and R. S. Bradley (2021). "Little Ice Age abruptly triggered by intrusion of Atlantic waters into the Nordic Seas." Science advances **7**(51): eabi8230.

Lechleitner, F. A., et al. (2017). "Tropical rainfall over the last two millennia: evidence for a low-latitude hydrologic seesaw." Scientific Reports **7**(1): 1-9.

Ledru, M.-P., et al. (2013). "The Medieval climate anomaly and the Little Ice Age in the eastern Ecuadorian Andes." Climate of the Past **9**(1): 307-321.

Lehmann, S. B., et al. (2021). "Prolonged early to middle Holocene drought in the Pacific Northwest inferred from lacustrine carbonate oxygen isotope values and sedimentology." Quaternary Science Reviews **271**: 107192.

Levine, A. F., et al. (2017). "The impact of the AMO on multidecadal ENSO variability." Geophysical Research Letters **44**(8): 3877-3886.

Li, H.-C. and T.-L. Ku (1997). "δ13C–δ18C covariance as a paleohydrological indicator for closed-basin lakes." Palaeogeography, Palaeoclimatology, Palaeoecology **133**(1-2): 69-80.

Li, J., et al. (2011). "Interdecadal modulation of El Niño amplitude during the past millennium." Nature Climate Change **1**(2): 114-118.

Li, J., et al. (2013). "El Niño modulations over the past seven centuries." Nature Climate Change **3**(9): 822-826.

Liu, Z. and M. Alexander (2007). "Atmospheric bridge, oceanic tunnel, and global climatic teleconnections." Reviews of Geophysics **45**(2).

Long, C. J., et al. (2014). "The impact of Mt Mazama tephra deposition on forest vegetation in the Central Cascades, Oregon, USA." The Holocene **24**(4): 503-511.

Long, C. J., et al. (2019). "A 7600 yr vegetation and fire history from Anthony Lake, northeastern Oregon, USA, with linkages to modern synoptic climate patterns." Quaternary Research **91**(2): 705-713.

Lu, Z., et al. (2018). "A review of paleo El Niño-southern oscillation." Atmosphere **9**(4): 130.

Mabaso, M. L., et al. (2007). "El Niño southern oscillation (ENSO) and annual malaria incidence in southern Africa." Transactions of the Royal Society of Tropical Medicine and Hygiene **101**(4): 326-330.

MacDonald, G. M. and R. A. Case (2005). "Variations in the Pacific Decadal Oscillation over the past millennium." Geophysical Research Letters **32**(8).

Mack, R. N., et al. (1976). "Pollen sequence from the Columbia Basin, Washington: Reappraisal of postglacial vegetation." American Midland Naturalist: 390-397.

Mack, R. N., et al. (1978). "Late Quaternary pollen record from Big Meadow, Pend Oreille County, Washington." Ecology **59**(5): 956-965.

Mack, R. N., et al. (1978). "Late Quaternary pollen record from the Sanpoil River valley, Washington." Canadian Journal of Botany **56**(14): 1642-1650.

Mack, R. N., et al. (1979). "Holocene vegetation history of the Okanogan Valley, Washington." Quaternary Research **12**(2): 212-225.

Mack, R. N., et al. (1983). "Holocene vegetational history of the Kootenai River valley, Montana." Quaternary Research **20**(2): 177-193.

Mann, D. H., et al. (2019). "Climate-driven ecological stability as a globally shared cause of Late Quaternary megafaunal extinctions: the Plaids and Stripes Hypothesis." Biological Reviews **94**(1): 328-352.

Mann, M. E., et al. (2021). "Multidecadal climate oscillations during the past millennium driven by volcanic forcing." Science **371**(6533): 1014-1019.

Mann, M. E., et al. (2020). "Absence of internal multidecadal and interdecadal oscillations in climate model simulations." Nature communications **11**(1): 49.

Mann, M. E., et al. (2009). "Global signatures and dynamical origins of the Little Ice Age and Medieval Climate Anomaly." Science **326**(5957): 1256-1260.

Mantilla, G., et al. (2009). "The role of ENSO in understanding changes in Colombia's annual malaria burden by region, 1960–2006." Malaria journal **8**(1): 1-11.

Mantua, N. J., et al. (1997). "A Pacific interdecadal climate oscillation with impacts on salmon production." Bulletin of the American Meteorological Society **78**(6): 1069-1080.

Mark, S. Z., et al. (2022). "XRF analysis of Laguna Pallcacocha sediments yields new insights into Holocene El Niño development." Earth and Planetary Science Letters **593**: 117657.

Marlon, J. R., et al. (2012). "Long-term perspective on wildfires in the western USA." Proceedings of the National Academy of Sciences **109**(9): E535-E543.

Marsh, E. J., et al. (2018). "IntCal, SHCal, or a mixed curve? Choosing a 14C calibration curve for archaeological and paleoenvironmental records from tropical South America." Radiocarbon **60**(3): 925-940.

Masson-Delmotte, V., et al. (2013). "Information from paleoclimate archives."

McAfee, S. A. and E. K. Wise (2016). "Intra-seasonal and inter-decadal variability in ENSO impacts on the Pacific Northwest." International Journal of Climatology **36**(1): 508-516.

McCabe, G. J., et al. (2004). "Pacific and Atlantic Ocean influences on multidecadal drought frequency in the United States." Proceedings of the National Academy of Sciences **101**(12): 4136-4141.

McDaniel, P., et al. (2005). "Andic soils of the inland Pacific Northwest, USA: properties and ecological significance." Soil Science **170**(4): 300-311.

McGregor, H., et al. (2013). "A weak El Niño/Southern Oscillation with delayed seasonal growth around 4,300 years ago." Nature Geoscience **6**(11): 949-953.

McGregor, H. V. and M. K. Gagan (2004). "Western Pacific coral δ18O records of anomalous Holocene variability in the El Niño–Southern Oscillation." Geophysical Research Letters **31**(11).

McGregor, S., et al. (2014). "Recent Walker circulation strengthening and Pacific cooling amplified by Atlantic warming." Nature Climate Change **4**(10): 888-892.

McPhaden, M. J., et al. (2020). "Introduction to El Niño Southern Oscillation in a changing climate." El Niño Southern Oscillation in a Changing Climate: 1-19.

Menounos, B., et al. (2017). "Cordilleran Ice Sheet mass loss preceded climate reversals near the Pleistocene Termination." Science **358**(6364): 781-784.

Mensing, S., et al. (2006). "Long-term fire history in Great Basin sagebrush reconstructed from macroscopic charcoal in spring sediments, Newark Valley, Nevada." Western North American Naturalist **66**(1): 64-77.

Meyers, P. A. and E. Lallier-Vergès (1999). "Lacustrine sedimentary organic matter records of Late Quaternary paleoclimates." Journal of paleolimnology **21**: 345-372.

Meyers, S. (2014). Astrochron: An R package for astrochronology.

Miller, R. F. and R. J. Tausch (2000). The role of fire in pinyon and juniper woodlands: a descriptive analysis. Proceedings of the invasive species workshop: the role of fire in the control and spread of invasive species. Fire conference.

Millspaugh, S. H., et al. (2000). "Variations in fire frequency and climate over the past 17 000 yr in central Yellowstone National Park." Geology **28**(3): 211-214.

Minaya, V., et al. (2016). "Simulating gross primary production and stand hydrological processes of páramo grasslands in the Ecuadorian Andean Region using the BIOME-BGC model." Soil Science **181**(7): 335-346.

Moffa-Sánchez, P. and I. R. Hall (2017). "North Atlantic variability and its links to European climate over the last 3000 years." Nature communications **8**(1): 1726.

Moon, V. G. (1993). "Microstructural controls on the geomechanical behaviour of ignimbrite." Engineering Geology **35**(1-2): 19-31.

Moy, C. M., et al. (2002). "Variability of El Niño/Southern Oscillation activity at millennial timescales during the Holocene epoch." Nature **420**(6912): 162.

Murton, D. K. and S. J. Crowhurst (2020). "Cross correlation of CIELAB color reflectance data from archive photographs and line-scan images of sediment." Quaternary Research **93**: 267-283.

Mushet, G. R., et al. (2023). "The importance of effective moisture and landscape controls on diatom assemblages and primary production in Roche Lake, British Columbia, Canada over the past ca. 1800 years." Quaternary Research **111**: 53-67.

Mushet, G. R., et al. (2022). "Postglacial hydroclimate in the southern interior of British Columbia (Canada): Lake ecosystem response to the Holocene Thermal Maximum and drivers of mid-to-late Holocene climate variability." Quaternary Science Reviews **276**: 107302.

Nascimento, M., et al. (2020). "The adoption of agropastoralism and increased ENSO frequency in the Andes." Quaternary Science Reviews **243**: 106471.

Nederbragt, A. J. and J. Thurow (2005). "Amplitude of ENSO cycles in the Santa Barbara Basin, off California, during the past 15 000 years." Journal of Quaternary Science: Published for the Quaternary Research Association **20**(5): 447-456.

Neely, A. B., et al. (2019). "Bedrock fracture density controls on hillslope erodibility in steep, rocky landscapes with patchy soil cover, southern California, USA." Earth and Planetary Science Letters **522**: 186-197.

Nelson, D. B., et al. (2011). "Drought variability in the Pacific Northwest from a 6,000-yr lake sediment record." Proceedings of the National Academy of Sciences **108**(10): 3870-3875.

Newman, M., et al. (2016). "The Pacific decadal oscillation, revisited." Journal of Climate **29**(12): 4399-4427.

Nidheesh, A., et al. (2017). "Influence of ENSO on the Pacific decadal oscillation in CMIP models." Climate Dynamics **49**: 3309-3326.

Oksanen, J., et al. (2013). "Package 'vegan'." Community ecology package, version **2**(9): 1-295.

Parnell, A. (2014). "Bchron: Radiocarbon dating, age-depth modelling, relative sea level rate estimation, and non-parametric phase modelling." R package version **4**(1).

Parnell, A. and M. A. Parnell (2021). "Package 'Bchron'."

Pausata, F. S., et al. (2017). "Greening of the Sahara suppressed ENSO activity during the mid-Holocene." Nature communications **8**(1): 1-12.

Pederson, G. T., et al. (2011). "The unusual nature of recent snowpack declines in the North American Cordillera." Science **333**(6040): 332-335.

Peinerud, E. K. (2000). "Interpretation of Si concentrations in lake sediments: three case studies." Environmental Geology **40**(1-2): 64-72.

Pfeil-McCullough, E., et al. (2015). "Emerald ash borer and the urban forest: Changes in landslide potential due to canopy loss scenarios in the City of Pittsburgh, PA." Science of the total environment **536**: 538-545.

Pompeani, D. P., et al. (2018). "Climate, fire, and vegetation mediate mercury delivery to midlatitude lakes over the holocene." Environmental science & technology **52**(15): 8157-8164.

Poore, R., et al. (2003). "Millennial-to century-scale variability in Gulf of Mexico Holocene climate records." Paleoceanography **18**(2).

Power, M. J., et al. (2006). "Fire and vegetation history during the last 3800 years in northwestern Montana." Geomorphology **75**(3-4): 420-436.

Praetorius, S. K., et al. (2020). "The role of Northeast Pacific meltwater events in deglacial climate change." Science advances **6**(9): eaay2915.

Quinn, W. H., et al. (1987). "El Niño occurrences over the past four and a half centuries." Journal of Geophysical Research: Oceans **92**(C13): 14449-14461.

Rahmstorf, S., et al. (2015). "Exceptional twentieth-century slowdown in Atlantic Ocean overturning circulation." Nature Climate Change **5**(5): 475-480.

Rasmusson, E. M. and J. M. Wallace (1983). "Meteorological aspects of the El Nino/southern oscillation." Science **222**(4629): 1195-1202.

Reimer, P. J., et al. (2020). "The IntCal20 Northern Hemisphere radiocarbon age calibration curve (0–55 cal kBP)." Radiocarbon **62**(4): 725-757.

Ren, H.-L. and F.-F. Jin (2013). "Recharge oscillator mechanisms in two types of ENSO." Journal of Climate **26**(17): 6506-6523.

Roberts, W. H., et al. (2014). "ENSO in the mid-Holocene according to CSM and HadCM3." Journal of Climate **27**(3): 1223-1242.

Rodbell, D. T., et al. (1999). "An~ 15,000-year record of El Niño-driven alluviation in southwestern Ecuador." Science **283**(5401): 516-520.

Rodbell, D. T., et al. (2008). "Clastic sediment flux to tropical Andean lakes: records of glaciation and soil erosion." Quaternary Science Reviews **27**(15-16): 1612-1626.

Rodionov, S., et al. (2007). "The Aleutian Low, storm tracks, and winter climate variability in the Bering Sea." Deep Sea Research Part II: Topical Studies in Oceanography **54**(23-26): 2560-2577.

Rodysill, J. R., et al. (2019). "La Niña-driven flooding in the Indo-Pacific warm pool during the past millennium." Quaternary Science Reviews **225**: 106020.

Rosenmeier, M. F., et al. (2002). "A 4000-year lacustrine record of environmental change in the southern Maya lowlands, Petén, Guatemala." Quaternary Research **57**(2): 183-190.

Rustic, G. T., et al. (2015). "Dynamical excitation of the tropical Pacific Ocean and ENSO variability by Little Ice Age cooling." Science **350**(6267): 1537-1541.

Rustic, G. T., et al. (2020). "Modulation of late Pleistocene ENSO strength by the tropical Pacific thermocline." Nature communications **11**(1): 5377.

Santos, G. M. and K. Ormsby (2013). "Behavioral variability in ABA chemical pretreatment close to the 14C age limit." Radiocarbon **55**(2–3): 534-544.

Schiefer, E. (2006). "Predicting sediment physical properties within a montane lake basin, southern Coast Mountains, British Columbia, Canada." Lake and Reservoir Management **22**(1): 69-78.

Schiller, C. M., et al. (2020). "Vegetation responses to Quaternary volcanic and hydrothermal disturbances in the Northern Rocky Mountains and Greater Yellowstone Ecosystem (USA)." Palaeogeography, Palaeoclimatology, Palaeoecology **559**: 109859.

Schillerberg, T. A. and D. Tian (2020). "Changes of crop failure risks in the United States associated with large-scale climate oscillations in the Atlantic and Pacific Oceans." Environmental Research Letters **15**(6): 064035.

Schillereff, D. N., et al. (2014). "Flood stratigraphies in lake sediments: A review." Earth-Science Reviews **135**: 17-37.

Schillereff, D. N., et al. (2016). "Hydrological thresholds and basin control over paleoflood records in lakes." Geology **44**(1): 43-46.

Schmidt, M. W., et al. (2012). "Solar forcing of Florida Straits surface salinity during the early Holocene." Paleoceanography **27**(3).

Schneider, T., et al. (2014). "Migrations and dynamics of the intertropical convergence zone." Nature **513**(7516): 45-53.

Schneider, T., et al. (2018). "Paleo-ENSO revisited: Ecuadorian Lake Pallcacocha does not reveal a conclusive El Niño signal." Global and planetary change **168**: 54-66.

Schnurrenberger, D., et al. (2003). "Classification of lacustrine sediments based on sedimentary components." Journal of paleolimnology **29**: 141-154.

Schoenemann, S. W., et al. (2020). "2,200-year tree-ring and lake-sediment based snowpack reconstruction for the northern Rocky Mountains highlights the historic magnitude of recent snow drought." Quaternary Science Advances **2**: 100013.

Schoennagel, T., et al. (2005). "ENSO and PDO variability affect drought-induced fire occurrence in Rocky Mountain subalpine forests." Ecological Applications **15**(6): 2000-2014.

Schwanghart, W. and D. Scherler (2014). "TopoToolbox 2–MATLAB-based software for topographic analysis and modeling in Earth surface sciences." Earth Surface Dynamics **2**(1): 1-7.

Shuman, B., et al. (2009). "Holocene lake-level trends in the Rocky Mountains, USA." Quaternary Science Reviews **28**(19-20): 1861-1879.

Shuman, B. N., et al. (2009). "Abrupt climate change as an important agent of ecological change in the Northeast US throughout the past 15,000 years." Quaternary Science Reviews **28**(17-18): 1693-1709.

Shuman, B. N., et al. (2018). "Placing the Common Era in a Holocene context: millennial to centennial patterns and trends in the hydroclimate of North America over the past 2000 years." Climate of the Past **14**(5): 665-686.

Steinman, B. A. and M. B. Abbott (2013). "Isotopic and hydrologic responses of small, closed lakes to climate variability: Hydroclimate reconstructions from lake sediment oxygen isotope records and mass balance models." Geochimica et Cosmochimica Acta **105**: 342-359.

Steinman, B. A., et al. (2014). "Ocean-atmosphere forcing of centennial hydroclimate variability in the Pacific Northwest." Geophysical Research Letters **41**(7): 2553-2560.

Steinman, B. A., et al. (2014). "Ocean-atmosphere forcing of centennial hydroclimate variability in the Pacific Northwest." Geophysical Research Letters **41**(7): 2553-2560.

Steinman, B. A., et al. (2012). "1,500 year quantitative reconstruction of winter precipitation in the Pacific Northwest." Proceedings of the National Academy of Sciences **109**(29): 11619-11623.

Steinman, B. A., et al. (2013). "Isotopic and hydrologic responses of small, closed lakes to climate variability: Comparison of measured and modeled lake level and sediment core oxygen isotope records." Geochimica et Cosmochimica Acta **105**: 455-471.

Steinman, B. A., et al. (2019). "Lake sediment records of Holocene hydroclimate and impacts of the Mount Mazama eruption, north-central Washington, USA." Quaternary Science Reviews **204**: 17-36.

Steinman, B. A., et al. (2016). "Oxygen isotope records of Holocene climate variability in the Pacific Northwest." Quaternary Science Reviews **142**: 40-60.

Steinman, B. A., et al. (2010). "The isotopic and hydrologic response of small, closed-basin lakes to climate forcing from predictive models: Application to paleoclimate studies in the upper Columbia River basin." Limnology and Oceanography **55**(6): 2231-2245.

Steinman, B. A., et al. (2022). "Interhemispheric antiphasing of neotropical precipitation during the past millennium." Proceedings of the National Academy of Sciences **119**(17): e2120015119.

Stevenson, S., et al. (2016). "“El Niño like” hydroclimate responses to last millennium volcanic eruptions." Journal of Climate **29**(8): 2907-2921.

Stone, J. R. and S. C. Fritz (2006). "Multidecadal drought and Holocene climate instability in the Rocky Mountains." Geology **34**(5): 409-412.

Sun, W., et al. (2022). "Pacific multidecadal (50–70 year) variability instigated by volcanic forcing during the Little Ice Age (1250–1850)." Climate Dynamics: 1-14.

Sung, M. K., et al. (2014). "A physical mechanism of the precipitation dipole in the western United States based on PDO-storm track relationship." Geophysical Research Letters **41**(13): 4719-4726.

Svenning, J. C. and B. Sandel (2013). "Disequilibrium vegetation dynamics under future climate change." American Journal of Botany **100**(7): 1266-1286.

Tan, L., et al. (2019). "Rainfall variations in central Indo-Pacific over the past 2,700 y." Proceedings of the National Academy of Sciences **116**(35): 17201-17206.

Thompson, D. M., et al. (2017). "Tropical Pacific climate variability over the last 6000 years as recorded in Bainbridge Crater Lake, Galápagos." Paleoceanography **32**(8): 903-922.

Thompson, D. M., et al. (2017). "Tropical Pacific climate variability over the last 6000 years as recorded in Bainbridge Crater Lake, Galápagos." Paleoceanography **32**(8): 903-922.

Timmermann, A., et al. (2007). "The influence of a weakening of the Atlantic meridional overturning circulation on ENSO." Journal of Climate **20**(19): 4899-4919.

Tinner, W. and A. F. Lotter (2001). "Central European vegetation response to abrupt climate change at 8.2 ka." Geology **29**(6): 551-554.

Torrence, C. and G. P. Compo (1998). "A practical guide to wavelet analysis." Bulletin of the American Meteorological Society **79**(1): 61-78.

Trenberth, K. E. (1997). "The definition of el nino." Bulletin of the American Meteorological Society **78**(12): 2771-2778.

Trouet, V., et al. (2013). "A 1500-year reconstruction of annual mean temperature for temperate North America on decadal-to-multidecadal time scales." Environmental Research Letters **8**(2): 024008.

Trouet, V., et al. (2006). "Fire-climate interactions in forests of the American Pacific coast." Geophysical Research Letters **33**(18).

Tudhope, A. W., et al. (2001). "Variability in the El Niño-Southern Oscillation through a glacial-interglacial cycle." Science **291**(5508): 1511-1517.

Verbruggen, W., et al. (2021). "Contrasting responses of woody and herbaceous vegetation to altered rainfall characteristics in the Sahel." Biogeosciences **18**(1): 77-93.

Viau, A., et al. (2012). "The climate of North America during the past 2000 years reconstructed from pollen data." Global and planetary change **84**: 75-83.

Walker, G. T. (1924). "Correlations in seasonal variations of weather. VIII, A further study of world weather." Men. Indian Meteor. Dept. **24**: 275-332.

Walsh, M. K., et al. (2018). "Toward a better understanding of climate and human impacts on late Holocene fire regimes in the Pacific Northwest, USA." Progress in Physical Geography: Earth and Environment **42**(4): 478-512.

Walsh, M. K., et al. (2015). "A regional perspective on Holocene fire–climate–human interactions in the Pacific Northwest of North America." Annals of the Association of American Geographers **105**(6): 1135-1157.

Webb, T. (1986). "Is vegetation in equilibrium with climate? How to interpret late-Quaternary pollen data." Vegetatio **67**: 75-91.

Westerling, A. L. and T. W. Swetnam (2003). "Interannual to decadal drought and wildfire in the western United States." EOS, Transactions American Geophysical Union **84**(49): 545-555.

Whipple, K. X., et al. (2000). "River incision into bedrock: Mechanics and relative efficacy of plucking, abrasion, and cavitation." Geological Society of America Bulletin **112**(3): 490-503.

White, S. and A. Ravelo (2020). "Dampened El Niño in the early Pliocene warm period." Geophysical Research Letters **47**(4): e2019GL085504.

White, S. M., et al. (2018). "Dampened El Niño in the early and mid-Holocene due to insolation-forced warming/deepening of the thermocline." Geophysical Research Letters **45**(1): 316-326.

Whitlock, C. (1992). "Vegetational and climatic history of the Pacific Northwest during the last 20,000 years: implications for understanding present-day biodiversity." Northwest Environmental Journal **8**: 5-5.

Whitlock, C. and P. J. Bartlein (1997). "Vegetation and climate change in northwest America during the past 125 kyr." Nature **388**(6637): 57-61.

Whitlock, C., et al. (2012). "Holocene seasonal variability inferred from multiple proxy records from Crevice Lake, Yellowstone National Park, USA." Palaeogeography, Palaeoclimatology, Palaeoecology **331**: 90-103.

Whitlock, C. and C. Larsen (2001). "Charcoal as a fire proxy." Tracking environmental change using lake sediments: terrestrial, algal, and siliceous indicators: 75-97.

Williams, A. P., et al. (2020). "Large contribution from anthropogenic warming to an emerging North American megadrought." Science **368**(6488): 314-318.

Williams, J. W., et al. (2021). "A unifying framework for studying and managing climate-driven rates of ecological change." Nature Ecology & Evolution **5**(1): 17-26.

Williams, J. W., et al. (2002). "Rapid and widespread vegetation responses to past climate change in the North Atlantic region." Geology **30**(11): 971-974.

Williamson, M. S., et al. (2018). "Effect of AMOC collapse on ENSO in a high resolution general circulation model." Climate Dynamics **50**: 2537-2552.

Willis, K. J. and H. J. B. Birks (2006). "What is natural? The need for a long-term perspective in biodiversity conservation." Science **314**(5803): 1261-1265.

Winkler, D. E., et al. (2019). "Shrub persistence and increased grass mortality in response to drought in dryland systems." Global change biology **25**(9): 3121-3135.

Wise, E. K. (2010). "Spatiotemporal variability of the precipitation dipole transition zone in the western United States." Geophysical Research Letters **37**(7).

Wise, E. K. and M. P. Dannenberg (2014). "Persistence of pressure patterns over North America and the North Pacific since AD 1500." Nature communications **5**(1): 1-6.

Wise, E. K. and M. P. Dannenberg (2017). "Reconstructed storm tracks reveal three centuries of changing moisture delivery to North America." Science advances **3**(6): e1602263.

Wright, C. S. and J. K. Agee (2004). "Fire and vegetation history in the eastern Cascade Mountains, Washington." Ecological Applications **14**(2): 443-459.

Wright, H. E., et al. (1984). "Piston corers for peat and lake sediments." Ecology **65**(2): 657-659.

Wynecoop, M. D., et al. (2019). "Getting back to fire suméŝ: exploring a multi-disciplinary approach to incorporating traditional knowledge into fuels treatments." Fire Ecology **15**(1): 1-18.

Yan, H., et al. (2011). "A record of the Southern Oscillation Index for the past 2,000 years from precipitation proxies." Nature Geoscience **4**(9): 611-614.

Zhang, Z., et al. (2014). "El Niño evolution during the Holocene revealed by a biomarker rain gauge in the Galápagos Islands." Earth and Planetary Science Letters **404**: 420-434.

Zheng, W., et al. (2008). "ENSO at 6ka and 21ka from ocean–atmosphere coupled model simulations." Climate Dynamics **30**(7-8): 745-762.

Zhu, F., et al. (2022). "A re-appraisal of the ENSO response to volcanism with paleoclimate data assimilation." Nature communications **13**(1): 747.